THE MIGRATION BEHAVIOUR OF XENON IMPLANTED INTO GLASSY CARBON

BY

MAHJOUB YAGOUB ABDALLA ISMAIL

Submitted in partial fulfilment of the requirements for the degree of

DOCTOR OF PHILOSOPHY (PhD) IN PHYSICS

In the Faculty of Natural and Agricultural Sciences at University of Pretoria

December …… 2019

Supervisor/Promoter: Prof. J. B. Malherbe

Co- supervisor: Dr. E. G. Njoroge

Co- supervisor: Prof. T. T. Hlatshwayo

UNIVERSITEIT VAN PRETORIA
UNIVERSITY OF PRETORIA
YUNIBESITHI YA PRETORIA

DECLARATION

I, Mahjoub Yagoub Abdalla Ismail, declare that the dissertation, which I hereby submit for the degree of PhD in University of Pretoria, is my own work and has not been submitted by for a degree at this or any other tertiary institution.

Signature: ……………………….

Date: …………………………….

SUMMARY

The migration behaviour of xenon implanted into glassy carbon

BY

Mahjoub Yagoub Abdalla Ismail

Submitted in partial fulfilment of the requirements for the degree of (PhD) in Physics in the Faculty of Natural and Agricultural Science, University of Pretoria

Supervisor/Promoter: Prof. J. B. Malherbe
Co- supervisor: Dr. E. G. Njoroge
Co- supervisor: Prof. T. T. Hlatshwayo

Glassy carbon is an isotropic, continuous and non-graphitizing carbon which combines the properties of glass, ceramic with those of graphite. It has some excellent properties like high tensile strength, high hardness; high electrical and thermal conductivities; and combined resistance to high temperature, corrosion and wear. Glassy carbon also has high impermeability to gases and liquids. No doubt, glassy carbon has found a good its way in the nuclear application field. In many reactor designs, the nuclear fuel becomes critical in the graphite core and during the operation of these reactors, activated fission products such as Cr, Cs, Cd, Fe, Ag, Pd, Ni among other fission elements are trapped within the structure of the graphite core. Interestingly, the problem with the graphite reactor core has been addressed by proposing glassy carbon as an alternative. Recently, the nuclear material group at the University of Pretoria has also proposed the use of glassy carbon as a containment material for radioactive fission products. For glassy carbon to be a good candidate for containment, it must be a good diffusion barrier for fission product like Xe and its near-surface region must remain unchanged under bombardment with low and swift heavy ion irradiation and extreme heat condition.

This study is in two parts. Both parts are geared towards the study of the effectiveness of glassy carbon as a good storage material was investigated. Firstly, 200 keV Xe ions were implanted into glassy carbon substrates to a fluence of 1×10^{16} ions/cm^2 at room temperature.

Also, we have also investigated the effect of SHI irradiation on Xe as-implanted samples at a fluence of 1×10^{14} ions/cm^2. After implantation and swift heavy ion irradiation, the samples were investigated using several techniques. This was with a view to characterizing the level of damage created by the ion bombardment, the distributions of the Xe ions in glassy carbon and the effect of SHI irradiation on these distributions. The irradiated and un-irradiated but implanted with Xe samples were isochronally annealed in a vacuum in steps of 100 °C for 5 hours at temperatures ranging from 300 °C – 800 °C and 900 °C – 1500 °C, respectively.

Raman spectroscopy was used to study the structure of the irradiated and un-irradiated samples implanted with Xe before and after annealing. The scanning electron microscopy (SEM) was used to monitor the surface morphology after each annealing cycle. The migration behaviour of Xe in the irradiated and un-irradiated but implanted samples before and after each annealing step were investigated by Rutherford backscattering spectrometry (RBS). We have reported the conventional RBS depth profile results after annealing at two different temperature regimes, 300 °C – 800 °C and 900 °C – 1500 °C, respectively. For the first annealing temperature regime, 300 °C – 800 °C no noticeable diffusion of Xe was observed as the profile remained nearly the same as compared to the as-implanted depth profile. The non-diffusion of Xe at these low temperatures was attributed to the amorphisation of the glassy carbon leading to creation of defects within the implanted region of the glassy carbon matrix. The defects which could be in terms of voids and vacancies are responsible for the trapping of Xe well within the damaged region of the glassy carbon matrix. The Xe profile shifted towards the surface of glassy carbon after annealing at 900 °C. The shift at this temperature towards the surface was accompanied with slight broadening of the Xe profile. This broadening was considered critical because the diffusion of Xe was Fickian (Gaussian) in nature. Annealing from 900 °C – 1500 °C resulted in the movement of Xe profile deeper beyond the damaged bulk deeper into the undamaged bulk of glassy carbon and the formation of a bimodal distribution was also observed. As the Xe atom moved deeper into the undamaged bulk, the migration behaviour extends up to a depth of 800 nm deeper into the undamaged bulk with increasing bimodal distribution formation after annealing at 1400 °C. A suggestive model given to the migration behaviour of Xe is the presence of large number of pores in glassy carbon. These pores needs to be filled up when Xe atoms become more energized after annealing at higher temperatures.

The Raman result for the virgin glassy carbon spectra obtained at 514.5 nm shows that D and G peaks are at 1350 cm^{-1} and 1587 cm^{-1}, respectively. Xenon implantation into glassy carbon

resulted in amorphisation as evident by the merging of D and G peaks, decreased I_D/I_G ratio and increased FWHM. Annealing of the sample in the first temperature regime shows that the damaged layer caused by Xe implantation start to recrystallizes after annealing at 500 °C. This temperature is considered a dynamic annealing temperature for Xe implanted glassy carbon. The recrystallization of the glassy carbon are accompanied by some changes after annealing at 500 °C – 900 °C. These changes include a decrease and narrowing of the FWHM of the G peak, a decrease in the I_D/I_G ratio and upshift in the G peak positions. However, annealing of the xenon implanted glassy carbon sample up to 1500 °C did not revert to its original state before ion implantation.

The re-growth of the Raman D and G peaks was further observed after high temperature annealing of the implanted glassy carbon from 1000 °C – 1500 °C. From 1000 °C – 1300 °C the D and G peaks shows better recovery with slightly increased G peak than the D peak. However, at 1400 °C and 1500 °C, the intensity of the D and G peak appear to be the same. At the highest annealing temperature, (1500 °C), the crystallite size, La of the implanted glassy carbon have increased from 0.88 to 1.39 nm. This is an indication that the structural recovery of the implanted layer resulted in a structure that is more graphite-like than the glassy carbon. The difference in the crystallite sizes also means that some of the damage introduced by Xe ion implantation was still retained after heat treatment at highest temperature.

The effect of xenon ions bombardment and heat treatment on the surface topography of the GC was characterized using scanning electron microscopy (SEM) and complemented with atomic force microscopy (AFM). AFM was used to evaluate and quantify the effect of Xe ion bombardment and annealing temperature on the surface roughness. The AFM result shows that the sample surface became rougher after Xe implantation. The increased roughness was later confirmed from the SEM micrographs. The SEM micrographs obtained from the samples showed that the polishing marks became prominent after ion bombardment. The surface roughness further increased after annealing at 1500 °C. The SEM micrograph of the sample annealed at 1500 °C shows a uniform distribution of large granules on the surface of the sample. The relative height difference in the implanted and un-implanted layer of glassy carbon was determined using AFM and this was used to calculate the density of the implanted glassy carbon which is 2.215 gcm^{-3}. This value is much comparable to the density of graphite which is 2.26 gcm^{-3}. This shows that the recovery of the implanted region resulted in a structure that is more graphite-like than glassy carbon.

The HRTEM analyses gave a clearer information on the structure of virgin glassy carbon and after ion bombardment. The TEM images of the virgin glassy carbon indicated a layered fullerene-like nano structure. This structure changed after Xe bombardment indicating the amorphisation of glassy carbon with the presence of some nano-crystallites features. The HRTEM image of sample annealed at 600 ^{o}C had showed some graphitic strands which became reduced after annealing at 1000 ^{o}C. The HRTEM result of annealed sample might depicts some form of recovery of the glassy carbon.

The effect of swift heavy ion (SHI) irradiation of Xe ion-implanted glassy carbon was also investigated. We hypothesized that glassy carbon will be exposed to radioactivity release (in orders of 100s MeV to few GeV) resulting from the fission process of nuclear waste with large range of energies. Glassy carbon proposed as a nuclear waste containment material in this study is expected to undergo structural changes after SHI irradiation. The RBS result of sample irradiated with 167 MeV Xe SHIs at fluence of 1×10^{14} ions/cm^2 indicates an increased shift of Xe ions towards the undamaged bulk of glassy carbon as compared to the un-irradiated but implanted samples. This shift of Xe may be due to the transient melting along the ion trajectory which also resulted in a little amount of xenon that have evaporated.

The Xe SHIs irradiated but implanted sample was annealed in the temperature range of 1000 – 1500 ^{o}C in steps of 100 for 5 hours and characterize with RBS. The RBS depth profile of SHI irradiated but implanted sample indicate the diffusion of Xe after annealing at 1000 ^{o}C. The RBS depth profiles obtained for the sample irradiated with SHIs and subsequently annealed was not expected because the un-irradiated sample had a bimodal distribution after annealing at 1000 ^{o}C. The RBS depth profiles obtained for the sample irradiated with SHIs and subsequently annealed between 1100 and 1500 ^{o}C showed a similar migration behaviour for Xe as compared with the un-irradiated but implanted sample. This implies that SHIs irradiation does not influence the migration behaviour of Xe in glassy carbon at annealing temperature $\geq$1100 ^{o}C.

The effect of SHIs on the damaged layer of the implanted glassy carbon was investigated by using Raman spectroscopy. Two distinguished peaks reappeared near the D and G bands of the glassy carbon as a result of SHIs irradiation. The G peak intensity became slightly more prominent as compared to the D peak intensity. This observation means that glassy carbon structure is already recrystallizing as a result of SHIs irradiation which was later confirmed by the calculated increased crystallite size. These results agree well with the RBS results for SHI irradiation.

Acknowledgements

I would like to acknowledge the following people for their support and valuable contribution to the success of my study.

- My academic promoter, Prof. J.B. Malherbe, his guidance, support, discussion and advice for all time has been immense value.
- My co-supervisors Dr. E. G. Njoroge and Prof. T. T. Hlatshwayo for their wonderful guidance, support, discussion during the course of this study.
- The head of department, Prof. C.C. Theron, for arranging some part-time work in the department, which helped me financially during this study.
- I would also like to express my gratitude, Dr. Eric Njoroge and Dr. Ope Odutomowo for their help, guidance in analysis the results and writing the thesis.
- The University of Pretoria Research and Innovation office for financial aids.
- Mrs Elfrieda Meyburgh for all her assistance in the physics department.
- Mr Ponkin Dmitry Olegovich, for his assistance during the research in JINR-Dubna, Russia.
- Mr Elsheikh Ibrahim and his family for their assistance during the visit to the UK.
- Fellow students in the Physics department for all their help, encouragement and moral support, and special thanks to my colleagues in the nuclear materials research group.
- My family for their endless love, support and encouragement throughout my studies and life.
- My wife Rashida and sons (Mohammed, Ahmed and Mustafa) for their love, patience, continuous support, encouragement and prayers.
- My parents, brothers, sisters and family members, who supported me during my studies and life.

LIST OF ABBREVIATIONS

AC – Amorphous Carbon

AFM – Atomic Force Microscopy

BSE – Backscattered Electrons

CCD - Charged Coupled Devices

DLC – Diamond –Like Carbon

FE-SEM- Field Emission Scanning Electron Microscope

FPs - Fission Products

FWHM – Full Width at Half Maximum

GC – Glassy Carbon

HLW – High Level Wastes

HRTEM – High Resolution Transmission Electron Microscopy

ILW – Intermediate Level Wastes

LLW – Low Level Wastes

MCA – Multi-Channel Analyser

RBS – Rutherford Backscattering spectrometry

SE – Secondary Electrons

SEM – Scanning electron microscopy

SHI –Swift Heavy Ion

SRIM – Stopping and Range of Ions in Matter

TRIM – Transport of Ions in Matter

TABLE OF CONTENTS

SUMMARY ii
CHAPTER 1 1
INTRODUCTION 1
1.1 Xenon as radioactive waste and poisoning 1
1.2 Classification of nuclear wastes 2
1.2.1 Low-level nuclear wastes (LLW) 2
1.2.2 Intermediate level nuclear wastes (ILW) 3
1.2.3 High-level nuclear wastes (HLW) 3
1.3 Storage of nuclear wastes 3
1.3.1 The wastes storage method 4
1.3.1.1 Wet storage method 4
1.3.1.2 Dry storage method 4
1.4 Motivation and research objectives 5
1.5 Outlay of thesis 7
References 8
CHAPTER 2 10
CARBON MATERIAL AND ITS ALLOTROPES 10
2.1 Allotropes of carbon: Structure, Properties and Applications 11
2.1.1 Graphite 12
2.1.1.1 Properties of graphite 14
2.1.1.2 Applications of graphite 15
2.1.1.2 Diamond 16
2.1.2.1 Properties of diamond 17
2.1.2.2 Applications of diamond 18
2.1.3 Amorphous carbon 19
2.1.3.1 Diamond-like carbon 19
2.1.3.2 Fullerenes 20
2.1.3.2.1 Properties of fullerenes 21
2.1.3.2.2 Applications of fullerenes 22
2.1.3.3 Glassy carbon 22
2.1.3.3.1 Structure of glassy carbon 23
2.1.3.3.2 Properties of glassy carbon 29
2.1.3.3.3 Applications of glassy carbon 30
References 31

CHAPTER 3 33
ION IMPLANTATION 33
3.1 General concepts 33
3.2 Stopping power of ions in solids 34
3.2.1 Nuclear Stopping 36
3.2.2 Electronic Stopping 39
3.3 Energy Straggling 41
3.4 Range of ion implanted 42
3.5 Simulation of xenon ion implanted in glassy carbon 46
3.6 Amorphisation 48
3.7 Annealing of the radiation damage 49
References 51
CHAPTER 4 54
DIFFUSION IN SOLIDS 54
4.1 Mechanisms of diffusion in solids 54
4.1.1 Volume Diffusion 54
4.1.1.1 Vacancy mechanism 54
4.1.1.2 Interstitial mechanism 55
4.1.1.2 Interstitialcy mechanism 56
4.1.2 Dislocations and grain boundaries mechanism 56
4.2 Mathematics of Diffusion 57
4.2.1 Fick's first law 57
4.2.2 Fick's second law 58
4.3 Estimating the diffusion coefficient 60
References 62
CHAPTER 5 63
ANALYTICAL TECHNIQUES 63
5.1 Rutherford Backscattering Spectrometry 63
5.1.1 The Van de Graaff accelerator 63
5.1.2 Principle and theory of Rutherford Backscattering Spectrometry 65
5.1.3 Kinematic Factor (K) 66
5.1.4 Scattering cross section (σ) 67
5.1.5 Depth scaling 68
5.1.6 Depth resolution 69
5.2 Raman Spectroscopy 70
5.2.1 Theory and principle of Raman Spectroscopy 70

5.2.2 The Raman instrument ... 73
5.3 Scanning Electron Microscopy ... 74
References ... 78
CHAPTER 6 ... 80
EXPERIMENTAL PROCEDURES ... 80
6.1 Sample preparation ... 80
6.2 Implantation procedures ... 80
6.3 Annealing of samples ... 81
6.4 The measurement conditions ... 84
6.4.1 The RBS measurement ... 84
6.4.2 Raman measurement ... 84
6.4.3 The SEM measurement ... 84
References ... 85
CHAPTER 7 ... 86
RESULTS AND DUSCUSSION ... 86
7.1 Implantation of glassy carbon with xenon ... 86
7.2 Effects of thermal annealing on migration and structure of Xe implanted glassy carbon ... 88
7.2.1 RBS Results ... 88
7.2.2 Raman results ... 93
7.2.3 Surface microstructure analysis using AFM and SEM analysis ... 104
7.2.4 Transmission electron microscopy (TEM) Results ... 110
7.2.5 Densification of glassy carbon due to Xe ion bombardment ... 115
7.3 Effects of SHI irradiation on migration and structure of Xe implanted glassy carbon ... 117
7.3.1 Swift heavy ion (SHI) irradiation ... 117
7.3.2 RBS results ... 119
7.3.3 Raman results ... 122
References ... 126
CHAPTER 8 ... 129
CONCLUSION ... 129
CHAPTER 9 ... 134
RESEARCH OUTPUT ... 134

LIST OF FIGURES

Fig. 1.1: A configuration for spent fuel waste storage (a) Wet storage (b) Dry storage methods [www1] [Nrc13]. 5

Fig. 2.1: Three different types of hybridization and their hybrid orbitals [Kru10]. 10

Fig. 2.2: Schematics showing the different allotropes of carbon. 11

Fig. 2.3: Crystal structure of different forms of graphite showing the (a) Hexagonal (b) Rhombohedral (c) Turbostratic stacking sequence [Pie93] [Zha17]. 14

Fig. 2.4: Lattice structure of (a) cubic diamond (b) hexagonal diamond [Kru10]. 17

Fig. 2.5: Phase diagram of diamond-like carbon materials [Gri99]. 20

Fig. 2.6: Molecular structure of C_{60} fullerene [Ans06]. 21

Fig. 2.7: The structural model for glassy carbon (a) proposed by Noda and Inagaki [Nod64] (b) proposed by Yamada [Yam64], oxygen bridge content in glassy carbon. *T* is a tetrahedral part in which the first neighbour distance is 1.55 Å and *G* a graphitic part in which the first neighbour distance is 1.42 Å. 25

Fig. 2.8: Structural model for the network of ribbon stacks in glassy carbon proposed Jenkins and Kawamura [Pie93]. 26

Fig. 2.9: The model of the structure of glassy carbon as proposed by Harris [Har05], (a) low-temperature and (b) high-temperature glassy carbon. 27

Fig. 2.10: HRTEM micrographs of virgin GC (a) closely packed particles (b) tightly curled single carbon layers (c) onion-like carbon structures. The images were obtained at different magnifications. 29

Fig. 3.1: Nuclear and electronic stopping powers of glassy carbon for Xe ions obtained from SRIM [Sri12]. The density of glassy carbon was taken as 1.42 g/cm^3. 36

Fig. 3.2: Scattering of an energetic ion by a stationary atom in the laboratory. 39

Fig. 3.3: Nuclear and electronic components of the ion stopping power as a function of ion velocity [Tri15]. 41

Fig. 3.4: The projected range R_P and the total range R for incident ion in target material. 44

Fig. 3.5: 200 keV xenon ions implanted in glassy carbon as a function of implantation depth. The first four moments of the implanted ion distributions are the projected range (R_p), the straggling (ΔR_p), the skewness (γ) and the kurtosis (β). Their values were obtained by fitting the as-implanted Xe depth profile to an Edgeworth distribution. 45

Fig. 3.6: TRIM [Sri12] simulation showing the: (a) trajectories of 200 keV xenon ions implanted in glassy carbon (b) the implanted Xe ion distribution and (c) the vacancy distribution. 48
Fig. 3.7: (a) Crystal damage and (b) annealed the damage. 50
Fig. 4.1: A schematic illustration of the vacancy diffusion mechanism: (a) and (b) are the positions of the atom before and after diffusion respectively. The atom A moves from (1) to (2) while the vacancy moves from (2) to (1). 55
Fig. 4.2: Interstitial mechanism of diffusion 56
Fig. 4.3: Interstitialcy mechanism of diffusion: (a) and (b) are the positions of self-interstitial before and after diffusion respectively. 56
Fig. 4.4: Illustration of Fick's first law, the concentration C is a function of the distance *x*. 58
Fig. 4.5: A differential volume element in a bar of cross-sectional area A. J_1 and J_2 are the flux of the impurity entering and exiting the volume element respectively. Redrawn from [Cam01]. 60
Fig. 5.1: Design of RBS set-up at the University of Pretoria. 64
Fig. 5.2: Sources of deadtime in a typical detection system. Redrawn from [Usm18]. 65
Fig. 5.3: A typical schematic of scattering between projectile and target atom. 67
Fig. 5.4: A schematic diagram illustrating the backscattering events of alpha particles and energy loss from depth *x* [Chu78]. 69
Fig. 5.5: Schematic illustration of the Rayleigh and Raman scattering processes. Both the low energy (upward arrows) and the scattered energy (downward arrows) have much larger energies than the energy of vibration. 71
Fig. 5.6: Schematic diagram showing the different components of a Raman instrument. 74
Fig. 5.7: Schematic diagram showing how the scanning electron microscope works [www1]. 75
Fig. 5.8: Diagram showing electron Beam interaction [www1]. 77
Fig. 6.1: Schematic diagram showing one of the annealing systems used in this research. 82
Fig. 6.2: Graph showing the annealing process at different temperatures. 83
Fig. 7.1: Depth profile of 200 keV Xe^+ ions implanted in glassy carbon at room temperature compared with SRIM simulation profile. The damage in dpa is also shown using the fluence of 1×10^{16}. 88
Fig. 7.2: The surface and maximum damage (dpa) of 200 keV and 320 keV Xe^+ ions implanted in glassy carbon at room temperature to a fluence of 1×10^{16} ions/cm^2. 88

Fig. 7.3: Xe depth profiles showing the effect of sequential at low temperature (300 – 800 °C) annealing on the migration behaviour. 90

Fig. 7. 4: Xe depth profiles showing the effect of sequential at high temperature (900 – 1400 °C) annealing on the migration behaviour. 92

Fig. 7. 5: The amount of Xe retained within the damaged region annealed at temperature (900 - 1400 °C). 93

Fig. 7. 6: Raman spectrum of (virgin) glassy carbon obtained with a 514.5 nm excitation laser wavelength. The red line is the cumulative fit peak while the green lines represent the individual peak fits. The peaks indicated by arrows are discussed in the text above. 94

Fig. 7.7: Raman spectra of 200 keV Xe implanted GC at room temperature and the effect of sequential annealing from 500 °C to 900 °C in steps of 100 °C for 5 h, on the structure of GC. The Figure also contains the Raman spectrum for virgin GC for comparison. 95

Fig. 7.8: Raman spectra of 200 keV Xe implanted GC at room temperature and the effect of sequential annealing from 1000 °C to 1500 °C in steps of 100 °C for 5 h, on the structure of GC. The Figure also contains the Raman spectrum for virgin GC for comparison. 97

Fig. 7.9: Raman spectrum of 200 keV Xe implanted GC at room temperature. The red lines are the cumulative fit peak while the green lines represent the individual peak fit. The Figure also contains the virgin GC Raman spectrum for comparison. 98

Fig. 7.10: The G peak position of the acquired spectra before and after Xe ions bombardment and heat treatment. The position of virgin GC is shown at 0 °C while the big drop at 23 °C represents the G peak position after xenon bombardment in the GC substrate. 101

Fig. 7.11: The effect of xenon ion bombardment and heat treatment on the FWHM values of the G peak acquired after fitting the spectra with the BWF function. The increase in the FWHM values compared to the virgin glassy carbon shows the effect of amorphisation of the GC substrate after ion bombardment and heat treatment. 102

Fig. 7.12: I_D/I_G ratios of virgin glassy carbon, after RT xenon ion bombardment compared with after heat treatment of implanted GC. 103

Fig. 7.13: AFM images obtained of the virgin GC substrate (a) Height image (b) deflection error (c) 3D of the height image. 105

Fig. 7.14: AFM images obtained from the Xe implanted GC substrate (a) Height image (b) deflection error (c) 3D of the height image. 106

Fig. 7.15: SEM micrographs of (a) virgin GC at low magnification, (b) virgin GC at high magnification, (c) and (d) GC after Xe ion bombardment at low and high magnification respectively. 106
Fig. 7.16: AFM images obtained for Xe implanted GC after annealing at 1000 °C (a) Height image (b) deflection error (c) 3D of height image. 107
Fig. 7.17: SEM micrographs of Xe implanted GC and annealed at 1000 °C for 5h. The images were obtained at different magnifications. 108
Fig. 7.18: AFM images obtained for Xe implanted GC after annealing at 1100 °C (a) Height image (b) deflection error (c) 3D of height image. 108
Fig. 7.19: SEM micrographs of Xe implanted GC and annealed at 1100 °C for 5h. The images were obtained at different magnifications. 109
Fig. 7.20: AFM images obtained for Xe implanted GC after annealing at 1500 °C (a) Height image (b) deflection error (c) 3D of height image. 110
Fig. 7.21: SEM micrographs of Xe implanted GC and annealed at 1500 °C for 5h. The images were obtained at different magnifications. 110
Fig. 7.22: HRTEM micrographs of virgin glassy carbon obtained at different magnifications. The onion-like structure of glassy carbon is highlighted in the brown circles in the Figures. 111
Fig. 7.23: HRTEM micrograph showing the effect of 200 keV Xe bombardment on GC taken at different magnifications. (a) is shows the contrast between the Pt protective layer, the implanted layer and the bulk of the glassy carbon. (b) – (d) are the HRTEM images obtained for the Xe implanted glassy carbon at different magnifications and positions. 113
Fig. 7.24: HRTEM micrographs showing the effect of 600 °C heat treatment on the microstructure of Xe implanted glassy carbon. (a) is shows the contrast between the Pt protective layer, the implanted layer and the bulk of the glassy carbon. (b) – (d) are the HRTEM images obtained within the Xe implanted layer at different magnifications and positions after 600 °C annealing. 114
Fig. 7.25: HRTEM micrographs showing the effect of 1000 °C heat treatment on the microstructure of Xe implanted glassy carbon. (a) is shows the contrast between the Pt protective layer, the implanted layer and the bulk of the glassy carbon. (b) – (d) are the HRTEM images obtained within the Xe implanted layer at different magnifications and positions after 1000 °C annealing. 115

Fig. 7.26: AFM line scan measurement taken from (a) implanted region to (b) un-implanted region of glassy carbon, to obtain the step height value between the two regions. 116
Fig. 7.27: Trajectories produced by 167 MeV Xe ion (white in colour) in GC along with the recoils (represented by green colour) [Sri12]. 118
Fig. 7.28: The energy loss of electronic (inelastic) and nuclear (elastic) collisions by Xe ion in GC, at the energy of 167 MeV [Sri12]. 118
Fig. 7.29: RBS spectra comparison of 200 keV Xe^{+} implanted GC, and irradiated with swift heavy ions at (167 MeV Xe^{+}). 120
Fig. 7.30: Xe depth profiles showing the effect of high temperature annealing on the migration behaviour (a) as-implanted RT (b) after SHI irradiation. 121
Fig. 7.31: The amount of Xe retained with the damaged region after SHI irradiation and annealed at temperature (1000 - 1400 ^{o}C). 122
Fig. 7.32: Raman spectrum of Xe implanted in GC at RT and thereafter irradiated by 167 MeV Xe ion at RT to a fluence of 1×10^{14}. The red lines are the cumulative fit peak while the green lines represent the individual peak fit. The virgin GC Raman spectrum included for comparison. 123
Fig. 7.33: Raman spectrum of xenon implanted GC at room then irradiated with SHI at room temperature and the effect of annealing at temperatures ranging from 1000 ^{o}C to 1500 ^{o}C in steps of 100 ^{o}C for 5 h, on the structure of GC. The Figure also contains the Raman spectrum for virgin GC for comparison. 125

LIST OF TABLES

Table 2.1: Some properties of hexagonal graphite [Pie93] [Miy98]. 15

Table 2.2: Some properties of cubic and hexagonal of diamond [Pie93] [Dre96] [May00] [Hay17]. 18

Table 2.3: Some physical properties of fullerene C_{60} molecules and its crystalline structure [Dre96] 21

Table 7. 1: A comparison of the range parameters obtained after fitting the RBS depth profiles at different temperatures with a Gaussian function. 89

Table 7. 2: The Raman spectroscopy results of the 200 keV Xe implanted GC at room temperature and annealed up to 1500 ^{o}C compared to the virgin glassy carbon. The quantitative values were acquired by fitting using a Lorentzian fit for the D peak and a Breit-Wigner-Fano (BWF) fit for the G peak. 99

Table 7. 3: The Raman results of the (200 keV Xe + SHI) irradiated GC at room temperature and annealed up to 1500 ^{o}C compared to the virgin glassy carbon at 0 C. The quantitative acquired by fitting using a Lorentzian fit for the D peak and a Breit-Wigner-Fano (BWF) fit for the G peak. 125

CHAPTER 1

INTRODUCTION

Nuclear energy supplies about 17% of the total electrical energy generated in the world. Further expansion of nuclear power offers a tempting alternative to relieve the pressure on countries to reduce greenhouse gases and their carbon footprints [Giu07]. However, the generation of nuclear energy raises a number of concerns for environment accidents such as those that occurred at Three Mile Island, Chernobyl and Fukushima. Radioactive waste is generated in a wide range of activities involving a wide variety of radioactive materials associated with the operation of nuclear facilities, the use of sealed radioactive sources in the industry, and the use of human-made radionuclides in hospitals and laboratories. The main activities that generate radioactive waste include nuclear power plant operations, nuclear fuel cycle activities and nuclear research activities [Iae06]. The physical, chemical and radiological characteristics of the waste arising from these activities are widely different [Iae06]. The general objective is to manage radioactive waste in such a way as to protect human health and the environment as well as to limit any burden in the future.

1.1 Xenon as radioactive waste and poisoning

Gaseous wastes often contain, along with gases, radioactive particulates which are fine particles in the air to which radioactive materials have stuck. These gases contain radionuclides such as ^{88}Kr, ^{131}I, and ^{133}Xe [Nag15]. Generally, all fission products can be classified as reactor poisons because they all absorb neutrons to some extent. However, two of the fission products, Xe-135 and Sm-149, are significant by themselves due to their absorption cross-section and high production as fission products or fission product daughters. Xenon-135 has a microscopic absorption cross-section of 3.5×10^{6} barns and a total fission product yield of 6.6%. Samarium-149 has an absorption cross-section of 42,000 barns and a total fission product yield of 1.4% [Cso83]. Xenon-135 is the more important of the two and will be dealt with and discuss in more detail.

Xenon is classified as a high-level nuclear waste element. It is mainly produced in nuclear fission reactions. It consists of various radioactive isotopes including xenon-135, which is of considerable significance in the operation of nuclear power reactors. The reason is that it acts

as a neutron absorber or poison, which can slow down or stop the chain reaction after a period of operation [Sae10]. A major contribution to the sequence of events leading to the Chernobyl nuclear disaster was the failure to anticipate the effect of xenon poisoning on the rate of the nuclear fission reaction [Dia03]. Xenon-135 is a product of U-235 fission and has a very large neutron-capture cross-section. It also decays radioactively with a half-life of 9.13 hours. Little of the Xe-135 results directly from a fission reaction. Most comes from the decay chain, Te-135 to I-135 to Xe-135 [Rog00]. ^{135}Xe, with its extremely high absorption cross-section of 2.65 $\times10^6$ barns is used up quickly upon creation, transmuting into ^{136}Xe, which is a stable isotope. ^{135}Xe is produced in the fuel in two ways:

I. Directly from fission, having a yield of about 0.3% of all fission products.
II. Indirectly is about 95% from the decay of iodine-135 as a secondary fission product, as a result of radioactive of iodine-135 via the following decay chain:

$$ {}^{135}_{52}\mathrm{T} \xrightarrow{\beta^-} {}^{135}_{53}\mathrm{I} \xrightarrow{\beta^-} {}^{135}_{53}\mathrm{Xe} \qquad (1.1)$$

1.2 Classification of nuclear wastes

Nuclear wastes are classified according to its activity level and the radioactive half-life as follow [www1] [Rah06]:

1.2.1 Low-level nuclear wastes (LLW)

Low-level nuclear wastes mainly come from the nuclear industry, as well as a few research laboratories and medical facilities. Low-level wastes can be stored into a sewage system and solid waste which are delivered to a landfill site or an incineration plant if the activities are below the nuclide-specific limits based on the annual limit on intake values. At the interim storage, the waste packages are loaded into 5 m^3 concrete containers. Most low-level radioactive waste is typically sent to land-based disposal immediately following its packaging for long-term management.

1.2.2 Intermediate level nuclear wastes (ILW)

Intermediate level nuclear wastes are mostly generated from spent fuel reprocessing and general operations and maintenance at nuclear sites. It has radioactivity levels that are higher than low-level waste but which do not generate enough heat to require special storage or disposal facilities. However, like other radioactive wastes, they need to be contained to protect workers from the radiation. Intermediate-level radioactive wastes are stored pending disposal in a geological repository. Some of ILW are disposed of in the Waste Isolation Pilot Plant (WIPP) deep geological repository.

1.2.3 High-level nuclear wastes (HLW)

High-level wastes consist of the spent nuclear fuels withdrawn from nuclear power plants following utilization for power generation and the highly radioactive waste resulting from the reprocessing of spent fuel. Some of these nuclear wastes in spent fuel have short half-lives, for example, iodine-131 has a half-life of 8-days and therefore their radioactivity decreases rapidly. However, most of them have long half-lives. For example, plutonium-239 has a half-life of 24000 years, and plutonium-240 has a half-life of 6800 years. Because of these long half-lived radioactive elements, spent fuel must be isolated and stored in waste containers. This high-level nuclear wastes also can result in health problems such as cancer, an increase in environmental temperature and radiation.

1.3 Storage of nuclear wastes

Nuclear wastes of the high-level should be stored in a segregated method such that it can be retrieved for further treatment, or to be transferred to another storage facility or for disposal. Isolation of the waste may also reduce the exposure risks and may limit the severity of any consequences under accident conditions . There are many reasons why it may be appropriate to store radioactive wastes for varying periods of time which include [Iae06]:

- To allow the decay of short-lived radionuclides to a level at which the radioactive wastes can be released, discharged or recycled.

- To collect and accumulate a sufficient amount of radioactive wastes prior to its transfer to another facility for treatment and conditioning.
- To collect and accumulate a sufficient amount of radioactive wastes prior to its disposal.
- To reduce the heat generation rate of high-level radioactive wastes prior to its disposal and, in some cases, prior to steps in its predisposal management.
- To provide long term storage of nuclear wastes in places lacking a suitable disposal facility.

1.3.1 The wastes storage method

There are two methods in which nuclear waste can be stored [Nrc02] [Nrc13]:

1.3.1.1 Wet storage method

Currently, most spent nuclear fuels are stored and segregated in specially designed pools at individual reactor sites. The wet storage method involves storing spent fuel in rods under at least 20 feet of water (see Fig. 1.1a), which provides adequate shielding from the radiation near the pool site. Most pools were originally designed to store several years of spent fuel. Due to delays in developing disposal facilities for the spent fuel, most of the pools were designed to allow a greater number of spent fuel rods to be stored.

1.3.1.2 Dry storage method

When pool capacity began to fill up, nuclear institutions began to look for alternative methods of storing spent nuclear fuel. One of the alternative options is the dry storage system. In this method, spent fuel is surrounded by inert gas inside a container which is also called a cask-see Fig. 1.1b. The casks are usually made of metals such as copper, iron, stainless steels, titanium alloys, and nickel-based alloys or concrete. Some of these casks can be used for both long term storage and transportation. Most nuclear power plants are currently storing spent fuel under the dry storage option.

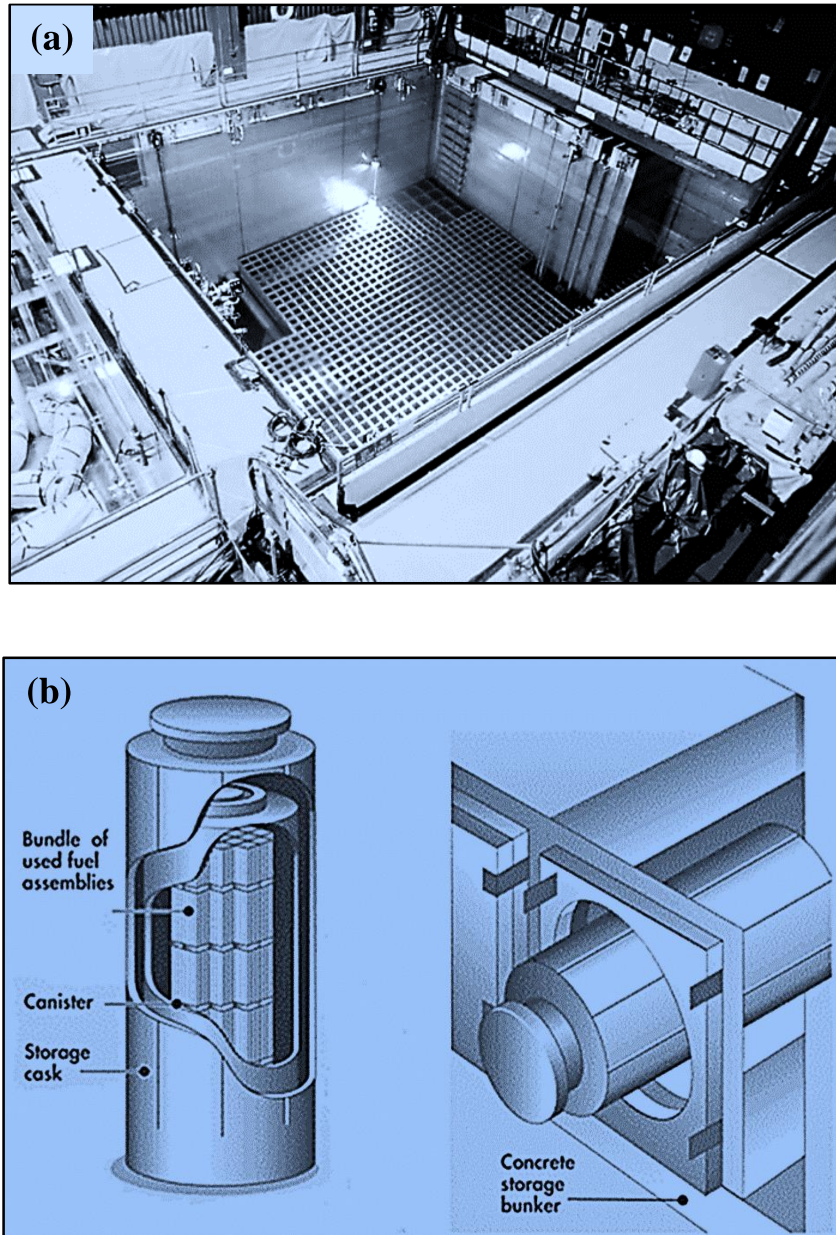

Fig. 1.1: A configuration for spent fuel waste storage (a) Wet storage (b) Dry storage methods [www1] [Nrc13].

1.4 Motivation and research objectives

The storage of radioactive waste must ensure that both human health and the environment will be protected, both now and in the future. The performance of the materials used in nuclear wastes are important during the entire process of waste management. A key consideration in nuclear-waste management is the development of a highly durable waste container (including

the cask and the surrounding container barriers) that ensures the long-term stability of materials and the isolation of radioactivity. Candidate materials that are being used for fabricating the cask are generally metals such as copper, iron, stainless steels, titanium alloys, and nickel-based alloys. Certain ceramics or graphitic materials may also be considered [Yim00]. Copper is one of the few metals which has a very good environmental durability, however, it is known to be poor in brine as well as in radiation environment [Wer92]. Iron steel provides good predictability since much is known about the material. It is not very corrosion-resistant but is less prone to catastrophic failures. Titanium alloys are mechanically strong and possess good corrosion resistance, however, they can experience brittle failure with the uptake of hydrogen. Nickel-based alloys, such as Incoloy and Hastelloy, are very corrosion resistant similar to titanium. They are easier to weld than titanium but could be more expensive. Stainless steels have good mechanical properties and are very corrosion resistant, but catastrophic failures are possible through stress-corrosion cracking as well as being very expensive [Yim00]. Ceramic materials, such as graphite and silicon carbide, have excellent corrosion resistance and are abundant. However, mechanical strength is a problem with graphite.

Due to physical and chemical stresses during transportation, interim storage and disposal, various forms of degradation can be expected. The main objective of this study is to investigate the feasibility of glassy carbon to be a good alternative material for constructing the casks used for nuclear waste storage [Mal18]. In order to do this, glassy carbon was implanted with one of the significant fission products namely Xe ions. One of the main problems in the dry method of nuclear storage is degradation over time due to heat. In order to investigate if glassy carbon is able to retain its thermal resistance, the implanted glassy carbon annealed at different temperatures. The low reactivity and gas impermeability of glassy carbon is attributed to its structure and properties, therefore, it is important that glassy carbon retains its structure even after ion bombardment and heat treatment. The structure of the glassy carbon was monitored after ion bombardment and heat treatment at different temperatures using Raman spectroscopy and transmission electron microscopy (TEM). The migration behaviour of Xe ions in glassy carbon due to heat treatment were investigated. The change in the surface morphology and roughness of glassy carbon were also investigated.

1.5 The outlay of the thesis

This thesis contains 9 chapters organized as follows: **Chapter 1** is the introduction and it gives a general overview of nuclear power and nuclear wastes as well as the methods of storing nuclear wastes. **Chapter 2** discusses carbon material and its allotropes, the structures, properties and applications. **Chapters 3** discusses the theory of ion implantation, general conception. Diffusion and the theory of diffusion is discussed in **Chapters 4**, while **Chapter 5** gives a general overview of some of the analytical techniques such as Rutherford backscattering spectrometry (RBS), Raman spectroscopy and scanning electron microscopy (SEM) which were used during the study. The experimental procedures including the annealing processes are discussed in **Chapter 6**. The results and discussions are presented in **Chapter 7**. The conclusions drawn from the results are given in **Chapter 8** as well as recommendations for future research work that still needs to be done. Research outputs from this work in **Chapter 9**.

References

[Cso83] Gy. Csom, I. Nemes, J. Ozorai, E. Szondi, Xenon-poisoning under non-stationary operating conditions in wwer-440 reactor, Training Reactor, Technical University of Budapest, Hungary, 1983.

[Dia03] B. Diacon, W. J. Garland, Xenon Effects on Nuclear Reactor Reactivity, Engineering Physics 4D03 Course Notes, McMaster University.

[Giu07] G. Giuliani, A. De Bono, S. Kluser, P. Peduzzi, Environment Alert Bulletin, UNEP, Europe, 2007.

[Iae06] IAEA, safety standards: Storage of radioactive waste, Vienna, 2006.

[Iae06] IAEA, Development of Specifications for Radioactive Waste Packages, Vienna, 2006.

[Mal18] Johan B. Malherbe, O.S. Odutemowo, E.G. Njoroge, D.F. Langa, T.T. Hlatshwayo, C.C. Theron, Ion bombardment of glassy carbon, Vacuum **149** (2018) 19 – 22.

[Nag15] S. Nagasaki, S. Nakayama (eds.), Radioactive Waste Engineering and Management, An Advanced Course in Nuclear Engineering. DOI 10.1007/978-4-431-55417-2.

[Nrc02] US Nuclear regulatory commission, Radioactive Waste: Production, Storage, Disposal, NRC, Washington, DC, 2002.

[Nrc13] U.S. Nuclear Regulatory Commission, Dry Cask Storage of Spent Nuclear Fuel, NRC, USA, 2013.

[Rah06] T. Rahola, M. Markkanen, Storage of low-level radioactive waste and regulatory control of sealed sources in Finland, STUK - Radiation and Nuclear Safety Authority, Finland, 2006.

[Rog00] P. L. Roggenkamp, The Influence of Xenon-135 on Reactor Operation, (2000) 49 – 56.

[Sae10] P. R. J. Saey, Radionuclides in the Environment: Xenon, John Wiley & Sons, Austria, 2010.

[Wer92] L. Werme, P. Sellin, N. Kjellbert, Copper canisters for nuclear high level waste disposal. Corrosion aspects, Swedish Nuclear Fuel and Waste Management Co., 1992.

[www1] www.irsn.fr, Radioactive waste management, Thematic series, IRSN, France,

2013. Accessed October 26, 2019.

[Yim00] M. Yim, K.L. Murty, Materials issues in nuclear-waste management, *Journal of the Minerals, Metals & Materials Society* **52** (2000) 26 – 29.

CHAPTER 2

CARBON MATERIAL AND ITS ALLOTROPES

Carbon is one of the most significant elements among all other elements. It is a unique and abundant chemical element in nature, with symbol C which consists of 6 protons and 6 electrons (^{12}C). Carbon can exist in more than 95% of all known chemical elements and consists of a large number of allotropes [Hir10]. It exists in nature in three pure forms namely: diamond, graphite, amorphous carbon and in synthetic forms such as glassy carbon and fullerenes. It all has four valence electrons so they can easily bond with other carbon atoms to form long chains or rings [Fal07]. Carbon has an outstanding ability to form different hybridization (sp^3, sp^2 and sp^1).

Carbon materials appear in different crystalline forms as a result of the three different types of bonding known as hybridization, which is sp^3, sp^2 and sp^1 as shown in Fig. 2.1. The first hybrid is the sp^1 (linear coordination), second is sp^2 (trigonal) and the third is sp^3 (tetragonal). Diamond is known as pure sp^3 hybridization and graphite is pure sp^2 hybridization, while amorphous carbon has sp^2 with fraction of sp^3 hybridization [Miy98].

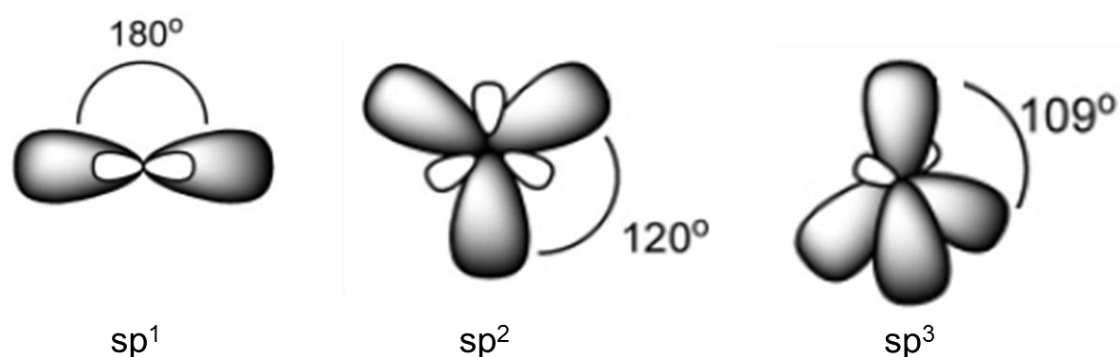

Fig. 2.1: Three different types of hybridization and their hybrid orbitals [Kru10].

In the sp^1 configuration, two of the four hybrid orbitals mix together. These two orbitals are repulsive and therefore form an angle of 180°, which makes the sp^1 molecule linear [Kru10].

The sp^1 bond forms σ bonds directed along ± x-axis and the other two electrons enter π orbitals in the y and z directions.

In the sp^2 configuration, when three of the four hybrid orbitals mix (an s and two p orbitals) to form trigonal sp^2 orbitals with the neighbouring atoms at 120° i.e. graphite structure, which form σ bonds in a plane [Pie13]. The free valence electron (pz) lies in a pπ orbital, with an axis perpendicular to the sp^2 hybrid orbitals. The π orbital forms a weaker bond with a π orbital on one or more neighbouring atoms [Ans06].

In the sp^3 configuration, i.e. in diamond structure, the four hybrid orbitals are assigned to be tetrahedrally directed to sp^3 orbital, which makes a strong σ-bond to an adjacent angle [Lin11].

2.1 Allotropes of carbon: Structure, Properties and Applications

The allotropes of carbon can be classified in two forms; natural and artificial as are shown in the fig. 2.2 below.

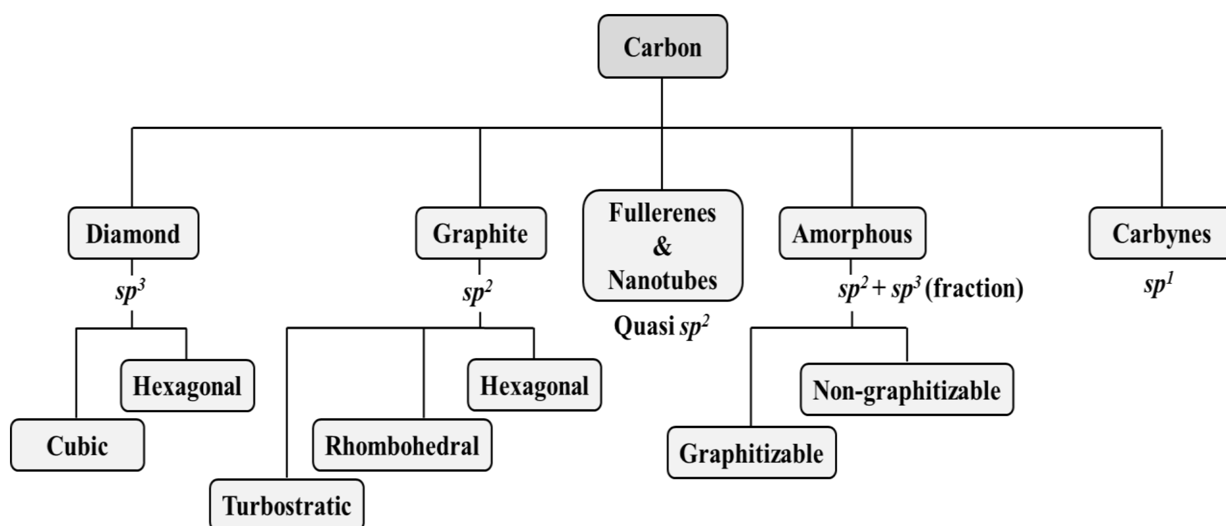

Fig. 2.2: Schematics showing the different allotropes of carbon.

2.1.1 Graphite

Graphite comprises of series of infinite layers of sp^2 hybridized carbon atoms. Each carbon atom is bonded to three others to form a planar array of hexagons. The weak van der Waals force keeps the graphene layers stacked together, 0.3354 nm apart [Fal07]. Graphite exists in three forms namely: hexagonal, rhombohedral and turbostratic as shown in Fig. 2.3 (a – c) below. The most common form is the hexagonal graphite which is arranged in an ABAB sequence which is shown in Fig. 2.3 (a). The ABAB sequence has an in-plane nearest-neighbor distance of 0.1421 nm, inter-planar separation of 0.3354 nm, an in-plane lattice parameter a_o of 0.2456 nm and a c-axis parameter of 0.6708 nm [Dre96] [Pie93].

Hexagonal graphite (Fig. 2.3 a) is thermodynamically stable at room temperature and ambient pressure and found in all synthetic materials. Rhombohedral graphite (Fig. 2.3 b) is unstable and is stacked in the ABCABCABC sequence [Pie93] [Miy98]. It has an in-plane lattice parameter of 0.2256 nm and a c-axis parameter of 1.0006 nm. It is never found in pure form but always in combination with hexagonal graphite. It usually reverts to the hexagonal form during heat treatment above 1300 °C [Pie93]. Turbostratic graphite is graphite in which there is a relatively random rotation of adjacent graphene layers which then results in stacking faults [Zha17]. Hence, there is no consistent interlayer spacing between the layers, whereas interlayer spacing ranging from 0.344 nm to 0.370 nm [Pau66]. As a consequence, there is no more interaction between the layers, and the orientation of individual planes no longer has an influence on the effective forces.

(a)

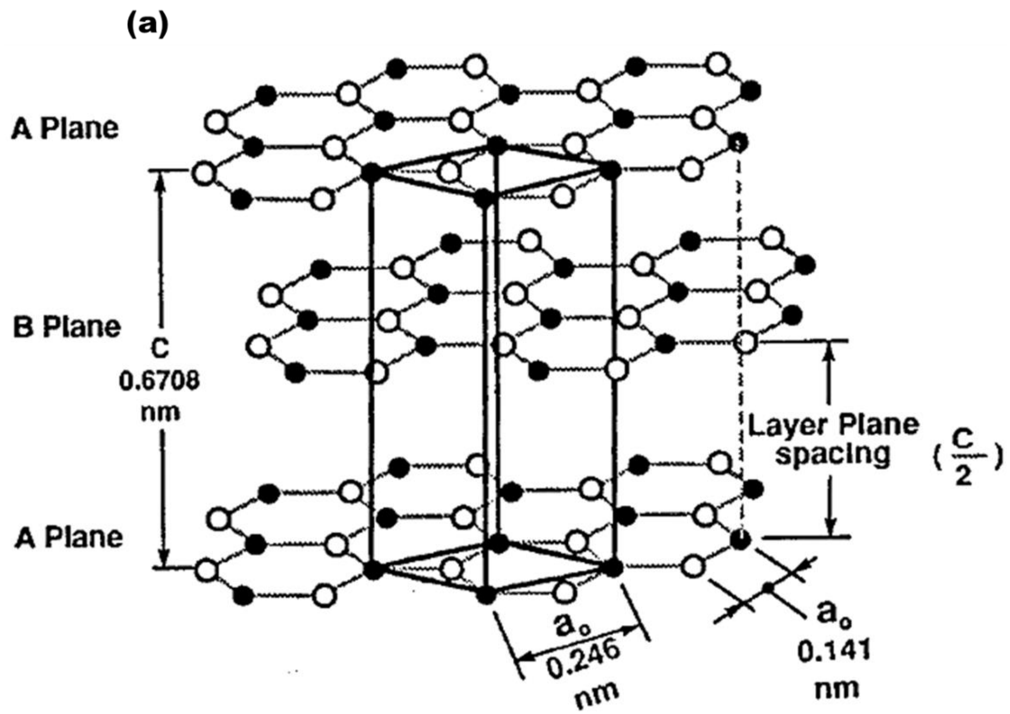

(b)

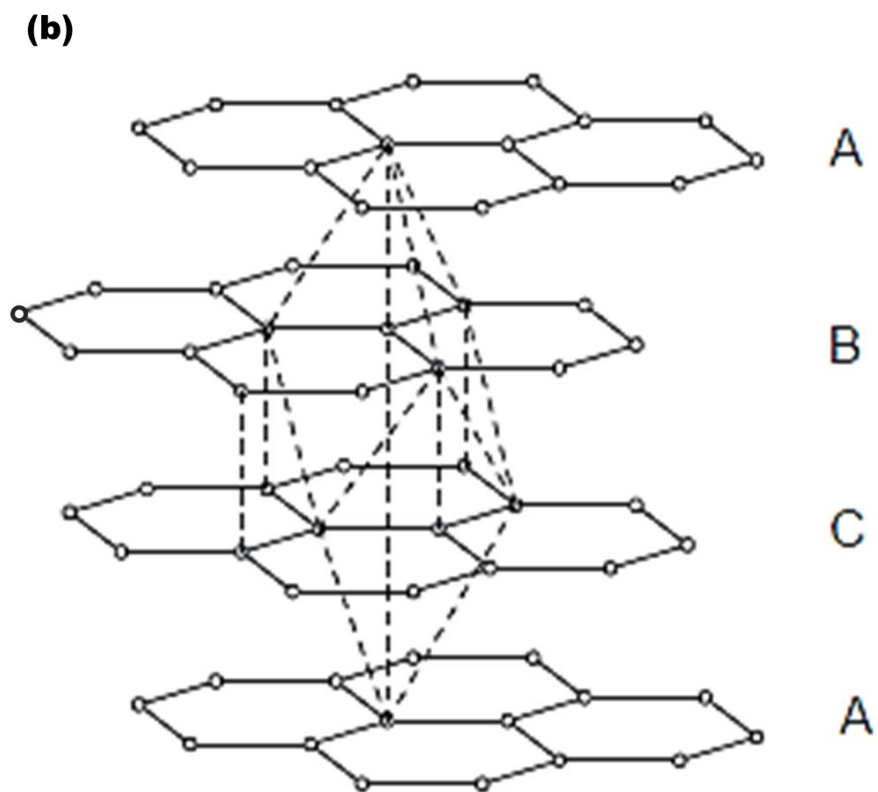

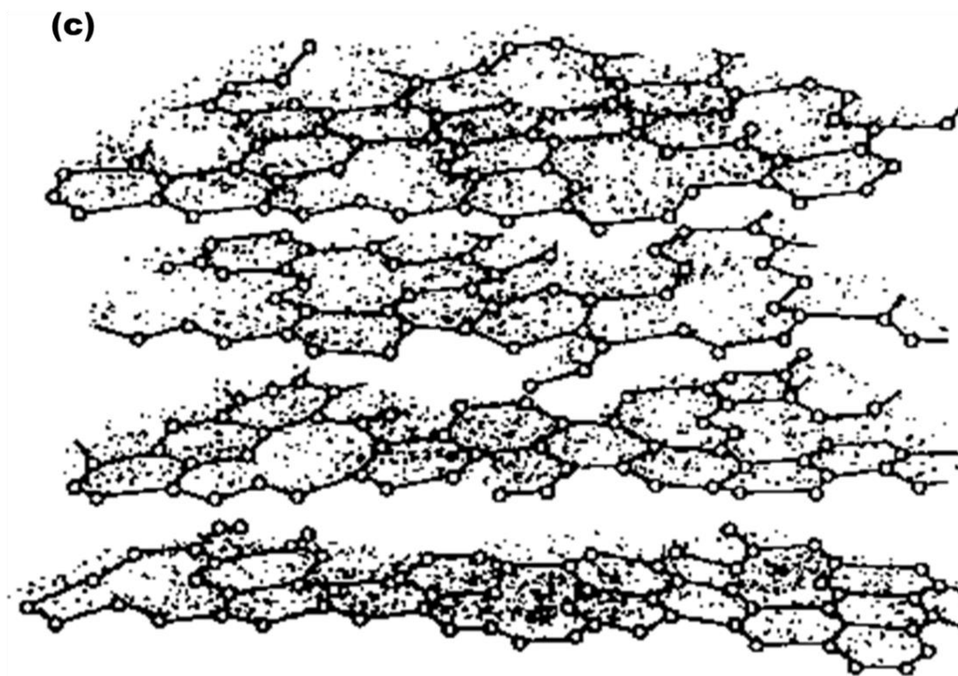

Fig. 2.3: Crystal structure of different forms of graphite showing the (a) Hexagonal (b) Rhombohedral (c) Turbostratic stacking sequence [Pie93] [Zha17].

2.1.1.1 Properties of graphite

The sp^2 hybridization is formed when three of the four hybrid orbitals mix (an s and two p orbitals) to form three sp^2 orbitals and unhybridized free p orbital electrons- see fig. 2.2. The three sp^2 orbitals formed are coplanar and form an angle of 120° between each other [Pie13]. They form σ-bonds by overlapping with orbitals of neighbouring orbitals. The free valence electron (p_z) lies in the π orbital with an axis perpendicular to the sp^2 hybrid orbitals where it forms a weak π bond [Ans06]. A common example of a trigonally hybridized structure is graphite. The structure and properties of graphite will be discussed later in this chapter.

The unusual crystal structure of graphite results in a considerable anisotropy. The properties of graphite may vary considerably when measured along the ab axis (within the plane) or the c direction (perpendicular to the planes). The table below gives some of the physical and chemical properties of hexagonal graphite.

Table 2.1: Some properties of hexagonal graphite [Pie93] [Miy98].

Property	Value
Lattice parameters	a_o = 0.2456 nm c_o = 0.6708 nm
Colour	Black
Density (1 atom)	2.26 g/cm^3
Compression strength	0.065-0.089 GPa
Atomic volume	5.315 cm^3/mol
Boiling point	4560 K
Carbon-carbon bond distance	0.1421 nm
Atomic number density	1.14×10^{23} atoms/cm^3
Melting point	4450 K
Heat of vaporization	355.8-598.2 kJ/mol
Thermal conductivity at 25 °C	Pyrolytic graphite: ab directions 190-398 W/m.°C c direction 1-3 W/m.°C
Specific heat capacity at 25 °C	0.690 - 0.719 kJ/kg-K
Coefficient of thermal expansion at 25 to 200 °C	Pyrolitic graphite: ab directions, -1 to 1 10^{-6}/ °C c direction, 15-25 10^{-6}/ °C
Binding energy	7.4 eV/C atom
Magnetic susceptibility	0.141×10^{-6} cm^3/g

2.1.1.2 Applications of graphite

Graphite is one of the most significant materials used in the manufacturing and laboratory applications depending on its type. Some applications of graphite such as nuclear, chemical, electrical and mechanical are listed below [www1]:

i. Due to its high thermal and neutron radiation resistance, graphite is used in the nuclear industry as materials for producing moderator rods in nuclear reactors.

ii. In the chemical industry/laboratory, graphite is also used as an electrode in the production of chemicals such as calcium carbide and halogens.

iii. Graphite used in the manufacture of carbon brushes for electrical motors.

iv. The mechanical properties of graphite also allow it to be used in the manufacture of engineering materials such as piston rings, shafts, thrust bearings, etc. Carbon-based seals also employed in the fuel pumps and shafts of aircraft jet engines.

2.1.1.2 Diamond

Diamond consists of sp^3-hybridized carbons, where the covalent chemical bonds extend three-dimensional. Diamond has two crystal structures, a cubic symmetry which is the more common and stable and hexagonal symmetry, less common and lower hardness found in nature as mineral Lonsdaleite [fal07] [Pie93]. In diamond, each tetrahedron of the hybridized carbon atom combines with four other hybridized atoms (tetrahedral). The resulting structure is a strong covalent bonded structure as shown in Fig. 2.4(a). The covalent bond between the carbon atoms of the diamond is characterized by a short bond length of 0.154 nm and high bond energy of 711 kJ/mol [Miy98].

The cubic structure of diamond can be visualized as stacking of puckered infinite layers (the {111} planes), or as two face-centred interpenetrating cubic lattices, one with the origin at (0, 0, 0) and the other at (1/4, 1/4, 1/4) with parallel axes. The stacking sequence of the {111} planes is ABCABC so that every third layer is identical [Dre96] [Pie93]. The in-plane lattice parameter of a cubic diamond is given as $a_o = 0.3567$ nm (at 25 °C and 1 atom). The nearest-neighbour C-C distance is 0.1544 nm, nearly 10 % larger than in graphite. And the atomic density of diamond (1.77×10^{23} cm^{-3}) which is 56 % higher than in graphite, due to the high anisotropy of the graphite structure.

Hexagonal diamond (Lonsdaleite) is extremely rare in nature. The hexagonal lattice is similar to a cubic relative and is built from tetrahedrons of carbon, but these are arranged in a different stacking sequence as shown in Fig. 2.4(b). The lattice parameters are $a_o = 0.252$ nm and $c_o =$ 0.412 nm. Both cubic and hexagonal diamonds are isotropic, three-dimensional structures with every atom tetrahedrally surrounded by four neighbours. Hexagonal diamond has an ABAB

stacking sequence, the *c*-axis of 0.206 nm, considerably smaller than the interplanar separation of 0.335 nm for graphite [Kru10] [Bun67].

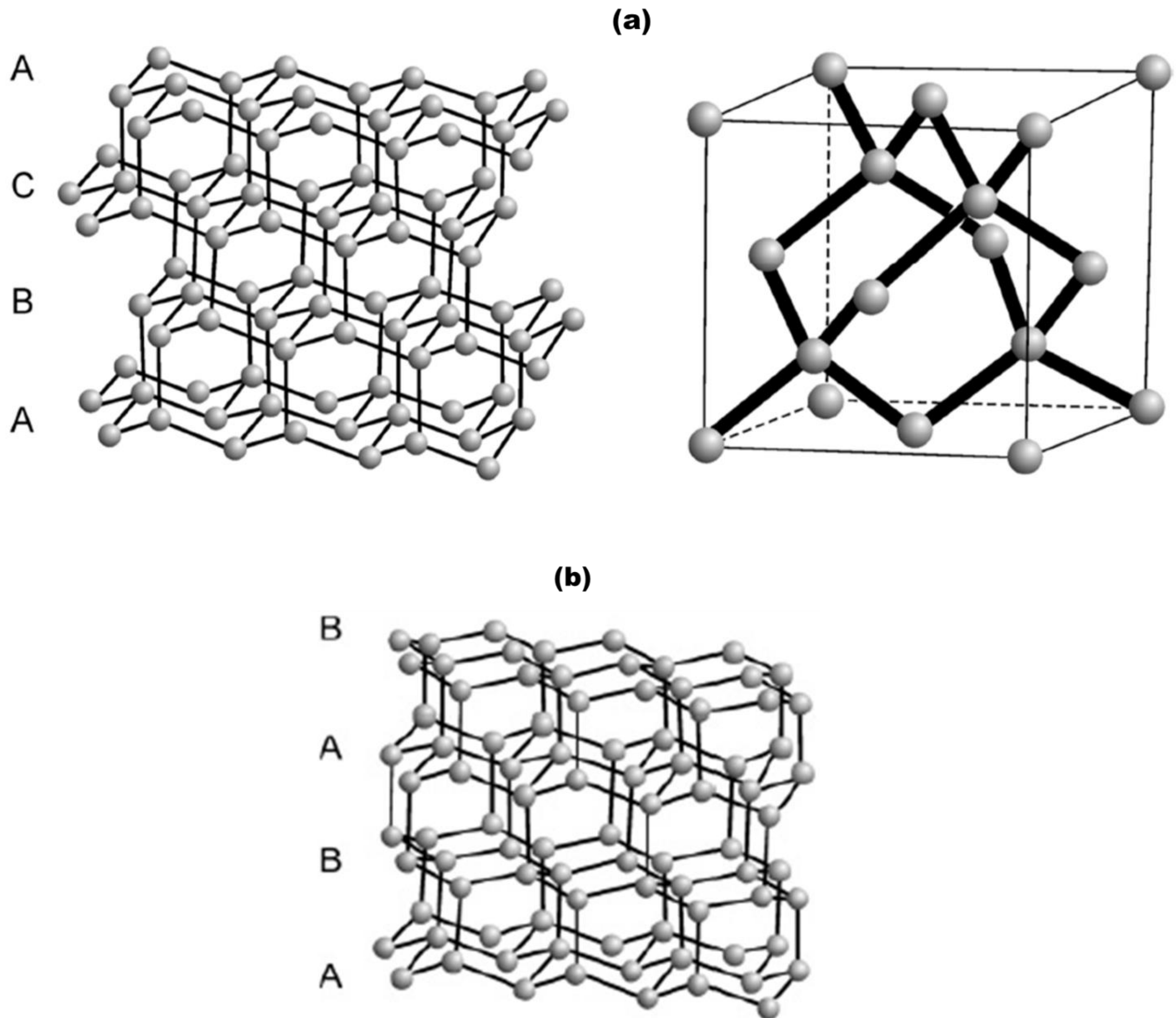

Fig. 2.4: Lattice structure of (a) cubic diamond (b) hexagonal diamond [Kru10].

2.1.2.1 Properties of diamond

The table 2.2 gives some of the physical, thermal, electrical and optical properties of diamond.

Table 2.2: Some properties of cubic and hexagonal of diamond [Pie93] [Dre96] [May00] [Hay17].

Property	Value	
Lattice Structure	*Cubic symmetry*	*Hexagonal symmetry*
Lattice constant (300 K)	0.3567	a_o = 0.252 nm c_o = 0.412 nm
Density (1 atom)	3.515 g/cm^3	3.52 g/cm^3
Carbon-Carbon bond distance	0.15448 nm	0.154 nm
Thermal conductivity (300 K)	2100 W/(m.K)	
Atomic number density	1.77×10^{23} atoms /cm^3	
Melting point	4500 K	
Mechanical hardness	90 GPa	
Bulk Modulus	1.2×10^{12} N m^{-2}	
Specific heat capacity (25 ^{o}C)	0.502 J/gK	
Sound propagation velocity	17.5 km/s^{-1}	
Bandgap	5.47 eV	
Compressibility	8.3 ×10^{-13} m^2 N^{-1}	

2.1.2.2 Applications of diamond

Diamond is one of the most coveted gems. It also has quite a number of industrial and laboratory applications due to its hardness, mechanical properties, high thermal conductivity, and excellent electrical insulating properties [www2] [May00]. Some of the applications of the diamond are listed below:

i. Due to its hardness diamond is mostly used in cutting, grinding, drilling, and polishing tools.

ii. Diamond can also be used in making tungsten wires, using for some labs equipment.

iii. Diamond is transparent over a wide spectral range, hence, it can be used for special spectroscopy applications especially in the UV region.

iv. Diamond has a high thermal conductivity it can be very good heat conductors.

2.1.3 Amorphous carbon

Amorphous carbon consists of carbon with varying mixture of tetrahedral (sp^3), trigonal (sp^2) and sometimes linear (sp^1) bonds. It has been considered as the third allotrope of carbon, although lacking any crystallinity and often containing significant amounts of hydrogen. These allotropes of carbon are included i.e. diamond-like carbon (DLC), glassy carbon, fullerenes, nanotubes, and the carbynes. Amorphous carbons are usually prepared by pyrolysis of organic polymer or hydrocarbon precursors at temperatures below 1500 ^{o}C. The nature of the starting material and the preparation history strongly influences the structural development and final properties upon further heat treatment [Fal07] [Rob96].

2.1.3.1 Diamond-like carbon

Diamond-like carbon (DLC) is amorphous carbon containing a significant fraction of sp^3 bonding, sometimes called highly tetrahedral amorphous carbons (ta-C). It commonly describes a family of metastable amorphous carbon. DLC is usually formed as thin films under specific deposition conditions, such as ion beam deposition (IBD) or chemical vapour deposition (CVD). The unique properties of diamond-like carbon and their modifications together make it suitable for a variety of applications. The exploited properties include the high hardness, high wear resistance and low friction coefficients, chemical inertness, and high electrical resistivity. Due to their chemical inertness and is impermeable to gases, it can be used against corrosion and diffusion barriers. Presently, DLC and its modifications are being considered as low dielectric materials for the interconnecting structures [Gri99].

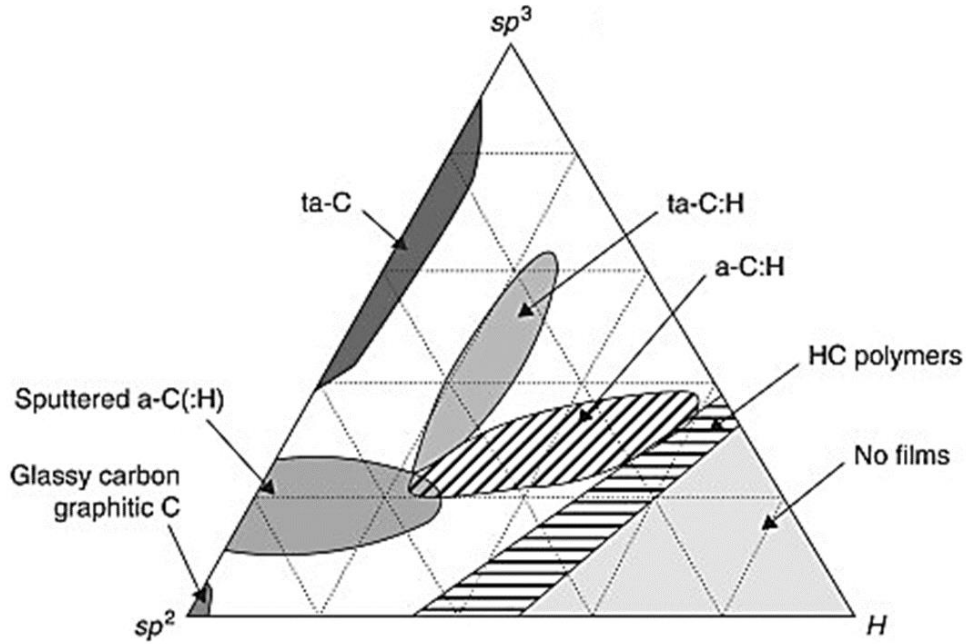

Fig. 2.5: Phase diagram of diamond-like carbon materials [Gri99].

2.1.3.2 Fullerenes

Fullerenes are one of the synthetic allotropes of carbon which have been discovered in recent years. Unlike graphite and diamond, the fullerenes do not found in a single material, but always as a family of molecular. The molecules are edgeless, have no charge, and have no boundaries, no dangling bonds, and no unpaired electrons [Pie93]. The fullerene hybridization is a modification of the sp^3 hybridization of diamond and sp^2 hybridization of graphite. The carbon atoms in the fullerene matrix are in such a way that the σ orbitals do not contain all the s-orbital character and the π-orbitals also do not contain the p-orbital character. The fullerene hybridization has variable characteristics depending on the number of carbon atoms in the molecule. This number varies from many fullerene structures that are identified and structurally characterized, the smallest structure of the fullerene family is the C_{20}. There are many fullerene structures such as C_{60}, C_{70}, C_{76}, C_{78} and C_{84} [Pie93] [Dre96]. The first stable, the most common fullerene hybridization and the first to be discovered is the C_{60} as shown in Fig. 2.6. Fullerene C_{60} consists of interconnected pentagons and hexagons and it is most likely to be a major constituent of soot (carbon black).

.

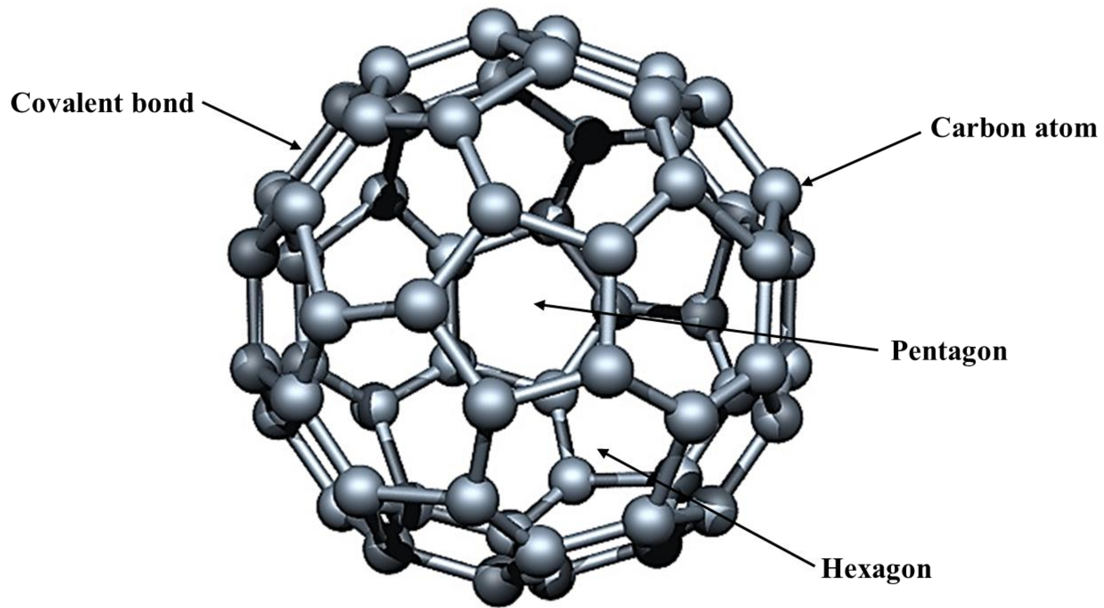

Fig. 2.6: Molecular structure of C_{60} fullerene [Ans06].

2.1.3.2.1 Properties of fullerenes

The table below gives some of the physical properties of fullerenes.

Table 2.3: Some physical properties of fullerene C_{60} molecules and its crystalline structure [Dre96].

Property	Value
Lattice structure	*face centred cubic (fcc)*
Lattice constant	1.417 nm
Density (1 atom)	1.72 g/cm^3
Molecular number density	1.44×10^{21}/cm^3
C_{60}-C_{60} bond distance	1.002 nm
C_{60}-C_{60} cohesive energy	1.6 eV
Thermal conductivity (300 K)	0.40 W/(m.K)
Electrical conductivity (300 K)	1.7×10^{-9} S/m
Melting point	1180 ^{o}C

Sublimation temperature	434 °C
Bulk modulus (300 K)	6.8 Gpa
Compressibility	6.9×10^{-11} m^2 N^{-1}

2.1.3.2.2 Applications of fullerenes

Due to its very interesting physical properties of C_{60}, which can be used in solar cells and biological applications [Fal07].

2.1.3.3 Glassy carbon

Glassy carbon (also known as vitreous carbon or glass-like carbon) is another synthetic allotrope of carbon. It is manufactured by the carbonization of organic polymers (plastics). The organic polymers are usually heated very slowly (usually under pressure) at a temperature ranging from 1000 °C to 3000 °C. Glassy carbon is described as cross-linked by carbon-carbon covalent bonds polymeric chains with random orientation. Additionally, glassy carbon has a low density which implies that it has high porosity, however, the permeability of the material is extremely low. This means that the pores are extremely small and impermeable to all gases. The pore diameters of 0.1 to 0.3 nm and 0.35 nm after heat-treatment up to 3000°C [Pie93].

To ensure that the polymeric precursor used in the fabrication of the glassy carbon product possesses the following characteristics:

- The structure of the molecule must be three-dimensionally cross-linked.
- Carbonization must occur in the carbon state, without mesophase formation, and result in the formation of a char.
- The number of benzene rings from the degree of aromatic must be high to provide high carbon yield.

The physical and mechanical properties of the glassy carbon manufactured are determined by the carbonization temperature. There are two common types of glassy carbon materials

produced at different temperatures, are the Sigradur® G and Sigradur® K glassy carbon . The Sigradur glassy carbons are produced from phenolic resins by pyrolysis in an inert atmosphere at temperatures up to 1000 °C (Sigradur® K) and 3000 °C (Sigradur® G).

Glassy carbon materials are manufactured by HTW Hochtemperature-Werkstoffe GmbH manufacturer [www3]. However, their physical and mechanical properties vary significantly due to the different carbonization temperature of each. Table 2.4 shows some of the properties of Sigradur® K and G types of glassy carbon as stated according to the manufacturer [www3] [Pie93].

Property	**Sigradur® K**	**Sigradur® G**
Maximum service temperature (vacuum and inert gas)	1000 °C	3000 °C
Density	1.54 g/cm^3	1.42 g/cm^3
Open porosity	0 %	0 %
Permeability coefficient	10^{-11} cm^2/s	10^{-9} cm^2/s
Vickers hardness	340 HV	230 HV
Flexural strength	210 MPa	260 MPa
Young's modulus	35 GPa	35 GPa
Compressive strength	580 MPa	480 MPa
Specific electrical resistance (30 °C)	50 Ωμm	45 Ωμm
Thermal conductivity (30 °C)	4.6 W/(km)	6.3 W/(km)
Median linear coefficient of expansion (20-200 °C)	3.5×10^{-6}/K	2.6×10^{-6}/K

From their physical properties, obviously, the Sigradur® K glassy carbon has a higher hardness and density compared to Sigradur® G glassy carbon. But the Sigradur® G type is the preferred choice for this study because of its higher thermal conductivity, high corrosion resistance and extremely high-temperature resistance (about 3000 °C) compared to Sigradur® K.

2.1.3.3.1 Structure of glassy carbon

The structure of glassy carbon has been of major interest to researchers, and several structural models proposed since it was first fabricated in the 1960s. The first model by Noda and Inagaki [Nod64] suggested that glassy carbon consists of a three-dimensional structure consisting of a

network of trigonal carbon atoms. The model also includes both tetrahedral parts (*T*-parts) and graphitic parts (*G*-parts) as shown in Fig. 2.7(a). From the observation the X-ray diffraction pattern of glassy carbon, Noda and Inagaki [Nod64] [Nod68] deduced that T part of the glassy carbon structure corresponds to a normal covalent bond (with the neighbouring distance of 1.55 Å) which is typically found in tetrahedral carbons such as diamond. The first neighbour distance of the G part was found to be 1.42 Å which is typical to graphite.

Kakinoki [Kak65] proposed a model which modified the model by Noda and Inagaki by considering the earlier study conducted by Yamada [Yam64] where they estimated the oxygen content in glassy carbon to be about 5-6 wt%. Kakinoki then decided to put some oxygen atoms between the graphite and tetrahedral carbon atoms (see-Fig. 2.7(b)). He suggested that the presence of oxygen in the matrix explains the non-graphitisation of glassy carbon at temperatures lower than 1100-1200 ^{o}C. He concluded that the presence of oxygen in glassy carbon can be removed by the heat treatments at temperatures as high as 2500-3000 ^{o}C. According to Jenkins and Kawamura [Jen71], the glassy carbon structure contains ribbon-like graphitic domains of sp^2-hybridized carbon atoms stacked in layers (microfibrils), irregularly twisted and entangled (Fig. 2.8).

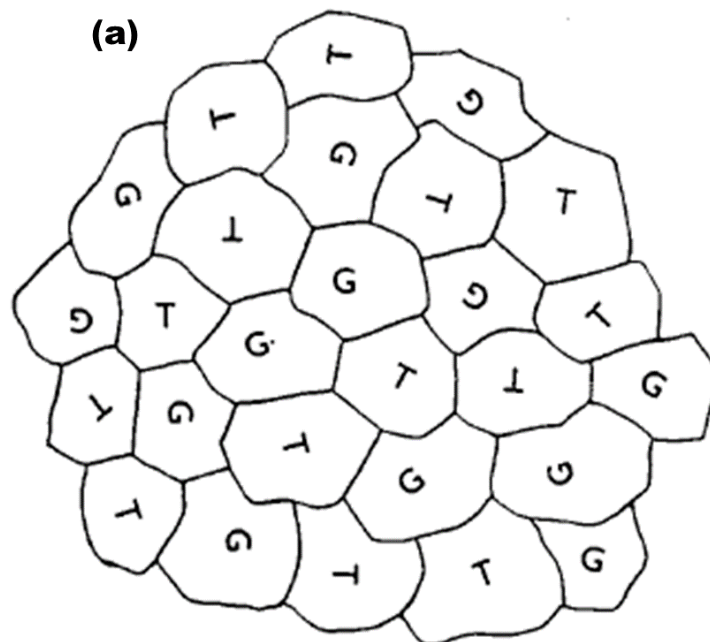

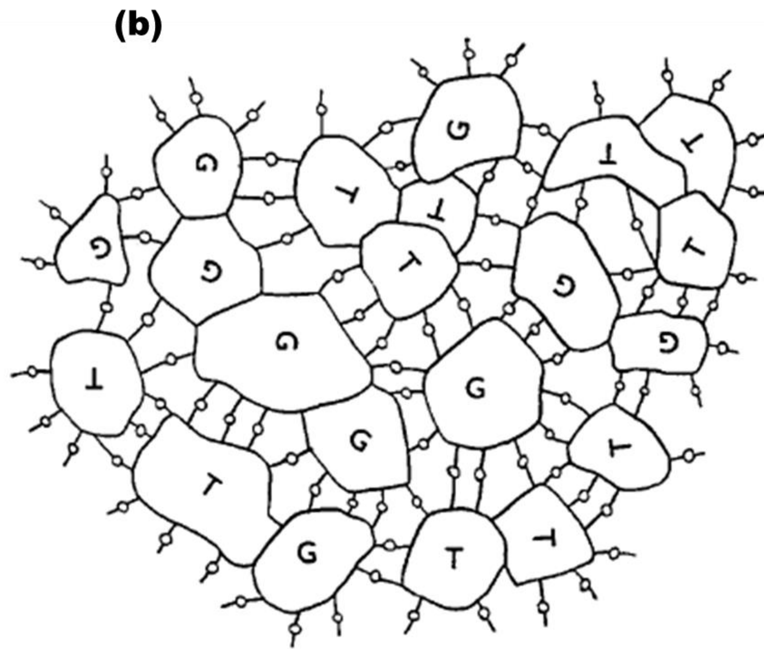

Fig. 2.7: The structural model for glassy carbon (a) proposed by Noda and Inagaki [Nod64] (b) proposed by Yamada [Yam64], oxygen bridgecontent in glassy carbon. *T* is a tetrahedral part in which the first neighbour distance is 1.55 Å and *G* a graphitic part in which the first neighbour distance is 1.42 Å.

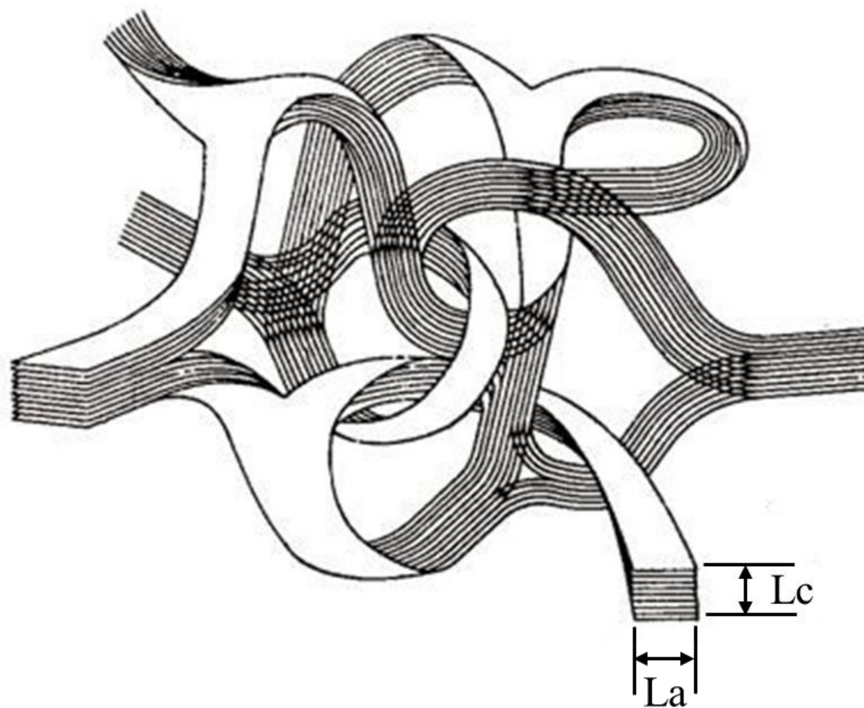

Fig. 2.8: Structural model for the network of ribbon stacks in glassy carbon proposed Jenkins and Kawamura [Pie93].

The most recent studies have suggested that glassy carbons have a fullerene-related structure [Har97] [Har05]. The presence of curvature has been attributed to the topological defects in the form of non-hexagonal carbon rings such as pentagons and heptagons that were directly observed by the high resolution transmission electron microscope (HRTEM) [Har13]. This has been attributed to its higher number of closely packed particles and tightly curled single carbon layers [Har04]. The structural model of glassy carbon proposed by Harris is shown in Fig. 2.9 below.

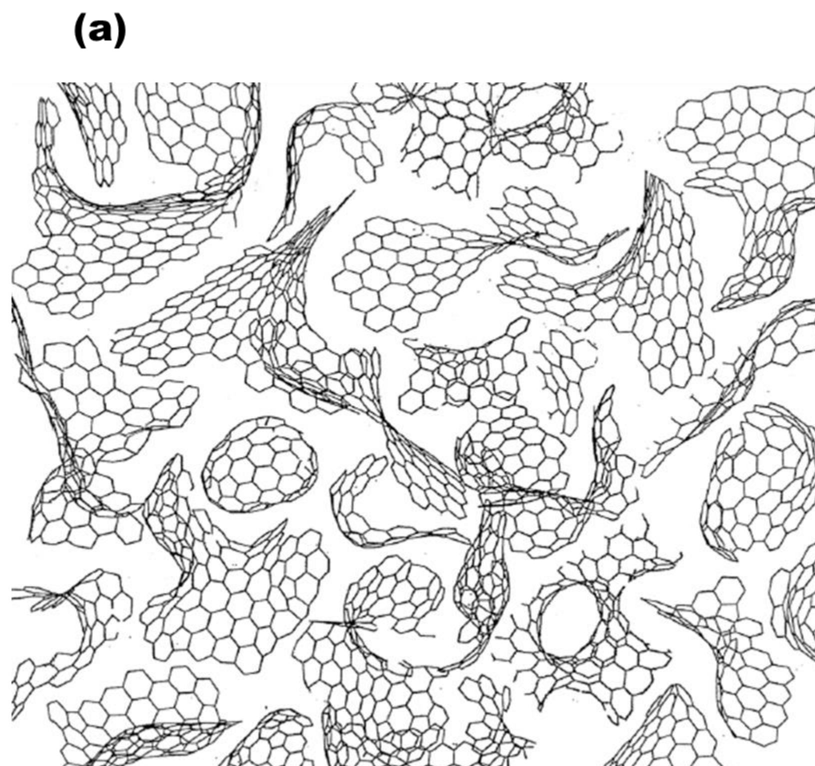

(b)

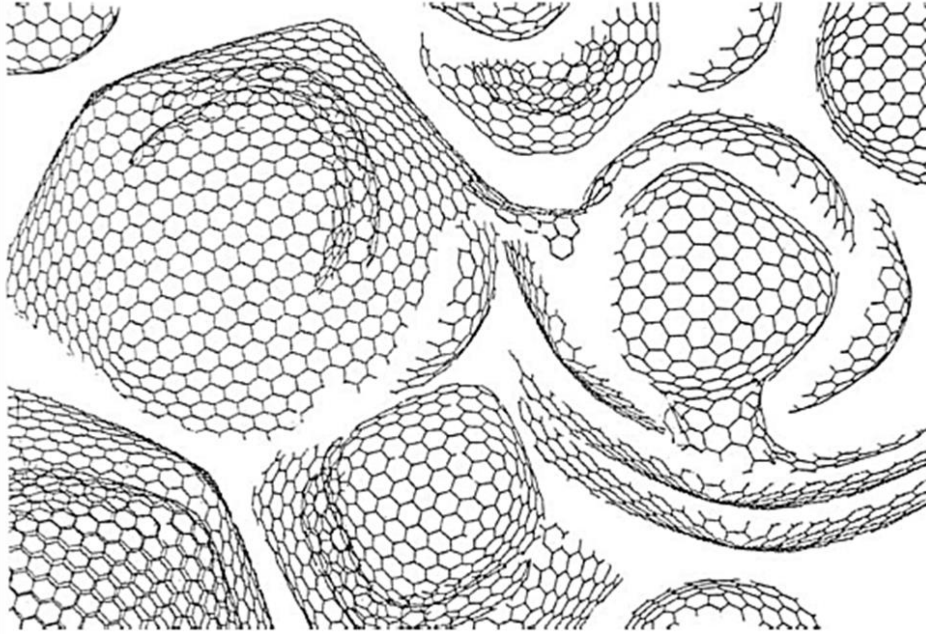

Fig. 2.9: The model of the structure of glassy carbon as proposed by Harris [Har05], (a) low-temperature and (b) high-temperature glassy carbon.

Fig 2.10 also shows the HRTEM micrograph of the virgin Sigradur® G glassy carbon (used in this study) cross-section was carried out using a Jem-3010 by JEOL [Odu18]. The image shows that glassy carbon is a typical non-graphitizing carbon accompanied by a closed carbon nanostructure. This can compare to an imperfect multi-layered fullerene which often surrounds closed pores.

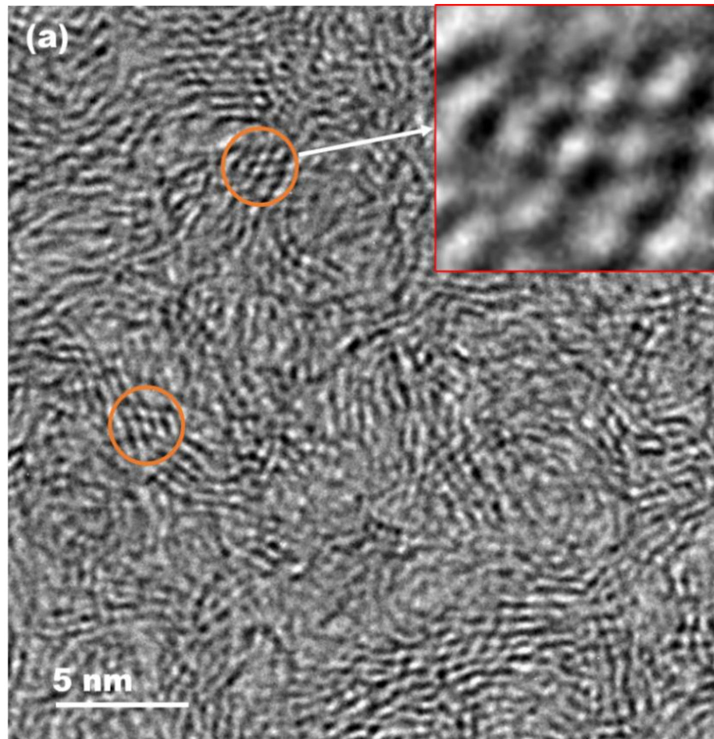
(a)
5 nm

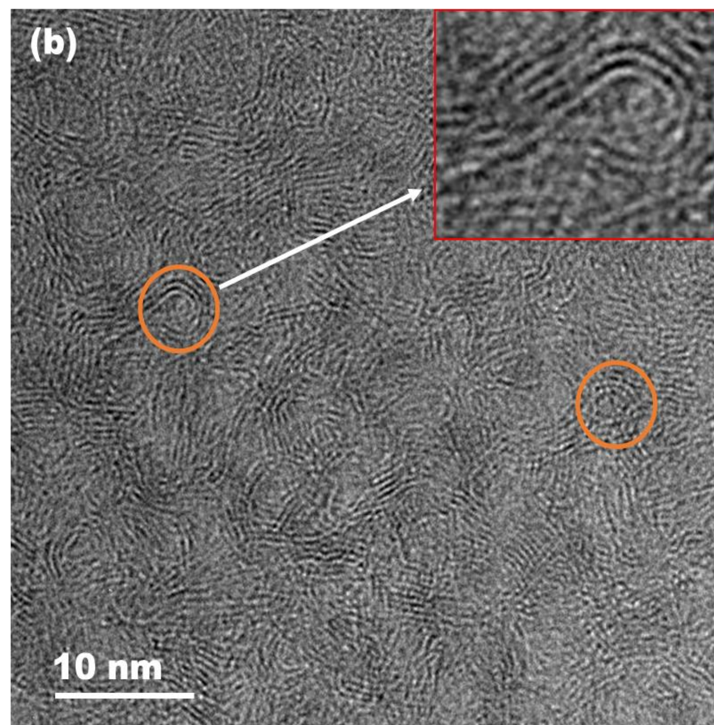
(b)
10 nm

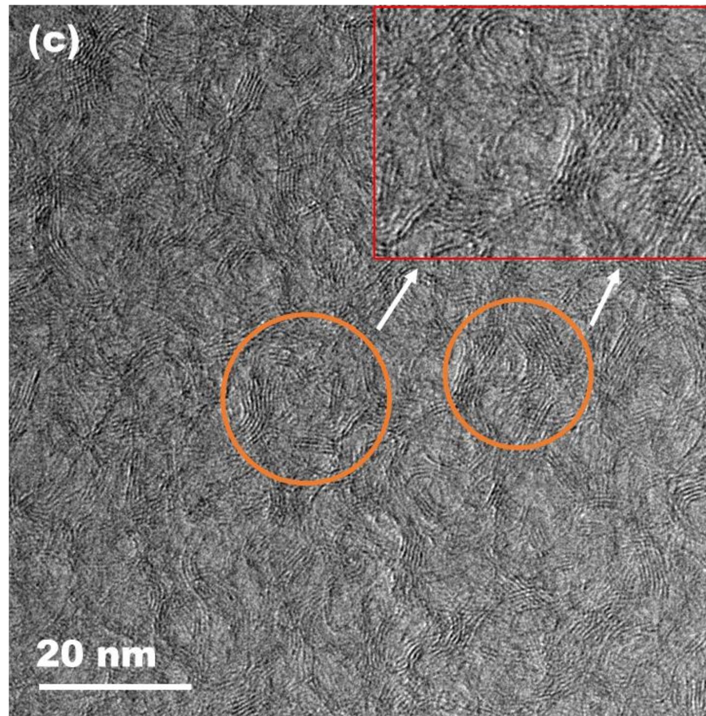

Fig. 2.10: HRTEM micrographs of virgin GC (a) closely packed particles (b) tightly curled single carbon layers (c) onion-like carbon structures. The images were obtained at different magnifications.

2.1.3.3.2 Properties of glassy carbon

The properties of glassy carbon differ from those of graphite due to the structural differences. Some of the properties of glassy carbon include [Pie93] [Har04].

i. High temperature resistance: glassy carbon is a non-graphitising carbon and cannot be transformed into crystalline graphite even at temperatures above 3000 ^{o}C.

ii. High resistance to attack by acids: glassy carbon unaffected by such treatment, when it comes in contact with concentrated sulphuric and nitric acids at room temperature even when it has been exposed for several months.

iii. Extreme corrosion resistance: the closed structure of glassy carbon does not permit it to form intercalation compounds. This feature makes it difficult for it to be corroded by acids and alkali agents.

iv. High hardness and strength: unlike most graphitic and ceramic materials, glassy carbon increases with strength with a rise in temperature up to 2430 ^{o}C.

2.1.3.3.3 Applications of glassy carbon

Based on its properties, glassy carbon can be used for several applications such as:

- Due to high temperature resistance and high thermal stability, glassy carbon has been considered as an alternative material for nuclear waste storage container. That ensures the long-term stability of materials and the isolation of radioactivity.

- Glassy carbon also highly resistant to attack by acids for several months, this property makes glassy carbon a useful material for crucibles. It is also can be used as an electrode material in electrochemistry, and its biocompatibility makes it a potential component of prosthetic devices.

- The chemical inertness and good electrical the conductivity of glassy carbon makes it a potentially excellent material for acid-battery electrodes.

References

[Ans06] E.V. Anslyn, D.A. Dougherty, Modern physical organic chemistry, University Science Books, 2006.

[Bun67] F. P. Bundy and J. S. Kasper, Hexagonal Diamond-A New Form of Carbon, *Journal of Chemical Physics* **46** (1967) 3437 – 3446.

[Dre96] M. S. Dresselhaus, G. Dresselhaus, P. C. Eklund, Science of Fullerenes and Carbon Nanotubes, Academic Press, USA, 1996.

[Fal07] E.H.L. Falcao, F. Wudl, Carbon allotropes: beyond graphite and diamond, Journal of Chemical Technology and Biotechnology, **82** (2007) 524 – 531.

[Gri99] A. Grill, Diamond-like carbon: state of the art, *Diamond and Related Materials* **8** (1999) 428 – 434

[Har97] P.J.F. Harris, Structure of non-graphitising carbons, *International Materials Reviews* **42** (1997) 206 – 218.

[Har04] P.J.F. Harris, Fullerene-related structure of commercial glassy carbons, Philosophical Magazine, **84** (2004) 3159 – 3167.

[Har05] P.J.F. Harris, New perspectives on the structure of graphitic carbons, Critical Reviews in Solid State and Materials Sciences, **30** (2005) 235 – 253.

[Har13] P. J. F Harris Fullerene-like models for microporous carbon, *Journal of Materials Science* **48** (2013) 565 – 577.

[Hay17] W. M. Haynes, D.R. Lide, CRC Handbook of Chemistry and Physics, 97th edi., CRC Press, New York, 2017.

[Hir10] A. Hirsch, The era of carbon allotropes, Nature Materials, **9** (2010) 868-871.

[Jen71] G.M. Jenkins, K. Kawamura, Structure of glassy carbon, Nature **231** (1971) 175 – 176.

[Kak65] J. Kakinoki, A model for the structure of glassy carbon, *Acta Crystallographica* **18** (1965) 578.

[Kru10] A. Krueger, Carbon materials and nanotechnology, John Wiley & Sons, 2010.

[May00] P.W. May, Diamond thin films: a 21st-century material, *Philosophical Transactions of the Royal Society London* A **358** (2000) 473 – 495.

[Miy98] K. Miyoshi, Structures and Mechanical Properties of Natural and Synthetic Diamonds, Lewis Research Center, Ohio, 1998.

[Nod64] T. Noda, M. Inagaki, The structure of glassy carbon, *Bulletin of the Chemical Society of Japan* **37** (1964) 1534 – 538.

[Nod68] T. Noda, M. Inagaki, S. Yamada, A Comment on the Structure of Glassy Carbon, *Bulletin of the Chemical Society of Japan* **41** (1968) 3023 – 3024.

[Odu18] O.S. Odutemowo, J.B. Malherbe, L.C. Prinsloo, E.G. Njoroge, R. Erasmus, E. Wendler, A. Undisz, M. Rettenmayr, Structural and surface changes in glassy carbon due to strontium implantation and heat treatment, *Journal of Nuclear Materials* **498** (2018)

[Pau66] L. Pauling, The Structure and Properties of Graphite and Boron Nitride, PNAS, Vol. **56**, No. 6 (1966), 1646 – 1652.

[Pie93] H.O. Pierson, Handbook of carbon, graphite, diamond and fullerenes: properties, processing and applications, Noyes Publications, New Jersey 1993.

[Rob96] J. Robertson, Amorphous carbon, *Current Opinion in Solid State 6 Materials Science* **1** (1996) 557 – 561.

[www1] www.azom.com, Graphite (C): Classifications, Properties and Applications of Graphite, (accessed September 4, 2019).

[www2] www.azom.com, Diamond (C): Properties and Applications (accessed September 9, 2019).

[www3] www.htw-germany.com/technology (accessed September 13, 2019).

[Yam64] S. Yamada, A Review of Glasslike Carbons, 1964.

[Zha17] Z. Zhang, QiWang, The New Method of XRD Measurement of the Degree of Disorder for Anode Coke Material, *Journal of crystals* **7, 5** (2017) 1 – 10.

CHAPTER 3

ION IMPLANTATION

When energetic ions penetrate through material, they slow down by transferring their energy to the target atoms via elastic and inelastic collisions events and eventually stop at some depth within the target. The process whereby the projectile ions are incorporated into the target material is usually known as ion implantation. In addition to the fundamental nature of this process, is important to a wide variety of technologies. It can also be used to change the physical, chemical, or electrical properties of the solids, doping in semiconductor device fabrication and in metal finishing, as well as various applications in materials science research.

3.1 General concepts

In ion implantation, the ions accelerated by an electric field strike the target material and interact with the target atoms. When the ions pass through the target material they experience elastic collisions (nuclear) and inelastic collisions (electronic). These interactions may result in target atoms being temporarily or permanently displaced from their original lattice sites which causes the formation and accumulation of defects in the target [Gna99]. Formation and accumulation of defects within the lattice structure can lead to loss of long-range order of the atoms may eventually transform the crystalline structure into an amorphous state [Cal07].
Several models have been proposed based on the formation and accumulation of defects within the lattice structure, which lead to loss of long-range order of the atoms. Christel et al. [Chr81] proposed a more general model. According to this model, the critical dose decreases with increasing ion mass and is constant at sufficiently low temperatures. In addition, the crystal region exposed to irradiation spontaneously transforms into an amorphous state after reaching a sufficiently high (critical) concentration of radiation-induced defects. Although a large number of studies has investigated amorphisation, the mechanism of the transition to the amorphous state is still not clearly understood [Tet04].

Another model for the formation of amorphous by ion implantation at all implant temperatures was proposed by Morehead and Crowder [Mor70]. This creates a highly disordered, cylindrical region of many broken bonds and displaced atoms surrounding the ion track. It is then assumed

that if all of the target atoms in this region are displaced, the region becomes amorphous [Den73]. A continuous amorphous layer can be created when the cylindrical regions produced by various ions overlapped. This occurs when the critical dose, ϕ_c, measured in ions cm^{-2} has been implanted. This led Morehead and Crowder to the conclusion that at low temperatures.

$$\phi_C = \frac{EN}{(dE/dx)} \tag{3.1}$$

where *E* is the effective energy needed to displace a target atom (estimated to be 25 eV), *N* is the number of target atoms and (*dE/dx*) is the average energy loss per unit path length [Den73].

A modification of this basic model has been proposed by Gibbons [Gib72] in which it is assumed that amorphous material may be produced by the overlap of damaged, non-amorphous regions associated with individual damage clusters. This model is found to explain the dose dependence of damage and the approach to amorphicity in light ion cases where the model of Morehead and Crowder is inapplicable [Chr81].

3.2 Stopping power of ions in solids

When a solid target is bombarded by an energetic ion beam, the ion undergoes a series of collisions with the host atoms until it finally stops at some depth in the target. Stopping power by the target material is the factor which a measure of the ability of a material to slow down energetic ions that travel within the material. It also determines the final distribution of ions, defects and the damage produced by such ions. Since the ion loses its energy during penetration in the substrate, the energy loss (stopping) in a material is defined as (*dE/dx*) and can be written as:

$$S = -\frac{dE}{dx} \tag{3.2}$$

where *E* is the kinetic energy of the ion and *x* distance along the ion trajectory in the target, which measured from the surface of the target.

An energetic ion penetrating a material loses its energy via two processes which are considered to be independent of each other. Therefore, stopping power can be separated into nuclear stopping and electronic stopping [Fin05]. The total stopping power, *S*, of a target is defined as the energy loss (*dE*) per unit length (*dx*) of the incident ion. Hence, the total stopping power is given by the sum of the nuclear and electronic stopping which can be expressed as:

$$S = \left(\frac{dE}{dx}\right)_{nuclear} + \left(\frac{dE}{dx}\right)_{electronic} \tag{3.3}$$

The stopping cross section can be calculated by dividing S by the target density N, to yield:

$$\varepsilon = -\frac{1}{N}\frac{dE}{dx} \tag{3.4}$$

where ε is the stopping cross section.

Fig. 3.1 shows the effect of ion energy on the electronic and nuclear stopping powers by the target material. Both stopping powers increase with increasing energy of the bombarded ions until they reach a maximum value, and thereafter decrease. At low energies heavy ions (below the critical energy) the nuclear stopping is dominating. The elastic collision with the target atoms leads to the transfer of kinetic energy to the knock-on target atoms which might be displaced from their original positions. This might initiate structural defects such as vacancies and interstitials in the target material. At high energies (above the critical energy), there is a shift in the energy loss mechanism and electronic stopping begins to dominate. In this study, both 200 keV and 320 keV Xe^+ were implanted in glassy carbon at room temperature. The implantation energies used are much less than the critical energy ($E_{critical}$ = 1212 keV), thus, nuclear stopping power is expected to dominate during the implantation process [Zar15].

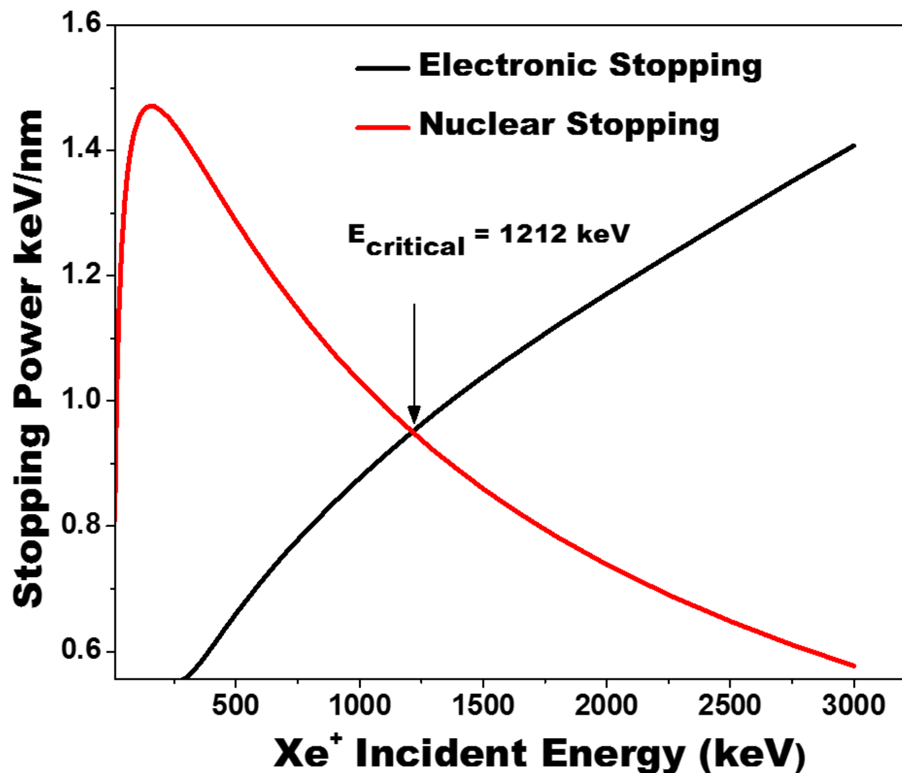

Fig. 3.1: Nuclear and electronic stopping powers of glassy carbon for Xe ions obtained from SRIM [Sri12]. The density of glassy carbon was taken as 1.42 g/cm^3.

3.2.1 Nuclear Stopping

Nuclear stopping occurs due to the energy transfer from the ion to the target nuclei. The interaction may be strong enough to displace the target atom from its lattice site. The energy lost by the incoming ion is transferred to the target atom, which can subsequently recoil away from its lattice site, thus causing lattice disorder and damaging the crystal structure.

Nuclear stopping can be explained theoretically based on a series of binary collisions between two charged particles and it can be well described by classical kinematics (see Fig. 3.2). The interaction between the incident ion and the target atom may be considered as isolated from the rest of the target atoms. This assumption enables us to treat the ion scattering and energy transfer as a simple two-body collision event. With this assumption, the maximum energy transfer (loss) by the incident ion will be equal to the total energy obtained in a head-on collision by the target atom. The energy loss (T) by the incident ion to the target atom is expressed as [Tow94].

$$T = \frac{4M_1M_2}{(M_1+M_2)^2} E_0 \sin^2\left(\frac{\theta}{2}\right) \tag{3.5}$$

where M_1 and M_2 are the atomic mass numbers of the ion and target atom respectively, θ is the scattering angle and E_o is the energy of the incident ion. T_{max}, is the maximum transferred energy which is given by $T_{max} = 4M_1M_2E/(M_1 + M_2)^2$, when ($\theta = \pi$), T_{max}, is in a head-on collision so,

$$T = T_{max} \sin^2\left(\frac{\theta}{2}\right) \tag{3.6}$$

The energy transfer from the ion to the target atoms can be considered as a binary elastic collision [Was07]. In order to describe the average energy transfer theoretically, we need to determine the probability of such a collision by the scattering cross-section reaction σ.

$$S_n(E) = N \int_0^{T_{max}} T d\sigma, \qquad d\sigma(T) = 2\pi b db \tag{3.7}$$

where b is the impact parameter, which is defined as the distance between the asymptotic trajectories of the colliding projectiles as shown in Fig. 3.2.

The projectile will transfer energy T which is a function of the collision event over all possible impact parameter b. The nuclear stopping is calculated by integrating with respect to the impact parameter:

$$S_n(E) = 2\pi \int_0^{b_{max}} T(E,\theta) b db \tag{3.8}$$

The biggest hurdle to determine the nuclear stopping power is how to calculate the repulsive interaction potential $V(r)$. Since the collision event is being treated as a binary collision with no external effects, it is safe to describe the particles as point masses which is acceptable considering the nucleus size. A simple approach is to treat the potential for interaction as simply the potential between the two nuclei, with the electrons serving only to screen the positive

nuclear charges from each other and thereby reducing the effective positive charges [Wer06]. At high energies ion implantation and small interatomic separations of the target atoms, r, $0 < r << a_o$ where the Bohr's radius, ($a_o = 0.53$ Å), $V(r)$ reduces to a repulsive coulomb interaction between the two nuclei. At intermediate energies separations, where the most relevant region for ion bombardment, there is a screening of the charges which makes this region very complicated to describe accurately [Bac12].

In ion implantation, when the distance between the two nuclei (the incident ion and the target atom) is typically in the order of a_o, the coulombic interatomic potential becomes invalid. This because of the limited range of interaction of the nuclei and hence no other nuclei will be involved. The effects of charge screening have been investigated and modelled by several researchers and they all agree that the Coulomb potential should be multiplied by a screening function $\Phi(r)$, such that the coulomb potential $V(r)$ then becomes:

$$V(r) = \frac{Z_1 Z_2 e^2}{4\pi\varepsilon_0 r}\Phi\left(\frac{r}{a}\right) \tag{3.9}$$

where a represents a screening length, which depends on the atomic numbers Z, and r/a is called the reduced radius. The reduced radius r/a makes the function $\Phi(r/a)$ in many classical interatomic potentials independent of Z_1 and Z_2, Z_1 and Z_2 are the atomic numbers of the ion and target respectively, e is the electron charge.

Successful attempts were made to fit the individual interatomic potentials. One of the most used screening functions for modeling atomic collisions is the one proposed by Ziegler, Littmark, and Biersack by using the Hartree-Fock equation and local density approximation [Zie85]. This approach allowed them to derive an expression for the so-called universal screening potential, Φ given below:

$$\phi(x) = 0.1818\, e^{-3.2x} + 0.5099\, e^{-0.9423x} + 0.2802\, e^{-0.4029} + 0.02817\, e^{-0.2016x} \tag{3.10}$$

where (x) the reduced radius defined as (r/a), based on the universal screening length, which is given as:

$$a = \frac{0.8854\, a_0}{Z_1^{0.23} + Z_2^{0.23}} \quad (3.11)$$

where a_o is the Bohr's radius given as 0.529 Å. This potential has been the basis for binary collision codes like (SRIM), which are frequently used to compute implantation profiles.

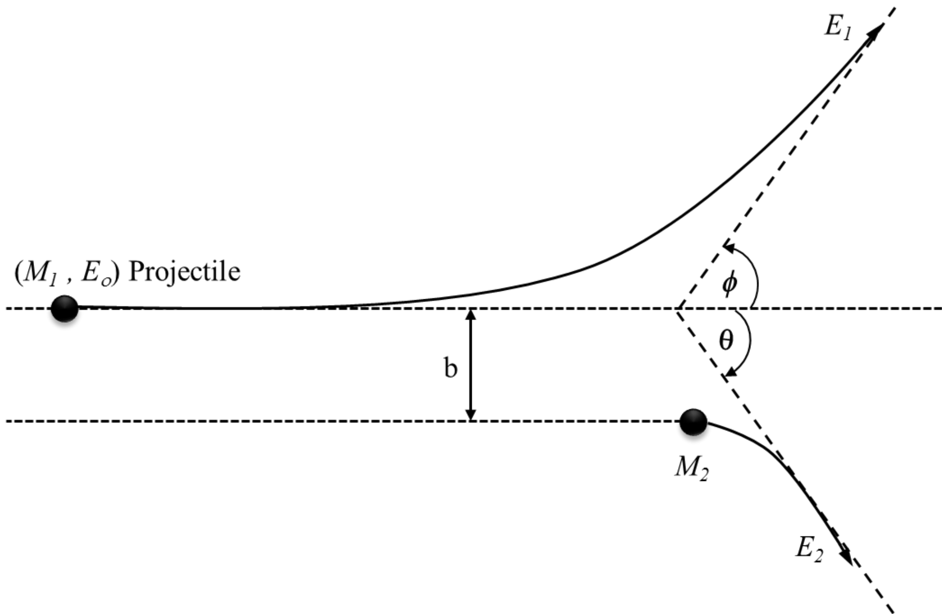

Fig. 3.2: Scattering of an energetic ion by a stationary atom in the laboratory.

3.2.2 Electronic Stopping

Electronic stopping is the interaction process between an energetic ion and the target electrons. The mechanism of transferring kinetic energy from the incident ions to the target electrons is complicated due to several processes. These processes include: direct kinetic energy transfer to target electrons, mainly due to electron-electron interactions, excitation or ionization of target atoms and excitation, ionization or electron capture of the incident ion [Tow94]. The electronic stopping has been described using different models for different ion energy regimes categorized as low, intermediate and high energies labeled I, II, and III in Fig.3.3. The basis of these models arises from comparing the ion velocity with the Bohr's velocity which is given as $v_o = ke^2/h$ where e and ħ are the electron charge and Planck's constant respectively.

The first region of the model (labeled I) is applicable to the low energy region, where the velocity of the ions, v is much slower than the target electrons such that $v < v_o Z^{2/3}$, where Z is the atomic number of the incident ion.

At 200 keV and 320 keV, a xenon ion has a velocity of 1.7×10^4 m/s and 6.8×10^5 m/s respectively. At these ion velocities,v is significantly lower than the Bohr velocity of the electrons ($v_o = 2.2\times10^6$ m/s) [Nas14]. Consequently, the incident ions cannot transfer sufficient energy to the electrons that have energy much lower than the Fermi level. Due to this, only electrons in the energy level close to the Fermi level contribute to the energy loss process. The electronic stopping for the low energy regime has been calculated by assuming a free electron gas with a density, ρ [Lin52]. The electronic stopping cross-section of an incident ion can be expressed as [Zie88]:

$$\varepsilon_e = \int I(v,\rho)\,(Z_1(v))^2 \rho dV \qquad (3.12)$$

where ε_e is the electronic stopping cross section, I is the stopping interaction of an ion of unit charge with velocity, v, and ρ the free electron gas density, Z_1 is the charge of the ion, and dV is a volume element of the target.

The second region of the model describes the intermediate energy (labeled II), a region where the incident ions velocity, $v \approx v_o Z^{2/3}$, and Z is the atomic number of the incident ion. In this region, the incident ion is partly ionized and the electronic stopping is maximized.

The third region (labeled III), the incident ions velocity, $v > v_o Z^{2/3}$, where Z is the atomic number of the incident ion.The incident ion with high velocity is fully stripped of all its electrons. This region is known as the Bethe-Bloch region, and the electronic stopping in this region is expressed as:

$$\varepsilon_e = \frac{4\pi Z_1^2 Z_2 e^2}{m_e v_1^2}\left[\ln\left(\frac{2m_e v_1^2}{I}\right) + \ln\left(\frac{1}{1-\beta^2}\right) - \frac{C}{Z_2}\right] \qquad (3.13)$$

where m_e is the electron's mass, v_1 the velocity of the ion, $\beta = v/c$ where c is the speed of light, Z_2 is the target atomic number, I is the average ionization potential and C/Z_2 is the shell

correction. I is theoretically defined as $\ln I = \sum_n f_n \ln E_n$, where E_n and f_n are the possible energy transitions and corresponding oscillator strengths for target atoms [Zie80] [Rim95]. The average ionization energy of the electrons of the target, is given by $I = I_o Z_2$ with $I_o = 10\ eV$.

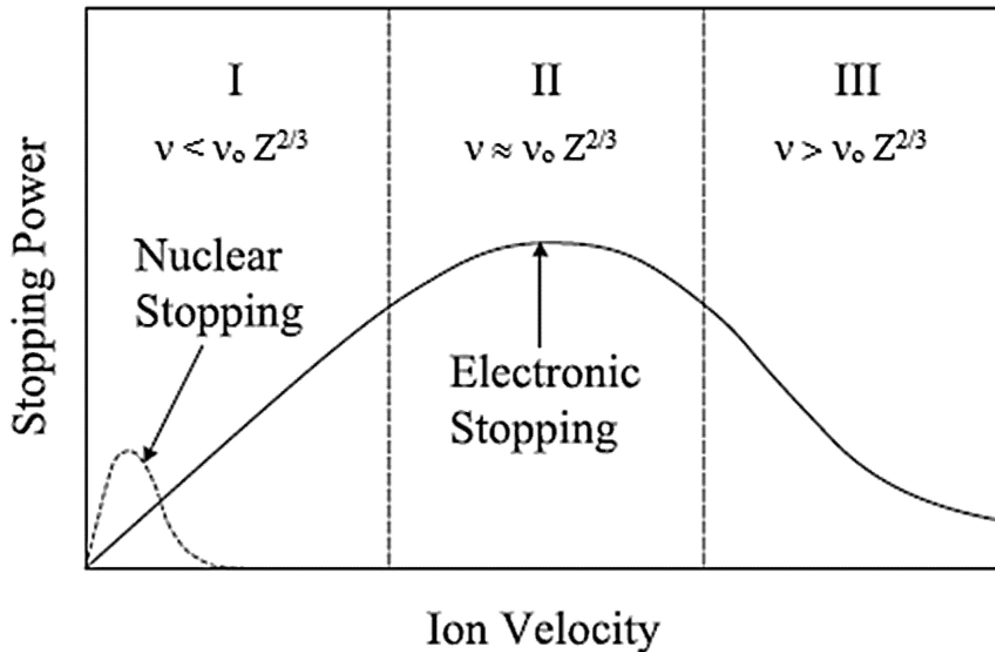

Fig. 3.3: Nuclear and electronic components of the ion stopping power as a function of ion velocity [Tri15].

In this study, xenon ions were implanted in glassy carbon at an energy of 200 keV and 320 keV which fall in the low energy regime. Rutherford backscattering spectrometry (RBS) analysis was carried out using helium particles with an energy of 1600 keV which is within the intermediate energy regime.

3.3 Energy Straggling

When energetic ions penetrate a target material, they lose energy due to many interactions with the atoms. This process often leads to statistical fluctuations, which implies identical ions with the same initial energy do not have the same energy after penetrating a certain thickness (x) of a homogeneous material [Chu78]. This phenomenon is known as energy straggling.

Several theories have been used to describe the straggling phenomenon, however, most of these theories are not accurate. The simplest theory is that derived by Bohr, where the energy straggling, Ω_B^2, is given as [May77].

$$\Omega_B^2 = 4\pi Z_1^2 Z_2 e^4 N \Delta R \qquad (3.14)$$

where Ω^2_B is Bohr's energy straggling, Z_1 and Z_2 are the projectile and target atomic numbers, respectively, N is the atomic density and ΔR is the thickness of the target. The full width at half maximum (FWHM) of the ion energy distribution, typically described by a Gaussian distribution in most cases, can be expressed as:

$$\text{FWHM} = 2\sqrt{2\ln 2}\,\Omega_B = 2.355\Omega_B \qquad (3.15)$$

The Bohr's theory predicts that the electronic energy straggling does not depend on the energy of the projectile and the value of the energy variation increases with the square root of the number of electrons per unit area $NZ_2\Delta x$ in the target [Nas14]. Furthermore, Bohr's theory was derived based on the assumption that [Bon71]:

(i) The target atoms are randomly distributed.

(ii) The velocity of the projectile is high as compared to the orbital velocities of the target electrons.

(iii) The energy of the projectile is changed only slightly during penetration.

Lindhard and Scharff [Lin62] [Lin68] [Lin96], Bonderup and Hvelplund [Bon71] have modified Bohr's theory of straggling. They have extended this theory to include corrections for energies where the assumptions may not be valid particularly at low and medium energies.

3.4 Range of ion implanted

The average distance travelled by an ion before finally coming to rest in a target material is known as the range of the ion. The mean total range of the ions can be calculated by integrating the energy loss.

$$R = \frac{1}{N}\int_0^{E_0} \frac{dE}{S} \Rightarrow \frac{1}{N}\int_0^{E_0} \frac{dE}{(dE/dx)_n + (dE/dx)_e} \quad (3.16)$$

where N is the atomic density of the target, *dE/dx* is the rate of energy loss of the ion as it travels through a target.

The average depth of implanted ions with respect to the surface is known as the mean projected range (R_P). Due to scattering of the ions in their interactions with the target atoms, projected range (R_P) is smaller than the mean total range, *R* as shown in figure 3.4. The relation between R and R_P is expressed approximately as

$$R_P \approx \frac{R}{1 + \frac{m_2}{3m_1}} \quad (3.17)$$

where m_1 and m_2 are the masses of incident ion and target atoms respectively.

Furthermore, as a result of multiple collisions, the ions will deviate from their original direction and there will be a lateral spreading of the ion beam in the target. This spread in ion range caused by the fluctuations in energy loss mechanism is known as range straggling (ΔR_P) [Goo12] [Tow94]. Some of the ions stop at a depth less than R_P and some others at a depth greater than R_P. Therefore, range straggling (standard deviation of the range) is usually used to find the distribution around R_P. Due to the range straggling effect, the implanted profile as a function of depth is approximately Gaussian in form. The concentration of implanted ions at low energy, a fluence (φ) and the depth (x) in a target with atomic density N are related to R_P and ΔR_P and is given as [Bau11] [Nas06]:

$$C(x) = \left(\frac{\varphi}{\sqrt{2\pi}\,\Delta R_P}\right) \exp\left(\frac{-(x - R_P)^2}{2\pi\Delta R_P^2}\right) \quad (3.18)$$

The term $\varphi/\sqrt{2\pi\Delta R_P}$ represents the peak concentration of implanted ions, $\varphi/\sqrt{2\pi\Delta R_P} \approx 0.4\varphi/\sqrt{\Delta R_P}$.

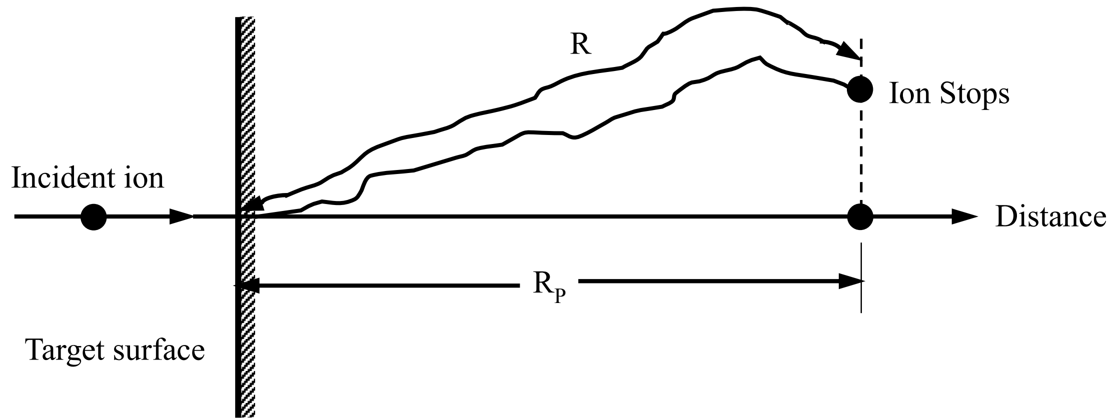

Fig. 3.4: The projected range R_P and the total range R for incident ion in target material.

Experimental profiles often show deviations from a symmetrical Gaussian distribution. Therefore, the two parameters R_P and ΔR_P are not enough to describe the depth distribution and more moments are needed [Rim95]. The next two moments in a general implantation profile are skewness and kurtosis. Skewness (γ) is a measure of how much the implantation profiles is tilted away from the projected range, R_P. The skewness of a profile can either be positive or negative according to the direction of tendency. Kurtosis (β) is described as the contribution ion distribution profile tail over the flatness of the implanted profile shape. For a perfect Gaussian profile, γ = 0 and β = 3.

$$\gamma = \frac{\sum_{i=1}^{n}(x_i - R_P)^3}{N\sigma^3} \tag{3.19}$$

$$\beta = \frac{\sum_{i=1}^{n}(x_i - R_P)^4}{N\sigma^4} \tag{3.20}$$

where $\boldsymbol{\sigma}$ is the standard deviation (i.e. range straggle, ΔR_P) and N is the total number of implanted ions.

Fig. 3.5 shows the as-implanted profile of xenon that was fitted to an Edgeworth distribution using the Genplot program [www1]. The Edgeworth distribution is expressed as:

$$N(x) = Af(x)\exp\left(-\frac{(x - R_P)^2}{2\Delta R_P^2}\right) \tag{3.21}$$

$$f(x) = 1 + \frac{\gamma}{6}\left[\left(\frac{x - R_P}{\Delta R_P}\right)^3 - 3\left(\frac{x - R_P}{\Delta R_P}\right)\right] + \frac{\beta - 3}{24}\left[\left(\frac{x - R_P}{\Delta R_P}\right)^4 - 6\left(\frac{x - R_P}{\Delta R_P}\right)^2 + 3\right]$$

(3.22)

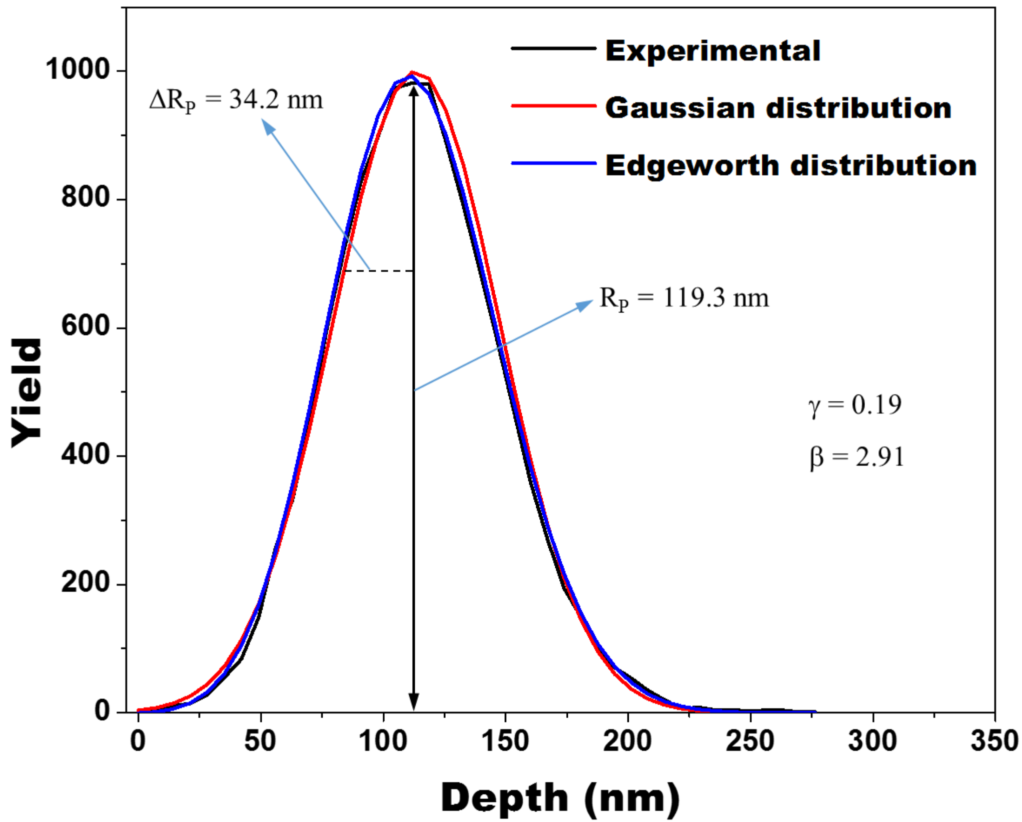

Fig. 3.5: 200 keV xenon ions implanted in glassy carbon as a function of implantation depth. The first four moments of the implanted ion distributions are the projected range (R_p), the straggling (ΔR_p), the skewness (γ) and the kurtosis (β). Their values were obtained by fitting the as-implanted Xe depth profile to an Edgeworth distribution.

As can be seen from the figure, within the resolution on the line thicknesses, these three curves agree with each other. This means that our as-implanted Xe has a Gaussian form. As will be discussed in the next chapter, this will be a crucial point to allow the determination of the diffusion coefficient from our Rutherford Backscattering Spectrometry (RBS) depth profiles.

3.5 Simulation of xenon ion implanted in glassy carbon

In order to gain an idea of the ion implantation details before performing the experiment, it is important to start with a simulation. In this study, the Stopping and Ranges of Ions in Matter (SRIM) program was used to calculate various parameters and moments such as projected range R_p, projected range straggling ΔR_p, the skewness (γ) and the kurtosis (β) related to ion implantation [Sri12]. The SRIM program contains different programs within it and one of these is the transport of ions in matter TRIM program. The TRIM program was used to simulate and predict the effect of xenon ion implantation on glassy carbon. The values obtained were compared with the experimental depth profiles obtained from Rutherford Backscattering spectrometry (RBS) results.

The SRIM program uses a Monte-Carlo computer simulation method and a binary collision algorithm to estimate the trajectory of implanted species due to the statistical nature of the paths of the implanted samples (see figure 3.6). The TRIM (sub-routine of SRIM) program is a highly efficient computer program with an excellent degree of accuracy of about 5 – 10 % error. This efficiency of TRIM is achieved by the fact that it does not take into account other parameters which can case deviations when compared to the real data after implantation such as crystal structure and the dynamic composition. The changes in the material that occurs when the incident ion penetrates the target material. Some of the assumptions made by TRIM include:

- The SRIM program does not take the crystallinity of the target into consideration i.e. it assumes that the target is amorphous, hence crystal orientation effects are ignored.
- The thermal effects in the solid i.e. redistribution of the implanted ions by thermal or vacancy are neglected.
- The recombination of interstitials with vacancies is neglected.
- The predictions of the projected range are based on binary collisions alone (the influence of neighboring atoms is neglected).
- The electronic and nuclear stopping powers are an averaging fit to a large number of experimental data points.

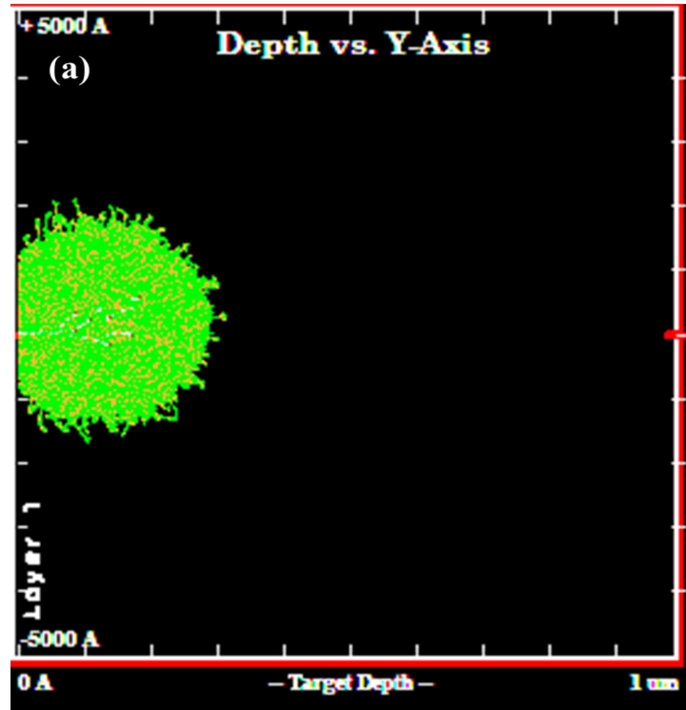
+5000 A
Depth vs. Y-Axis
(a)
Layer 1
-5000 A
0 A
– Target Depth –
1 um

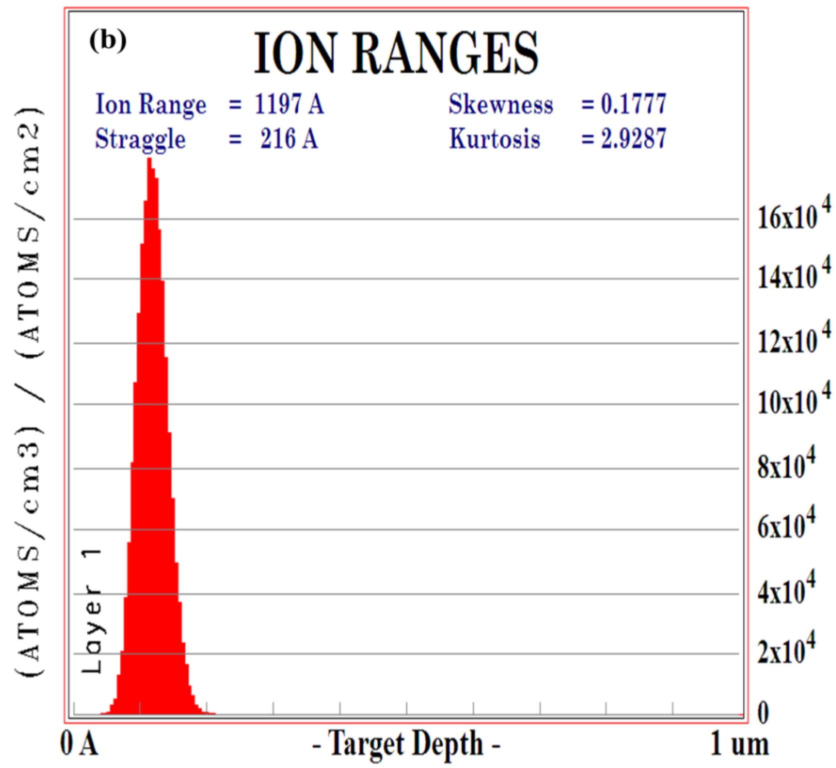
(b)
ION RANGES
Ion Range = 1197 A
Straggle = 216 A
Skewness = 0.1777
Kurtosis = 2.9287
(ATOMS/cm3) / (ATOMS/cm2)
Layer 1
16x10^4
14x10^4
12x10^4
10x10^4
8x10^4
6x10^4
4x10^4
2x10^4
0
0 A
- Target Depth -
1 um

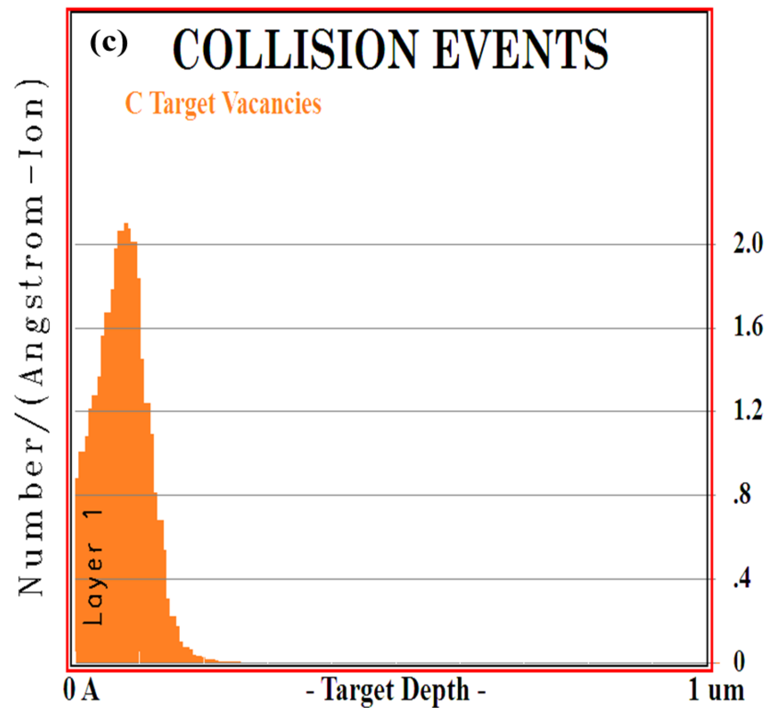

Fig. 3.6: TRIM [Sri12] simulation showing the: (a) trajectories of 200 keV xenon ions implanted in glassy carbon (b) the implanted Xe ion distribution and (c) the vacancy distribution.

3.6 Amorphisation

During ion implantation at low temperatures such as room temperature (RT) and low energies, each ion produces a region of disorder around the ion track. During implantation, the energy deposition associated with ion bombardment creates damage in the crystal lattice. Depending on the mass and the fluence of the implanted ion (e.g. Xe) the initial displacements lead to more extended disorder or full amorphisation. At the low energies (< 400 keV), it can readily induce amorphisation of the target substrate. As the implantation fluence increases, the disorder increases which leads to more atoms being displaced producing an amorphous layer.
Amorphisation is easily achieved in the case of glassy carbon with its predominantly covalent bonds (e.g. carbon). Glassy carbon is a graphitic material with the structure of a long-range disorder coexistence with the ordering of the six-hold aromatic rings arranged within nanosized graphite [Lav08]. Ion implantation amorphised glassy carbon has been studied by several authors [Iwa00] [Toi01] [Odu18] and the general agreement is that the density of glassy carbon increases from (1.4 – 1.5) g/cm3 to about 2.25 g/cm^3 (amorphous carbon) after high fluence

ion bombardment. The change in the density of glassy carbon due to ion bombardment results in the improvement of the wear resistance, hence, the wear resistance of glassy carbon could be improved by the ion implantation process. These properties also can make it as an alternative material for nuclear waste storage. It has been proposed as a containment material for high-level nuclear waste produced from nuclear power plants [Mal18]. Reports also concluded that glassy carbon will be a successful container which can retain nuclear wastes even in harsh condition.

3.7 Annealing of the radiation damage

The implanted ions may come to rest on a vacant lattice position (fill a vacancy) or occupy a non-lattice position (become an interstitial). These types of defects are known as point defects. Other point defects that may exist after ion implantation and annealing are substitutional atoms (foreign atoms which sit on a host lattice site) and interstitial atoms (either self-interstitials or foreign interstitials).To repair the defects created during ion implantation, annealing is used.
Annealing is the process of heating the crystal to reduced/ remove the amount of damage by adding energy into the system so that the defects become mobile [Hic07]. Upon annealing at moderate temperatures, point defects can interact to form extended defects. Extended annealing time or annealing at higher temperatures will result in the defects evolving so much that the atoms find lower-energy sites to occupy in the lattice and, thereby restoring the crystal structure [Gib72]. Figure 3.7 shows the effect of crystal structure before and after annealing. In this study, we investigated the influence of low and high-temperature annealing on the structure of glassy carbon after bombarded with Xe ions. The annealing behaviour of amorphous glassy carbon produced by room temperature ion implantation depends on the structure of the glassy carbon (discussed in detail in chapter 2).

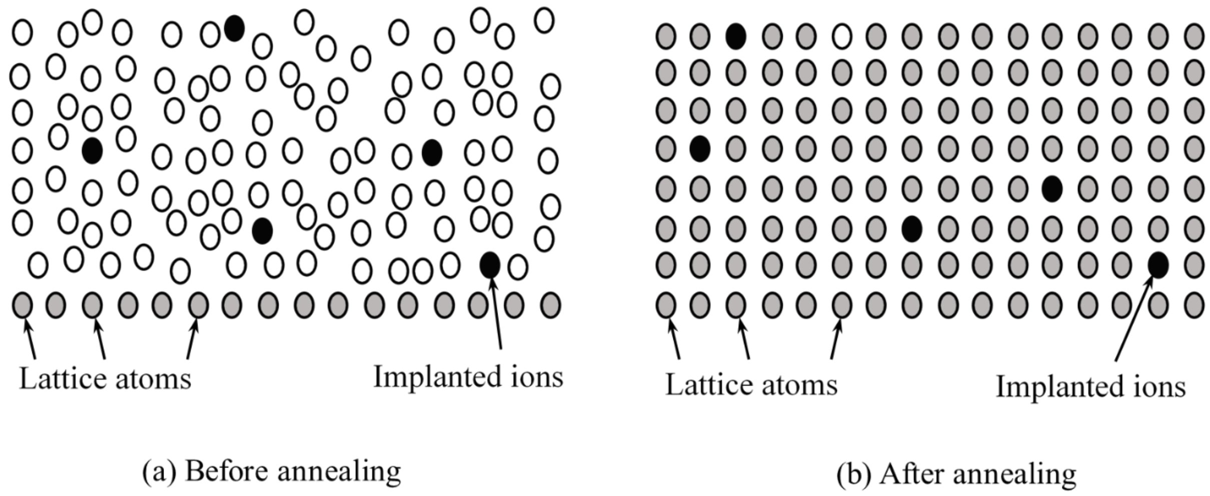

Fig. 3.7: (a) Crystal damage and (b) annealed the damage.

References

[Bac12] M. Backman, Effects of nuclear and electronic stopping power on ion irradiation of silicon based compounds, Helsinki, Finland, 2012.

[Bau11] Annie Baudrant, Silicon Technologies: ion implantation and thermal treatment, John Wiley & Sons, Inc., USA, 2011.

[Bon71] E. Bonderup, P. Hvelplund, Stopping power and energy straggling for swift protons, *Physical Review A* **4** (1971) 562 – 569.

[Buk14] S.S. Bukalov, L.A. Leites, A. Sorokin, A.S. Kotosonov, Structural changes in industrial glassy carbon as a function of heat treatment temperature according to Rama spectroscopy and X-ray, *Nanosystems: Physics, Chemistry, Mathematics* **5** (2014) 186 – 191.

[Cal07] W.D. Callister, Jr., Materials science and engineering: an introduction, 7th ed., John Wiley & Sons, Inc., New York, 2007.

[Chr81] L. A. Christel, J. F. Gibbons, T. W. Sigmon, Displacement criterion for amorphization of silicon during ion implantation, *Journal of Applied Physics* **52** (1981) 7143 – 7146.

[Chu78] W.K. Chu, J.W. Mayer, M. A. Nicolet, Backscattering spectroscopy, Academic Press, New York, 1978.

[Den73] J. R. Dennis, E. B. Hale, Model Correction for the Formation of Amorphous Silicon by Ion Implantation, *Radiation Effects* **19** (1973) 67 – 68.

[Gib72] J. F. Gibbons, Proc. IEEE 60, 1062 (1972).

[Gna99] H. Gnaser, Low-Energy Ion Irradiation of Solid Surfaces, Springer, Germany, 1999.

[Goo12] M. Goorsky, Ion Implantation, InTech, Croatia, 2012.

[Har04] P. J. F. Harris, Fullerene-related structure of commercial glassy carbons, *Philosophical Magazine* **84** (2004) 3159 – 3167.

[Hic07] D. P. Hickey, Ion implantation induced defect formation and amorphisation in the Group IV semiconductors: Diamond, silicon and germanium, Available at: http://etd.fcla.edu, 2007.

[Iwa00] M. Iwaki and K. I. Terashima, Change in atomic density of glassy carbon by Na ion implantation, *Surface and Coatings Technology* **128-129** (2000) 429 – 433.

[Lav08] V. Lavrentiev, J. Vacik, and H. Naramoto, Structural phenomena in glassy carbon induced by cobalt ion implantation, *Applied Physics A* **92** (2008) 673 – 680.

[Lin62] J. Lindhard and V. Nielsen, Nuclear collisions and ionisation fluctuations in charged particle detectors, *Physics Letters* **2** (1962) 209 – 211.

[Lin68] J. Lindhard, V. Nielsen, M. Scharff, Approximation method in classical scattering by screened coulomb fields., Kgl. Dan. Vidensk. Selsk., *Matematisk-fysiske Meddelelser* **36, 10** 1968.

[Lin96] J. Lindhard, H. Allan, Relativistic theory of stopping for heavy ions, *Physical Review A* **53** (1996) 2443 – 2455.

[Mal18] Johan B. Malherbe, O.S. Odutemowo, E.G. Njoroge, D.F. Langa, T.T. Hlatshwayo, C.C. Theron, Ion bombardment of glassy carbon, Vacuum **149** (2018) 19 – 22.

[May77] J.W. Mayer, E. Rimini, Ion beam handbook for material analysis, Academic Press, New York, 1977.

[Mor70] F. F. Morehead, Jr., B. L. Crowder, A model for the formation of amorphous Si by ion bombardment, *Radiation Effects* **6** (1970) 27 – 32.

[Nas06] M. Nastasi, J. Mayer, and Y. Wang, Ion Implantation and Synthesis of Materials, Springer Science & Business Media, 2006.

[Nas14] M. Nastasi, J. Mayer, and Y. Wang, Ion Beam Analysis, Fundamentals and Applications, CRC Press, London 2014.

[Odu18] O.S. Odutemowo, J.B. Malherbe, L.C. Prinsloo, E.G. Njoroge, R. Erasmus, E. Wendler, A. Undisz, M. Rettenmayr, Structural and surface changes in glassy carbon due to strontium implantation and heat treatment, *Journal of Nuclear Materials* **498** (2018) 103 – 116.

[Pie93] H.O. Pierson, Handbook of carbon, graphite, diamond and fullerenes, Noyes publications, New Jersey, 1993.

[Rim95] E. Rimini, Ion Implantation: Basics to Device Fabrication, Kluwer Academic Publisher 1995.

[Rys86] H. Ryssel, H. Glawischnig, Ion Implantation Techniques, Berchtesgaden, Fed. Rep. of Germany, 1982.

[Sri12] J. Ziegler, SRIM 2012 computer code, (2012). www.srim.org.

[Tet04] D. I. Tetelbaum, Yu. A. Mendeleva, A Mechanical Model of Amorphization

under Ion Bombardment, *Physics of the Solid State* **46** (2004) 2026 – 2029.

[Tow94] P.D. Townsend, P.J. Chandler, L. Zhang, Optical effects of ion implantation, Cambridge University Press, New York, 1994.

[Tri15] S. K. Tripathi, J. Kaur, R. Ridhi, K. Sharma, and R. Kaur, Radiation Induced Effects on Properties of Semiconducting Nanomaterials, Solid State Phenom., **239** (2015) 1 – 36.

[www1] http://www.genplot.com, accessed November 05, 2016.

[Zar15] E. Zarkadoula, M. Toulemonde, and W. J. Weber, Additive effects of electronic and nuclear energy losses in irradiation-induced amorphization of zircon, *Applied Physics Letters* **107** 261902 (2015) 1 – 5.

[Zie80] J. F. Ziegler, Stopping cross-sections for energetic ions in all elements, Vol. 5, Pergamon Press, New York 1980.

[Zie84] J. F. Ziegler, Ion Implantation Science and Technology, Academic Press, New York, 1984.

[Zie85] J.F. Ziegler, J.P. Biersack, The stopping and range of ions in matter, Treatise on Heavy-Ion Science, Springer, US, (1985) 93 – 129.

[Zie88] J.F. Ziegler, Ion Implantation Science and Technology, 2nd ed., Academic Press, New York, 1988.

CHAPTER 4

DIFFUSION IN SOLIDS

Diffusion is the transport of matter from a region of high concentration to a low concentration region, as a result of random motion of the atoms or molecules. The factors that influence diffusion are temperature (thermal energy), diffusing species, concentration gradient, and microstructure of the material. The diffusion process is also responsible for the chemical reactions and microstructural changes in solids.

4.1 Mechanisms of diffusion in solids

There are two major mechanisms of diffusion in solids namely: volume diffusion, dislocation and grain boundary diffusion. These mechanisms of diffusion depend significantly on the crystal structure and temperature. When the temperature increase, the average kinetic energy will increase which lead to the atoms oscillating faster until they break loose from the molecular bond. These oscillations will become large enough to allow an atom to change sites, by moving from its lattice site to another position in the crystal, which give rise to diffusion in solids.

4.1.1 Volume Diffusion

Volume diffusion (or lattice diffusion) is a mechanism of diffusion that occurs within a crystal lattice due to the movement of point defects. The way in which volume diffusion takes place depends largely on the type of point defect given below:

- Vacancy (substitutional)
- Interstitial (direct interstitial)
- Interstitialcy (self-interstitial) diffusion

4.1.1.1 Vacancy mechanism

All crystals have vacancies, some of the lattice sites are unoccupied by atoms, and that play an important role in all processes related to impurity diffusion. If one of the atoms on an adjacent

site jumps into the vacancy, the atom is said to have been diffused by the vacancy mechanism. In order for the atom to be able to jump from one lattice site to another, the atoms will need to have enough energy to overcome the bond and move to a vacant. This because the atoms that close to the vacant site are bonded to fewer atoms as a result of the displacement of one of the lattice atom. Therefore, during this process, the direction of flow of atoms is opposite the vacancy flow direction, as depicted in Figure 4.1.

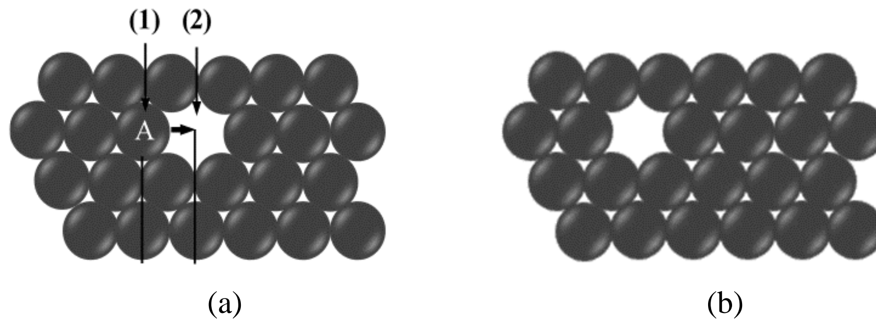

Fig. 4.1: A schematic illustration of the vacancy diffusion mechanism: (a) and (b) are the positions of the atom before and after diffusion respectively. The atom **A** moves from (1) to (2) while the vacancy moves from (2) to (1).

4.1.1.2 Interstitial mechanism

Impurity atoms in a solid (e.g. hydrogen, carbon, nitrogen, and oxygen) which are considerably smaller than the host atoms (lattice atoms) are usually incorporated in interstitial sites of the solid. Therefore, an atom is said to diffusing by an interstitial mechanism (known as a direct interstitial) when it jumps from one interstitial site to its nearest neighbour interstitial site without permanently displacing any of the matrix atoms [She89] [Hei05]. Furthermore, interstitial diffusion is generally faster than vacancy diffusion, because there are many more interstitial sites than vacancy sites to jump to. This requires small impurity atoms (e.g. C, H, O) to fit into interstices in the host, as depicted in Figure 4.2.

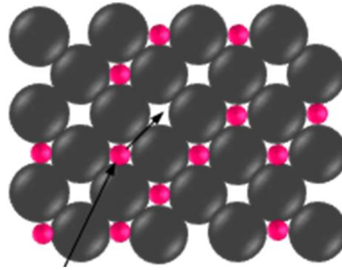

Fig. 4.2: Interstitial mechanism of diffusion

4.1.1.2 Interstitialcy mechanism

In this case, self-interstitials extra atoms located between lattice sites push neighbour atoms into an interstitial position (Fig 4.3). This allows the atoms to occupy the lattice site already occupied by the displaced neighbour atom. Self-interstitials are usually the same size as the atoms located in the lattice sites which gives less distortion [Meh07].

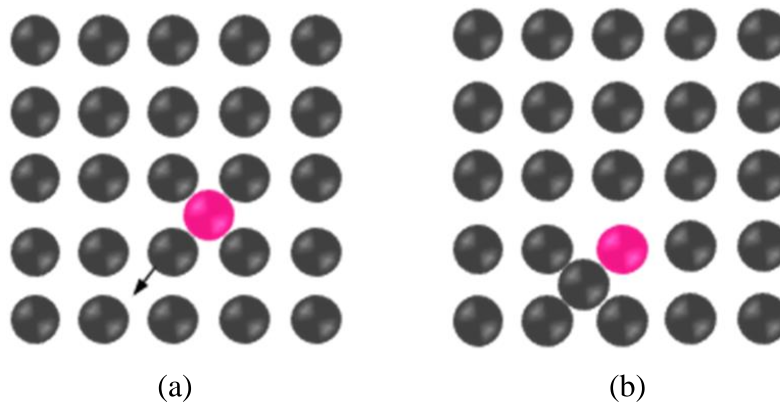

Fig. 4.3: Interstitialcy mechanism of diffusion: (a) and (b) are the positions of self-interstitial before and after diffusion respectively.

4.1.2 Dislocations and grain boundaries mechanism

The mechanisms of diffusion in crystalline materials are closely associated with defects. Point defects such as vacancies or interstitials are the simplest defects and often mediate diffusion. The other types of defects in crystalline solid material are dislocation and grain

boundary diffusion. These can act as diffusion short circuits because the mobility of atoms along such defects is usually much higher than in the lattice [Hei05] [Pau14]. This type of diffusion can have a strong impact on the process of interdiffusion, especially since the diffusion rates of atoms are enhanced along with these defects.

Most crystalline solids i.e. metals and alloys are found in polycrystalline form, which is made of multiple grains separated from each other by boundaries along which atomic configurations are highly distorted [Was07]. At low temperatures, the vacancy mobility will be low, the grain boundary and dislocation diffusion mechanisms dominate the lattice diffusion due to a high level of disorder along the boundaries. While at high temperatures, most of the disorders along the grain boundaries have been annealed out due to thermal energy. In this case, lattice diffusion dominates. Furthermore, grain boundary and dislocation make the diffusion in polycrystalline solids quite a complicated phenomenon because it is difficult to differentiate them from volume diffusion [Gup05]. This is because atoms diffusing through grain boundaries and dislocations may eventually leave and continue to diffuse in the lattice regions adjacent to the grain boundary which will eventually give rise to a volume diffusion field around the grain boundary.

4.2 Mathematics of Diffusion

4.2.1 Fick's first law

Fick's first law (also known as steady state diffusion) only applies if the concentration does not change with time (*t*) along with i.e. dC/dt = 0 and dC/dx = constant [Gup05]. The flux of the diffusing particles for one-dimensional diffusion (*x*-direction) is illustrated in figure 4.4. The particles can be atoms, molecules, or ions. Fick's first law for an isotropic medium can be written as [Meh07]:

$$J_x = -D\left(\frac{\partial C}{\partial x}\right) \quad (4.1)$$

where *J* is the flux, *C* is concentration, *D* is the diffusion coefficient and *x* is the distance of atomic migration. The minus sign is due to the opposite directions of the atomic flux and the concentration gradient. The unit of diffusion flux is determined as the number of particles (or

moles) travelling perpendicular to a unit area per unit time and concentration is the number of particles per unit volume. Therefore, the unit of diffusivity is given as length per unit time (typical units are m^2/s). Equation (4.1) states that the diffusion flux tends towards zero as the sample becomes homogenous. In three dimensions the Fick's first law is generalized as below [Meh07]:

$$J_x = -D\nabla C \qquad (4.2)$$

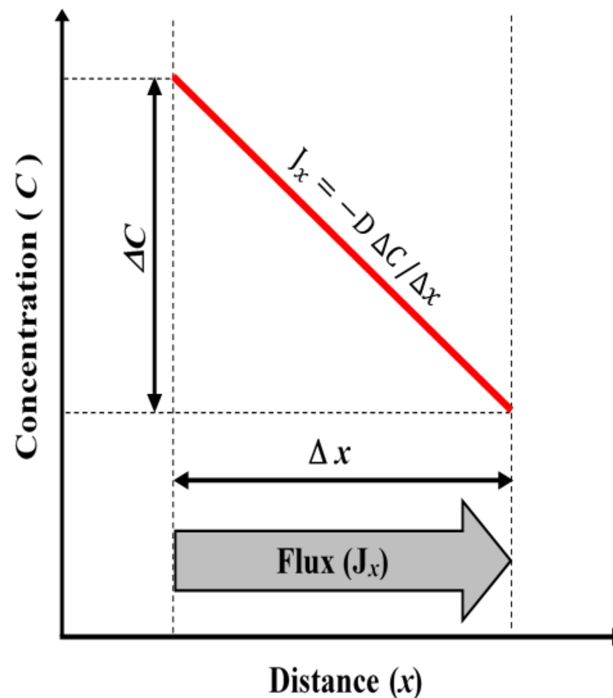

Fig. 4.4: Illustration of Fick's first law, the concentration C is a function of the distance *x*.

4.2.2 Fick's second law

In most real diffusion situations the concentration profile and the concentration gradient change with time. These changes can be described as non-steady state diffusion (Fick's second law), which is derived from equation (4.1). Consider a bar with a uniform cross-sectional area, A, and a small volume of length dx as shown in the Figure 4.5. If J_1 and J_2 are the fluxes of the impurity entering and exiting the volume element [Cam01], then

$$\frac{\partial J}{\partial x} = \frac{J_2 - J_1}{dx} \qquad (4.3)$$

If J_1 and J_2 are not the same, the concentration of the diffusing element in the volume must change. Since the number of impurities in the volume element is the product of the concentration and differential volume element (A.d*x*), then the continuity equation can be written as:

$$Adx\frac{\partial C}{\partial t} = -A(J_2 - J_1) = -Adx\frac{\partial J}{\partial x} \qquad (4.4)$$

or

$$\frac{\partial C(x,t)}{\partial t} = -\frac{\partial J}{\partial x} \qquad (4.5)$$

From equation (4.1) this can be written:

$$\frac{\partial C(x,t)}{\partial t} = \frac{\partial}{\partial x}\left(D\frac{\partial C}{\partial x}\right) \qquad (4.6)$$

Equation 4.5 yields the general form of Fick's second law. If the diffusion coefficient is assumed to be independent of position, then question (4.5) is reduced to:

$$\frac{\partial C(x,t)}{\partial t} = D\frac{\partial^2 C(x,t)}{\partial x^2} \qquad (4.7)$$

Then, in three dimensions for an isotropic medium, Fick's second law can be expressed as

$$\frac{\partial C}{\partial t} = D\nabla^2 C \qquad (4.8)$$

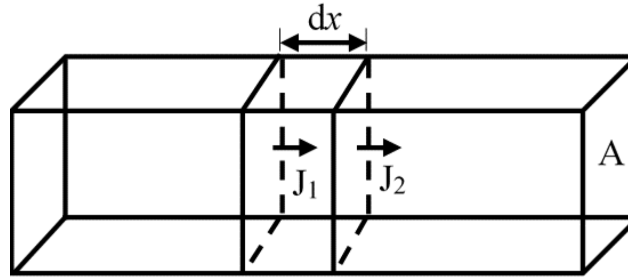

Fig. 4.5: A differential volume element in a bar of cross-sectional area A. J_1 and J_2 are the flux of the impurity entering and exiting the volume element respectively. Redrawn from [Cam01].

In a limited temperature range the temperature dependence of diffusion coefficient (*D*), is given by an Arrhenius equation [Sha73].

$$D = D_0 \exp\left(-\frac{E_a}{k_B T}\right) \tag{4.9}$$

where E_a is the activation energy, k_B is the Boltzmann constant, D_o is a temperature independent pre-exponential factor and *T* is the temperature in Kelvin.

4.3 Estimating the diffusion coefficient

Several methods have been used to obtain the general solutions of the diffusion equation for a variety of initial and boundary conditions provided the diffusion coefficient is constant [Cra75]. To solve the diffusion coefficient *D* for the Fickian diffusion, Malherbe et al. [Mal17] derived a solution to the Fick diffusion in equation (4.7). For an isotropic material implanted with a mono energetic impurity atoms (such as in this study) the initial implanted profile is assumed to be Gaussian with projected range (R_p) and range straggling (ΔR_p) and is given by:

$$C(\xi, 0) = A_0 \exp\left[\frac{\left(\xi - R_p\right)^2}{2\Delta R_p^2}\right] \tag{4.10}$$

where ξ is the depth below the surface. The solution for the diffusion of the implanted profile with annealing time is given by:

$$C(x,t) =$$

$$\frac{A_0 \, . \, \Delta R_p}{2\sqrt{2Dt + \Delta R_p^2}} e^{\left(-\frac{(x-R_p)^2}{4Dt+2\Delta R_p^2}\right)} \left[1 + erf\left(\frac{2DtR_p + x\Delta R_p^2}{\Delta R_p \sqrt{2(2\mathrm{Dt})^2 + 4Dt\Delta R_p^2}} \right) - ke^{\left(-\frac{xR_p}{Dt+\Delta R_p^2/2}\right)} \left\{ 1 + erf\left(\frac{2DtR_p - x\Delta R_p^2}{\Delta R_p \sqrt{2(2\mathrm{Dt})^2 + 4Dt\Delta R_p^2}} \right) \right\} \right] \quad (4.11)$$

and

$$k = 1 - \left[\frac{2C_0}{A_0} \frac{\sqrt{2Dt + \Delta R_p^2}}{\Delta R_p} \exp\left(\frac{R_p^2}{4Dt + 2\Delta R_p^2} \right) \Big/ \left\{ 1 + erf\left(\frac{R_p\sqrt{Dt}}{\Delta R_p \sqrt{2Dt + \Delta R_p^2}} \right) \right\} \right] \quad (4.12)$$

In the following diffusion, profiles are considered for the two limiting cases for the parameter k, k = 1 and k = -1. k = 1 represents the case of a perfect sink at the surface of the substrate while, k = -1 represents the case of a perfect reflecting surface. In our calculations, k was a fitting variable. A MATLAB program was written in-house in 2016, and updated with the new version (April 2018) [Mal17]. In order to fit the experimental data such as RBS data and to extract the diffusion coefficients at the different annealing temperatures and time duration, the diffusion has to be Fickian. However, the present version is more general and fits also data with a non-zero on the surface of the sample.

.

References

[Cal10] W. D. Callister, Jr, D. G. Rethwisch, Materials Science and Engineering: An Introduction, 8th ed., John Wiley& Sons, Inc., USA, 2010.

[Cam01] S.A. Campbell, The Science and Engineering of Microelectronic Fabrication, 2nd ed., Oxford University Press, New York, 2001.

[Cra75] J. Crank, The Mathematics of Diffusion, 2nd ed., Oxford University Press, Bristol, 1975.

[Gup05] D. Gupta, Diffusion processes in advanced technological materials, William Andrew, New York, 2005.

[Hei05] A P. Heitjans, J. Kärger, Diffusion in condensed matter, Springer, Berlin, 2005.

[Kau95] I. Kaur, Y. Mishin and W. Gust, Fundamentals of grain boundary and interphase boundary diffusion, 3rd ed., John Wiley & Sons, Inc., New York, 1995.

[Mal17] J.B. Malherbe, P.A. Selyshchev, O.S. Odutemowo, C.C. Theron, E.G. Njoroge, D.F. Langa, T.T. Hlatshwayo, Diffusion of a mono-energetic implanted species with a Gaussian profile, *Nuclear Instruments and Methods in Physics Research* **406** (2017) 708 – 713.

[Meh07] H. Mehrer, Diffusion in Solids, Springer, Berlin, 2007.

[Pau14] A. Paul, T. Laurila, V. Vuorinen and S. V. Divinski, Thermodynamics, Diffusion and the Kirkendall Effect in Solids, Springer International Publishing, Switzerland, 2014.

[Sha73] D. Shaw, Atomic Diffusion in Semiconductors, Plenum Press, London and New York, 1973.

[She89] P. Shewmon, Diffusion in Solids, 2nd ed., Ohio State University, USA, 1989.

[Was07] G. Was, Fundamentals of radiation material science, Metals and Alloys, Springer, Berlin, 2007.

CHAPTER 5

ANALYTICAL TECHNIQUES

5.1 Rutherford Backscattering Spectrometry

Rutherford backscattering spectrometry (RBS) is a technique where a beam of monoenergetic charged particles usually He^{+} or H^{+} ions, is incident and penetrates the target material with energy in the MeV range (1.4 and 1.6 MeV respectively in this study). Consequently, a small fraction of the ions are scattered back from the target at a certain angle i.e. 165 ^{o}. In a solid, where the ions penetrate the solid they are progressively slowed down and eventually stopped. However, a certain portion of the ions will undergo close collisions with target atoms resulting in large changes in energy transfers and direction. But a fewer of the incident projectiles ($<10^{-4}$) are scattered back and leave the target [Grob84]. The charged particles are generated and accelerated in a Van de Graaff accelerator.

5.1.1 The Van de Graaff accelerator

An illustration of the RBS set-up at the University of Pretoria is shown in Figure 5.1. The major components of this backscattering set-up consist of a helium ion source, a Van de Graaff accelerator to accelerate the particle to high energy and a detector to detect the backscattering ions. The maximum energy of this machine is 2.7 MeV but for this study 1.4 and 1.6 MeV energies were used.

The charged helium ions produced by the RF source are accelerated to high energies via high potential through an accelerating tube based on the principle by van de Graaff [Gra31] [Grob84]. This ion beam was produced by applying a dipole magnet deflection as mass and charge state separator. The ion beam was deflected into the beamline and directed to the target chamber. This was done by combining the horizontal and vertical slits allowing focusing and collimation of the beam. The magnet deflects the beam into either the left beamline or the right beamline. The left beamline has a vacuum chamber that is designed to operate below room temperature while the right beamline works at room temperature. The right beamline was used for this study. The analyzing chamber consists of a stage for mounting samples which is connected to a three-axis goniometer for controlled rotating of the samples, a solid state

detector, a 1 mm diameter collimator connected the beamline, and the vacuum pump (fore pump and turbo pump) system. The energy of the backscattered helium ions were recorded by a solid-state detector (SSD). The signal from the detector is amplified and digitized by an analogue to digital converter (ADC) inside the multi-chamber chamber analyzer (MCA). The output signal is stored in a computer which is connected to the MCA. A spectrum of yield versus channel number is obtained and saved in a computer.

The helium ions backscattered from the target which are incident on the detector create electron-hole pairs. The electron-hole pairs are separated by an applied electric field with a reverse bias voltage of 40 V and create a charge pulse. The energy of the backscattered ions is measured by a Si surface barrier detector which is located at a scattering angle of 165°.

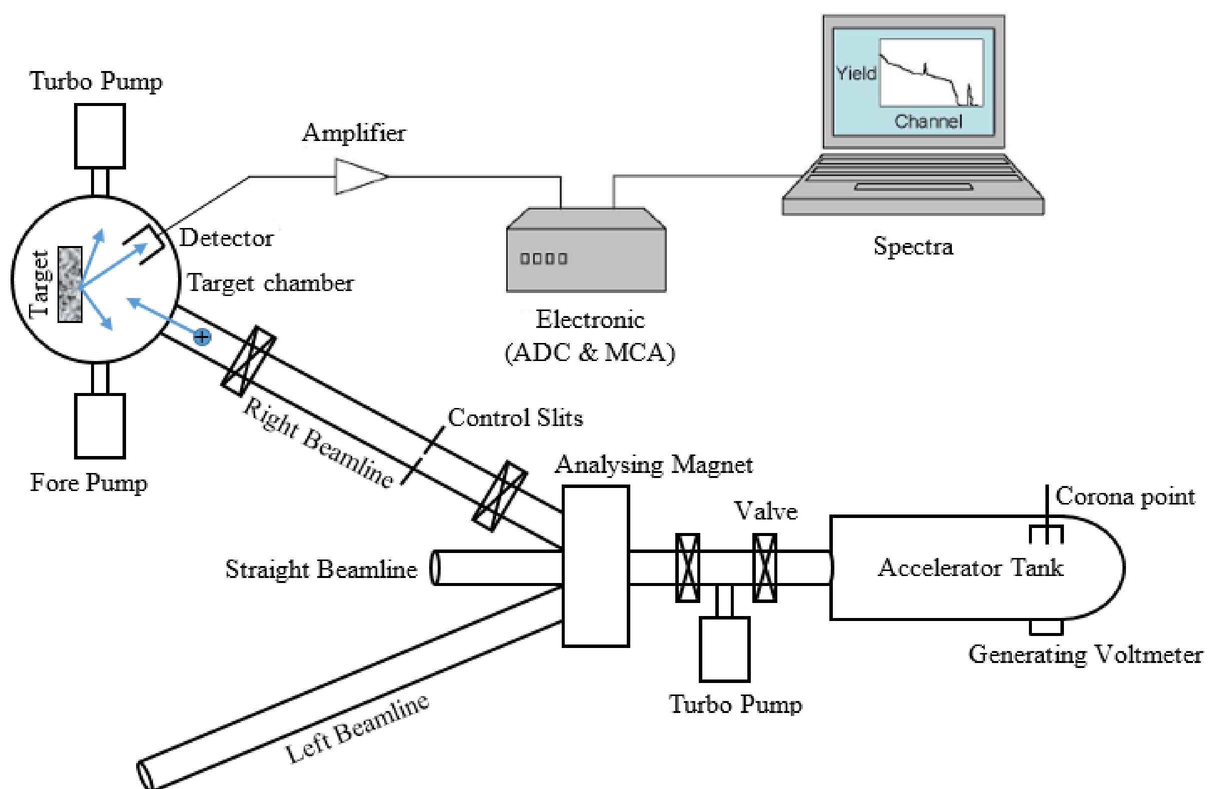

Fig. 5.1: Design of RBS set-up at the University of Pretoria.

During analyses, the maximum beam current is kept at about 15 nA to avoid heating of the sample and also to avoid very significant factors which affect the RBS measurement during the process of detecting backscattered helium ions. These factors are dead time, pile-up and ballistic deficit. Dead time is a minimum time of two separate events which can be recorded as two separate independent events for proper detection of the counting system. Pile-up is a

second factor, occurs when the time response of the detector system is not fast enough to separate the individual events on the detector due to the high rate of encountered events. Therefore, in such a situation two events may eventually be recorded as one event, which will falsify the measurements. In pile-up, the summed pulse is produced when two pulses combine leading to energy degradation as well as count rate loss.

MCA is a major contributor to the dead time in the counting system. Based on the design, MCA can produce pile-up and/or deadtime problems. The main contributor in MCA deadtime is the ADC. A schematic diagram of a typical pulse counting system is shown in figure 5.2, which also gives an overview of the dead time associated with various units. The ballistic deficit is defined as the phenomenon when the slow components of the ions do not contribute to the pulse in the pulse shaping stage, hence pulse amplitude is reduced. The shaping time constant of the amplified pulse must be significantly larger than the rise time of the pulse, otherwise, the amplitude information of the shaped pulse will be lost. The ballistic deficit is not a major concern as long as the charge collection time and consequently, the preamplifier's pulse rise time is constant for all pulses.

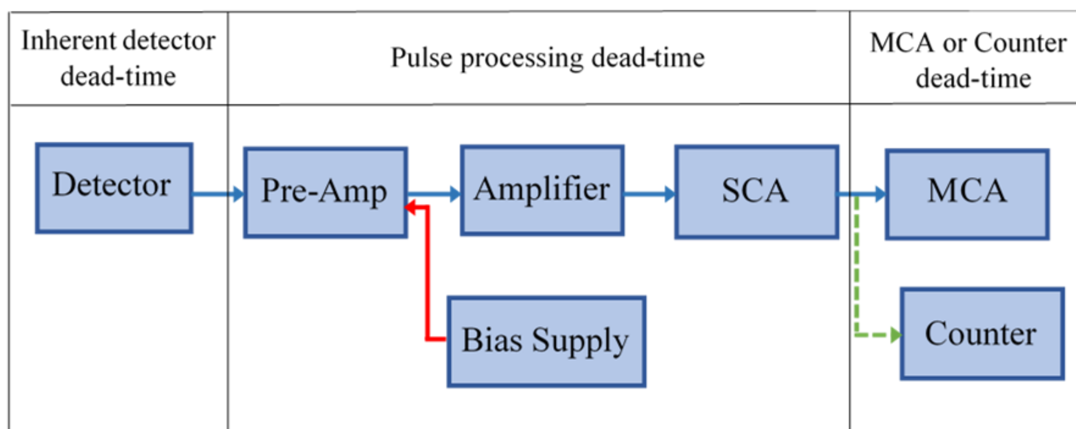

Fig. 5.2: Sources of deadtime in a typical detection system. Redrawn from [Usm18].

5.1.2 Principle and theory of Rutherford Backscattering Spectrometry

The Rutherford backscattering technique was first used in 1913. Following detailed experiments by Geiger and Marsden to test and confirm all the predictions of Rutherford's model for the atom and He^+ particle scattering from foils of various metals [Rut11]. The first

real use of RBS was done by nuclear physicists. They discovered using particle accelerators that the backscattering from their target which contained contaminants that the latter appeared as a parasitic effect in the nuclear reaction particle spectra [Tol49] [Gro84].
RBS is well known for quantitative compositional analysis of thin films. In 1967, Surveyor V used an alpha scattering experiment to analyse the composition of the moon's soil. Earlier, in 1960 the method was suggested by S. K. Allison for the remote analysis of surface composition [Chu78]. In addition, it is non-destructive, has a good depth resolution of the order of several nm, and very good sensitivity for heavy elements. Furthermore, RBS has become a popular widely used nuclear method in ion beam analysis in thin films and the surface layer of solids.

5.1.3 Kinematic Factor (K)

The process of energy transfer from the incident projectile ions (alpha particles) to target atoms is known as the kinematic factor (see Fig 5.3). This process can be described by considering the conservation of energy and momentum [Chu78] [Gro84]. Then, the ratio of the projectile energy (E_o) before and (E_1) after the collision is given as:

$$K = \frac{E_1}{E_o} = \left[\frac{M_1 \cos\theta \pm (M_2^2 - M_1^2 \sin^2\theta)^{½}}{M_1 + M_2}\right]^2 \quad (5.1)$$

where M_1 and M_2 are a projectile (alpha particle) and a target masses respectively, θ is the scattering angle. When $M_1 < M_2$, only the plus sign in equation (5.1) above holds. If $M_1 \geq M_2$ equation (5.1) above has two solutions, and the maximum possible scattering angle is given by equation (5.2) below.

$$\theta_{max} = \arcsin\left(\frac{M_2}{M_1}\right) \quad (5.2)$$

Generally, the kinematic factor is used for calibration of the RBS spectrum. Using the kinematic factor and beam energy, the backscattered particle's energy can be estimated. This can also be applied to determine the mass of an unknown target atom from measured energy E_1 and consequently identifying the target atoms [Chu78]. The kinematic factor increases with

the target mass and tends toward heavy masses, thus the mass separation on the RBS energy spectrum decreases when the mass increases.

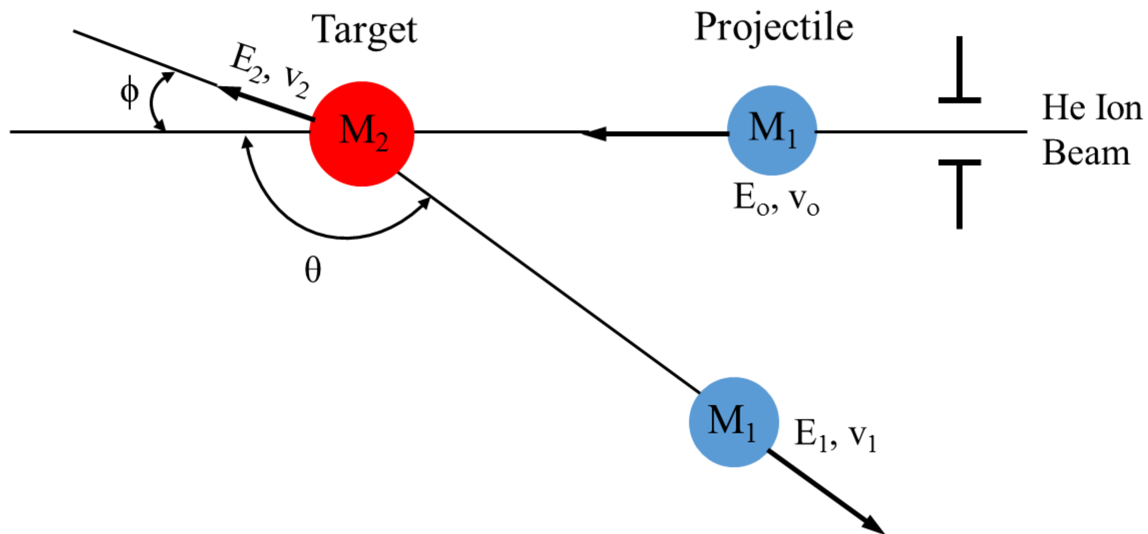

Fig. 5.3: A typical schematic of scattering between projectile and target atom.

5.1.4 Scattering cross section (σ)

A small fraction of the projectiles is usually backscattered at a certain angle, θ, from the target atoms into the detector. The differential cross section for scattering ($d\sigma/d\Omega$) is defined as the number of particles backscattered into a solid angle $d\Omega$ per number of incident particles per unit area. The differential cross section for the scattering of a projectile into a solid angle $d\Omega$ centered around an angle θ in the laboratory frame of reference is given as [Chu78][Gro84]:

$$\frac{\mathrm{d}\sigma}{\mathrm{d}\Omega} = \left(\frac{Z_1 Z_2 e^2}{4E}\right)^2 4\,\frac{\left[(M_2^2 - M_1^2 \sin^2\theta)^{1/2} + M_2 \cos\theta\right]^2}{M_2 \sin^4\theta\,(M_2^2 - M_1^2 \sin^2\theta)^{1/2}} \qquad (5.3)$$

where Z_1 is the atomic number of the projectile with mass M_1, Z_2 is the atomic number of the target with mass M_2, E_O is the energy of the projectile before scattering, e is the electron charge and θ is the backscattering angle.

Since the differential cross section is proportional to Z_2^2, for any projectile, heavy atoms scatter much more efficiently than light atoms. This means the RBS is more sensitive to targets with heavy elements than to light elements. The inversely proportionality of E_O to the differential

cross section, means one would expect the yield of backscattered particles to increase with decreasing bombarding energy. The total number of backscattered and detected particles is given by:

$$A = \sigma\,\Omega\,.\,\mathrm{Q}\,.\,N \qquad (5.4)$$

where σ is the differential cross section, Ω is the solid angle of the detector, Q is the total number of incident projectiles and N is the number of target atoms per unit area. From equation (5.4) when σ and Ω are known, and the numbers of the incident and detected particles are counted, the number of atoms per unit area in the target, N, can be determined.

5.1.5 Depth scaling

Depth scaling (also known as depth profiling) describes the relationship between the exit energy E_1 of the alpha particle backscattered at depth x inside the target and the incident particle with energy E_o backscattering at the surface as illustrated in figure 5.4. The alpha particle backscatters at the surface with an energy of KE_o while the one which backscatters at depth x have an initial energy E. Since E is lower than E_o, there is loses in energy before backscattering at depth x. The backscattered particle at depth, x loses energy on its way out of the target. From figure 5.4 also, the length of the inward path where the ion loses energy is $x/cos\theta_1$ and the length of the outward path is $x/cos\theta_2$. By assuming the energy loss (dE/dx) is constant over each path, the energy of the backscattered alpha particle at depth x is then given as [Chu78] [Wan09]:

$$KE_{\mathrm{o}} - E_1 = \left[\left(\frac{K}{cos\theta_1}\frac{dE}{dx}\right)_{in} + \left(\frac{K}{cos\theta_2}\frac{dE}{dx}\right)_{out}\right]x \qquad (5.5)$$

where KE_o is the energy of the backscattered particles at the surface atoms of the target and E_1 is the energy of the backscattered alpha particle from the atom at depth x. If we take ΔE as the energy difference between E_1 and KE_o, then

$$\Delta E = KE_{\mathrm{o}} - E_1 \qquad (5.6)$$

and equation (5.6) can be written as:

$$\Delta E = [S]x \tag{5.7}$$

where

$$[S] = \left[\left(\frac{K}{cos\theta_1}\frac{dE}{dx}\right)_{in} + \left(\frac{K}{cos\theta_2}\frac{dE}{dx}\right)_{out}\right] \tag{5.8}$$

[S] is called the energy loss factor which contains the relationship between the energy and the depth information. This means a measured energy spectrum can, therefore, be directly converted into a depth scale.

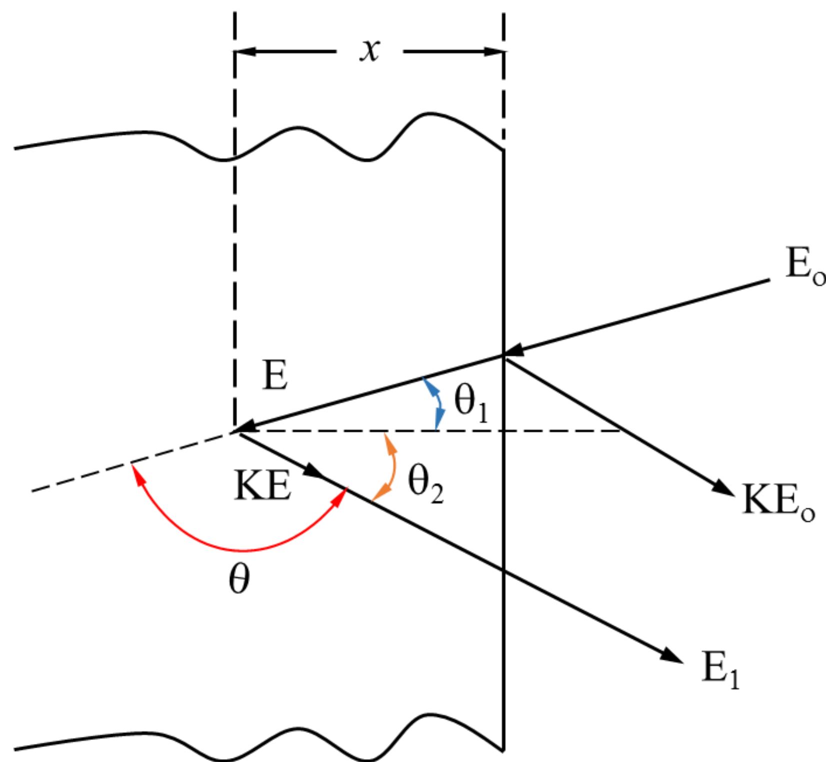

Fig. 5.4: A schematic diagram illustrating the backscattering events of alpha particles and energy loss from depth *x* [Chu78].

5.1.6 Depth resolution

A minimum detectable in-depth difference (δx) which related to the minimum detectable scattered particle energy difference, (δE) is known as depth resolution. Energy

straggling increases as the ion beam penetrates deeper into the sample. Therefore, depth resolution is better near the surface and degrades due to energy straggling in deeper layers [Jey09]. The depth resolution can be improved by increasing [S]. This is usually done by tilting the sample normal relative to the incoming beam (i.e., increasing θ_1 and/or θ_2). The effect is to increase the path length required to reach a given depth (measured perpendicular to the surface) in the sample. This increases the energy difference of the scattered particle for a given depth difference [Wan09].

5.2 Raman Spectroscopy

The phenomenon of inelastic scattering of light was first postulated by Smekal in 1923. It first observed experimentally in 1928 by Raman and Krishnan [Smi05]. Since then, the phenomenon has been referred to as Raman spectroscopy. The experiment used sunlight as the source, a telescope as the collector, and the eye as the detector [Fer03].

Raman scattering is based on the scattering of monochromatic light (photons), usually from a laser source. When photons of energy E_o interact with a sample molecule, it is absorbed by the sample and then re-emitted. A small proportion of these incident photons are however scattered at optical frequencies that differ from that of the incident photons [Gra89]. The frequency of the re-emitted photons is shifted up or down in comparison with the incident photons frequency, which is known as the Raman Effect. This shift provides information about vibrational, rotational and other low frequency transitions in molecules. Due to its sensitivity, high information content, and non-destructive nature Raman spectroscopy can be used to study the microstructure of carbon related materials such as graphite, diamond, glassy carbon, etc.

5.2.1 Theory and principle of Raman Spectroscopy

When a sample is irradiated with a light source, most photons are scattered by the sample at the same frequency as the incident light frequency (ν_o), the process is known as Rayleigh scattering. This scattering process is regarded as elastic scattering between the incident photon and the molecule.

The Raman scattering process from the ground vibrational state (m) leads to absorption of energy by the molecule and its elevated to a higher energy excited vibrational state (n). Figure 5.5 shows the other two types of Raman scattering are very weak (about 10^{-5} of the incident beam) and have frequencies ($\nu_o \pm \nu_m$), where ν_m is a vibrational frequency of a molecule. The (ν_o - ν_m) and ($\nu_o + \nu_m$) lines are called the Stokes and anti-Stokes scattering respectively. Molecules initially in the ground vibrational state give rise to Stokes Raman scattering (ν_o - ν_m) while molecules initially in the vibrational excited state give rise to anti-Stokes Raman scattering, ($\nu_o + \nu_m$). In Raman spectroscopy, we measure the vibrational frequency (ν_m) as a shift from the incident beam frequency (ν_o) [Fer03] [Lew01].

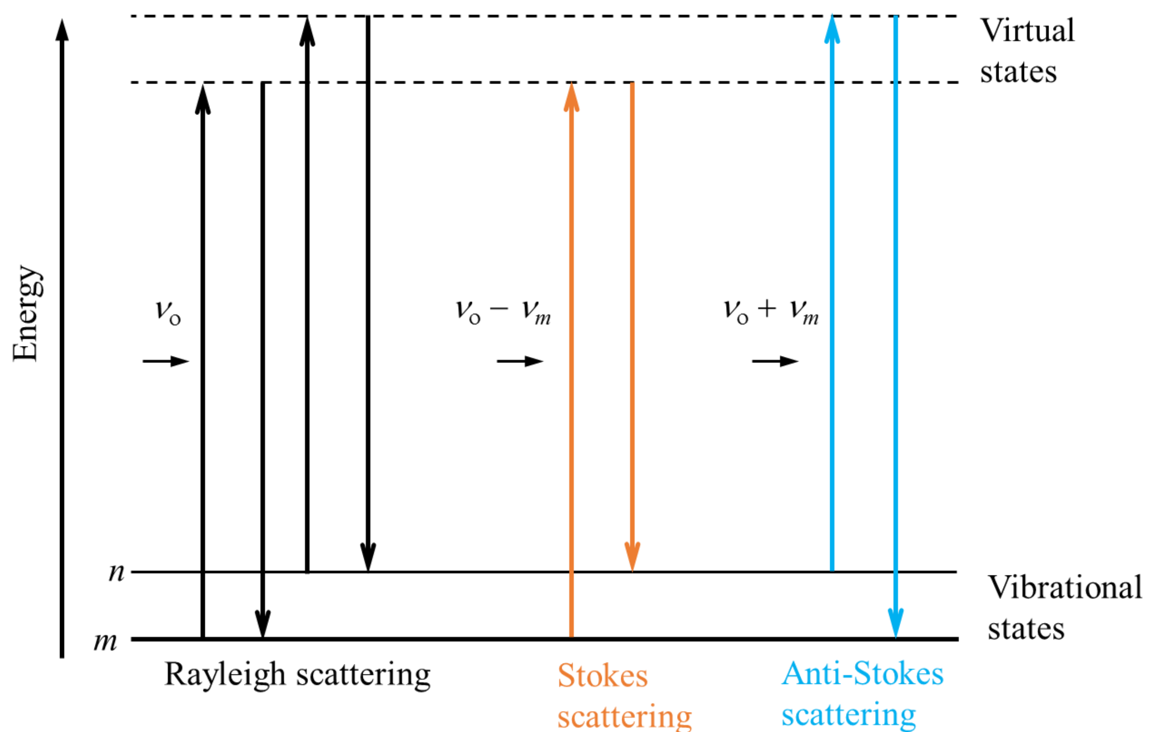

Fig. 5.5: Schematic illustration of the Rayleigh and Raman scattering processes. Both the low energy (upward arrows) and the scattered energy (downward arrows) have much larger energies than the energy of vibration.

When the incident photons interact with a molecule, the molecule experiences an electric field. As a result, the electrons are displaced relative to the protons and the polarized molecule has an induced dipole moment caused by the external electric field. The electric field E at a given time (t) and associated with the photon can be expressed as:

$$E = E_o cos2\pi\nu t \qquad (5.9)$$

where E_o is the maximum amplitude (the maximum value of the field) and ν is the frequency. This electric field will induce in the molecule an oscillating dipole moment, μ given by

$$\mu = \alpha E \ = \alpha E_o cos2\pi\nu t \qquad (5.10)$$

In molecules, the polarizability does not have a constant value, due to vibrations and rotations which causes α to vary. For small displacements, the polarizability can be expanded in a Taylor series as [Col90].

$$\alpha = \alpha_o + \frac{\partial x}{\partial Q} Q + \cdots \qquad (5.11)$$

where α_o is the equilibrium polarizability, Q is a normal coordinate and $\partial\alpha/\partial Q$ is the rate of change of polarizability with respect to Q measured at the equilibrium configuration. If higher order terms can be neglected, then the normal coordinate Q varies periodically and can be written

$$Q = Q_o cos2\pi\nu_\upsilon t \qquad (5.12)$$

where ν_υ is the frequency of the normal coordinate vibration and Q_o is a constant, the maximum value for Q. By combining equations (5.11) and (5.12)

$$\alpha = \alpha_o + \frac{\partial\alpha}{\partial Q} Q_o cos2\pi\nu_\upsilon t \qquad (5.13)$$

Substitution this value for α into equation (5.10) yields

$$\mu = \alpha_o E_o cos2\pi\nu t + \frac{\partial\alpha}{\partial Q} Q_o E_o (cos2\pi\nu_\upsilon t)(cos2\pi\nu t) \qquad (5.14)$$

Making use of trigonometric, equation (5.14) can be rewritten as:

$$\mu = \alpha_o E_o cos2\pi\nu t + \frac{\partial\alpha}{\partial Q}\frac{Q_o E_o}{2}[cos2\pi(\nu - \nu_\upsilon)t + cos2\pi(\nu + \nu_\upsilon)t\,] \tag{5.15}$$

It can be seen from this equation that the induced dipole moment μ varies with three component frequencies ν, $\nu - \nu_\upsilon$, and $\nu + \nu_\upsilon$ and can, therefore, give rise to Rayleigh scattering, Stokes, and anti-Stokes Raman scattering, respectively. This classical prediction for these frequencies corresponds to the quantum mechanical result for Raman transitions when $\Delta v = \pm 1$. If the vibrations cause no change in polarizability so that $\partial\alpha/\partial Q = 0$, then Eq. (1.117) shows that the Raman component frequencies of the induced dipole moment have zero amplitudes and therefore no radiation with Raman frequencies can be generated [Col90].

5.2.2 The Raman instrument

The Raman instrument setup consists of the following elements: Laser source (usually gas continuous-wave lasers such as Ar^+, Kr^+, and He-Ne), Raman light collector, monochromator, and detector. The highest intensity wavelengths include 515.4 nm (the wavelength that which was used in this study). The Raman scattered light is collected by the lens and passes through a monochromator. A schematic diagram of the Raman setup is shown in figure 5.2 below.

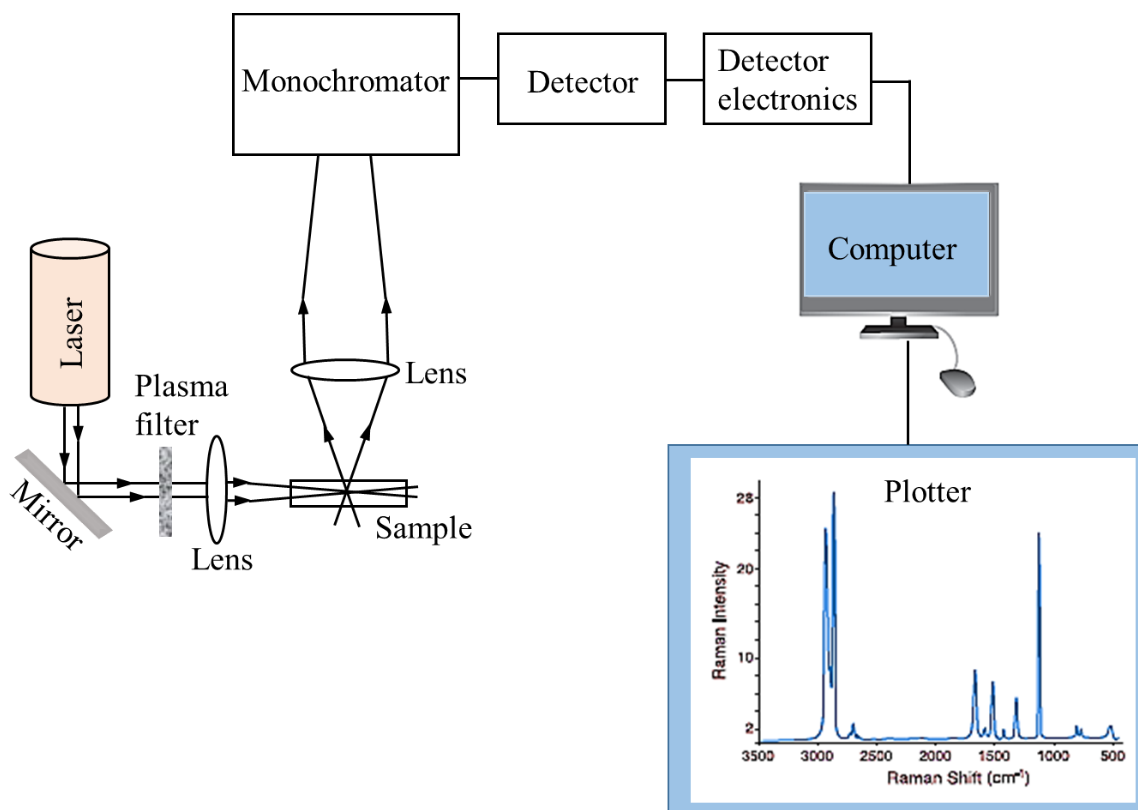

Fig. 5.6: Schematic diagram showing the different components of a Raman instrument.

5.3 Scanning Electron Microscopy

A scanning electron microscopy (SEM) is a method that uses electrons rather than light for high resolution imaging of surfaces. The advantages of SEM over light microscopy include much higher magnification (>100,000X) and greater depth of field up to 100 times than conventional light microscopy [Vou08]. The first SEM was built around 1938 (Von Ardenne), with the first commercial instrument around 1965. The electrons are produced in the electron gun by the electron beam source. The function of the electron gun is to provide a stable electron beam of adjustable energy.

A scanning electron microscopy uses a beam of electrons to form an image of objects on a very fine scale. These electrons are generated by an electron gun which provides a stable beam of electrons of adjustable energy. The electron guns consist of three major types: the tungsten filament, Lanthanum hexaboride (LaB6) and field emission [Haf07]. The older SEMs use heated tungsten or LaB6 thermionic emitters while some of the new SEMs are equipped with cold thermal or Schottky field emission sources. A field emission cathode is usually a wire shaped into a sharp tip (100 nm or less radius) supported by a tungsten hairpin. When the field

at the tip reaches a magnitude of about 10V/nm, electrons are emitted. A cathode current density as high as 105 A/cm^2 may be obtained from a field emitter as compared with 3 A/cm^2 from a thermionic source [Hla10] [Gol03].

There are two types of field electron guns, the cold field emitter and the Schottky field emitter. The cold field emitters require ultra-high vacuum conditions to ensure that the tip is clean and void of contaminants and oxides. The tip is usually flushed (heated for a few seconds) before operation so as to free absorbed gas molecules. The Schottky field emitter uses both heat and nitride coatings to overcome the potential barrier level. The FEGs (Field Emission Guns) are preferable to the tungsten filament and the Lanthanum hexaboride (LaB_6) emission guns. Because of the filaments last longer (due to the cold emission), it produces better resolution and the images produced are brighter. The disadvantages of the FEGs are that a much higher vacuum and a cleaner vacuum microscope are required [Odu17] [Dun97].

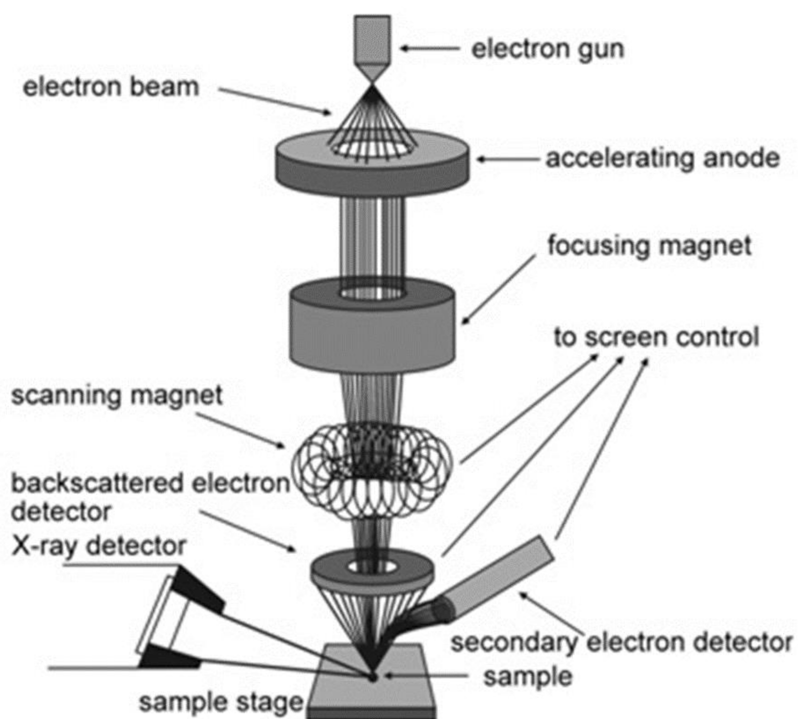

Fig. 5.7: Schematic diagram showing how the scanning electron microscope works [www1].

When an incident electron beam interacts with a sample, the incident electron undergoes two types of scattering elastic and inelastic scattering events within the sample's surface and near-surface material. These interactions give rise to various signal events such as backscattered

electrons, secondary electrons, X-rays, cathode luminescence, specimen current and transmitted electrons. However, this thesis, discussed only backscattered and secondary electrons.

The backscattered electrons (BSE) are as a result of an elastic collision between an incoming electron and the nucleus of the target atom. Their energy range they provide information from deeper layers. Accordingly, in this case the resolution is poorer, (about 2-4 nm). The element with higher atomic number (Z) will backscatter more electrons and appear brighter than an element with low atomic number. These electrons usually have higher energies compared to the energies of the secondary electrons.

Secondary electrons are as the results of the inelastic collisions between the incident electrons and the electrons of the target atoms. These electrons have energy less than 50 eV. The signals from secondary electrons can be used to study the surface topography of the sample. Due to their low energy, only secondary electrons that are very near the surface (a few nanometers) can exit the sample and be examine, the others electrons can simply absorbed by the sample due to their low energy [Gol03] [Vou08].

To create a SEM image, the incident electron beam is scanned in a raster pattern across the sample's surface. The emitted electrons are detected for each position in the scanned area by an electron detector. The intensity of the emitted electron signal is displayed as brightness on a cathode ray tube (CRT). By synchronizing the CRT scan to that of the scan of the incident electron beam, the CRT display represents the morphology of the sample surface area scanned by the beam. Magnification of the CRT image is the ratio of the image display size to the sample area scanned by the electron beam [www2].

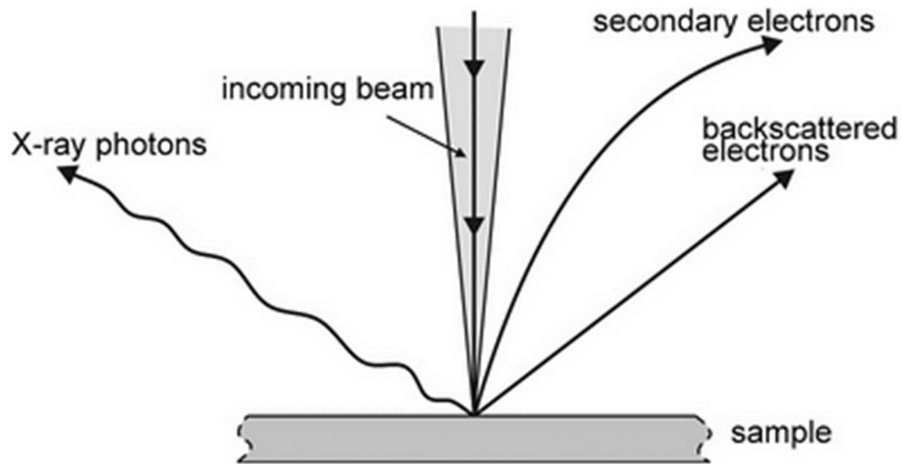

Fig. **5**.8: Diagram showing electron Beam interaction [www1].

In this study, the surface changes of glassy carbon as a result of xenon ion implantation and after heat treatment were investigated using a Zeiss Ultra 55 field emission scanning electron microscope fitted with an in-lens detector. This machine employs a field emission electron gun. The Zeiss Ultra 55 is equipped with SE (secondary electron) detectors, BE (backscattered electron) detectors and an in-lens SE detector. A 2 kV accelerating voltage was employed during all SEM imaging. The working distance was maintained at approximately 2.8 mm for all the imaging experiment and the magnifications, 1 um, 100 nm and 200 nm were used.

References

[Col90] N. B. Colthup, Lawrence H. Daly and Stephen E. Wiberley, Introduction to Infrared and Raman spectroscopy, 3rd ed., Academic Press, Inc., USA, 1990.

[Dun97] M. Dunlap, J.E. Adaskaveg, Introduction to the Scanning Electron Microscope, Theory, Pract. Proced. Facil. Adv. Instrumentation. UC Davis. 52 (1997).

[Fer03] J. R. Ferraro, Kazuo Nakamoto and Chris W. Brown, Introductory Raman Spectroscopy, 2nd ed., Elsevier Science, USA, 2003.

[Gra31] R.J. Van De Graaff, A 1,500,000 volt electrostatic generator, *Physical Review* **38** (1931) 1919 – 1920.

[Gra89] D. J. Gardiner and P. R. Graves, Practical Raman Spectroscopy, Springer-Verlag, Berlin Heidelberg, 1989.

[Gol03] J.I. Goldstein, D.E. Newbury, P. Echlin, D.C. Joy, A.D. Romig, C.E. Lyman, C. Fiori, E. Lifshin, Scanning electron microscopy and x-ray microanalysis, 3rd ed., Springer, New York, 2003.

[Gro84] J.J. Grob, P. Siffert, Rutherford backscattering spectroscopy (RBS), *Progress in Crystal Growth and Characterization* **8** (1984) 59 – 106.

[Haf07] B. Hafner, Scanning Electron Microscopy Primer, Charact. Facil. Univ. Minnesota-Twin Cities. (2007).

[Hla10] T.T. Hlatshwayo, Diffusion of silver in 6H-SiC, PhD Thesis, University of Pretoria, 2010.

[Jey09] C.Jeynes and N.P.Barradas, Pitfalls in Ion Beam Analysis, 2009.

[Len13] Yang Leng, Materials Characterization: Introduction to Microscopic and Spectroscopic Methods, 2nd ed, Wiley-VCH Verlag GmbH, Germany, 2013.

[Lew01] Ian R. Lewis and Howell G. M. Edwards, Handbook of Raman Spectroscopy, Marcel Dekker, Inc., New York, 2001.

[Odu16] O. S. Odutemowo, Modification of glassy carbon under strontium ion implantation, PhD Thesis, University of Pretoria 2017.

[Rut11] E. Rutherford, The Scattering of α and β Particles by Matter and the Structure of the Atom, *Philosophical Magazine* **6**, 21 (1911).

[Smi05] E. Smith, G. Dent, Modern Raman spectroscopy: a practical approach, John Wiley & Sons Ltd, England, 2005.

[Tol49] A. V Tollestrup, W.A. Fowler, C.C. Lauritsen, Energy release in beryllium and lithium reactions with protons, *Physical Review* **76** (1949) 428 – 430.

[Usm18] S. Usman and A. Patil, Radiation detector deadtime and pile up, *Nuclear Engineering and Technology* **50** (2018) 1006 – 1016.

[Vou08] B. Voutou, E. C. Stefanaki, Electron Microscopy: The Basics, *Physics of Advanced Materials Winter School* **1** (2008).

[Wan09] Yongqiang Wang and Michael Nastasi, Handbook of Modern Ion Beam Materials analysis 2nd ed, Materials Research Society, USA, 2009.

[www1] High-Resolution Scanning Electron Microscopy. http://www.technoorg.hu/news-and-events/articles (accessed June 20, 2019).

[www2] Materials Evaluation and Engineering, Inc., 2001, https://www.mee-inc.com. (accessed August 11, 2016)

CHAPTER 6

EXPERIMENTAL PROCEDURES

SIGRADUR® G glassy carbon samples strip with 50 mm × 10 mm dimensions and a thickness of 2 mm were implanted with xenon ions. The migration behaviour, structural changes and surface modification of the xenon ion implanted glassy carbon samples were investigated using RBS, Raman spectroscopy, and SEM respectively.

6.1 Sample preparation

The samples used for this research were SIGRADUR® G glassy carbon samples from Hochtemperatur-Werkstoffe (HTW), Germany. The company produces both SIGRADUR® G and SIGRADUR® K glassy carbon materials, however, the SIGRADUR® G carbon materials were a preferred choice for this study due to its superiority over SIGRADUR® K materials. Although the SIGRADUR® K materials are relatively denser and harder than the SIGRADUR® G, the SIGRADUR® G carbon materials have higher conductivity, higher corrosion resistance, and high temperature resistance.

Step 1, samples were mechanically polished on an ATM Saphir 500 polisher with 1μm and 0.25μm diamond solutions respectively before being cleaned. Step 2, samples were placed in an ultrasonic bath and first cleaned in an alkaline soap solution. Step 3, samples were then transferred to a new beaker containing de-ionized water. The de-ionized water was used to remove the soap solution from the sample and this was done twice for ten minutes. Step 4, Methanol was then used to clean the samples for 5 minutes so as to remove the de-ionized water. Step 5, samples were dried by blowing nitrogen gas on them for a few minutes and then placed in an oven at 50 ^{o}C for 1h so as to remove volatile impurities on the surface of the carbon samples.

6.2 Implantation procedures

After cleaning, the samples were implanted with xenon ions by the 400 keV ion implanter Romeo at the Institut für Festkörperphysik, Friedrich-Schiller-Universität Jena, Jena,

Germany. The xenon ions were implanted at room temperature at an energy of 200 keV with a fluence of 1×10^{16} ions/cm^2. Because of our interest in studying the radiation damage as a result of ion bombardment and structural changes in glassy carbon. The beam current was kept at about 8000 nA while the time was 1 h 3 min along the implantation process, in order to avoid annealing out of some of the damages due to an increase in the substrate material temperature. During implantation, the substrate reached a maximum temperature of about 55 °C.
After implantation, the samples were cut into 10 mm ×5 mm using a tungsten carbide (WC) cutter. This was to ensure that the samples fit into sample holders that have been specifically made for RBS and SEM analysis.

To wash off the dust particles, the samples were again cleaned with de-ionized water and methanol. This was done in order to remove/prevent contamination present on the surface.

6.3 Annealing of samples

Two annealing systems were used in this study. Isochronal annealing at low and high temperatures was employed in this research. The sample was placed in a quartz vacuum tube furnace which can annealed at a maximum temperature of 1000 °C. A schematic diagram of the annealing equipment is shown in Figure 6.1. After the sample was held, the quartz tube was evacuated to below 10^{-3} mbar by the fore pump, and then the turbo pump system was turned on. The turbo pump shown in the Figure 6.1 below provides high vacuum (up to 10^{-7} mbar) during annealing. A thermocouple was placed close to the sample in order to measure and monitor its temperature using a computer program.
Before annealing was performed, the oven was allowed to stabilise at the required annealing temperature. The oven was shifted over the quartz vacuum tube until the sample was in the middle of the oven for annealing. This step ensured that the sample quickly reached the required temperature. At the end of the annealing time, the oven was pulled back and the sample was then allowed to cool down to room temperature. The sample was then removed after the fore pump and turbo pump had been turned off and the turbo pump blades have stopped rotating. Usually, it takes about one hours for the turbo pump blades to totally stop rotating. The annealing temperature range was from 300 °C to 1000 °C in steps of 100 °C for 5 hours.
For the high temperatures annealing (1000 °C to 1500 °C in steps of 100 °C for 5 hours), the samples were placed inside small crucibles made from glassy carbon. The annealing was

performed in a computer controlled high temperature vacuum graphite furnace (Webb® 77). The temperature is controlled by a Eurotherm 2704 controller connected to a thermocouple as well as a pyrometer. The thermocouple was employed for measurements below 1475 °C and the pyrometer for measurements above 1525 °C [Kuh15] [Web06]. An average value of the thermocouple and pyrometer readings is used in the temperature range in between the 1475 °C and 1525 °C.

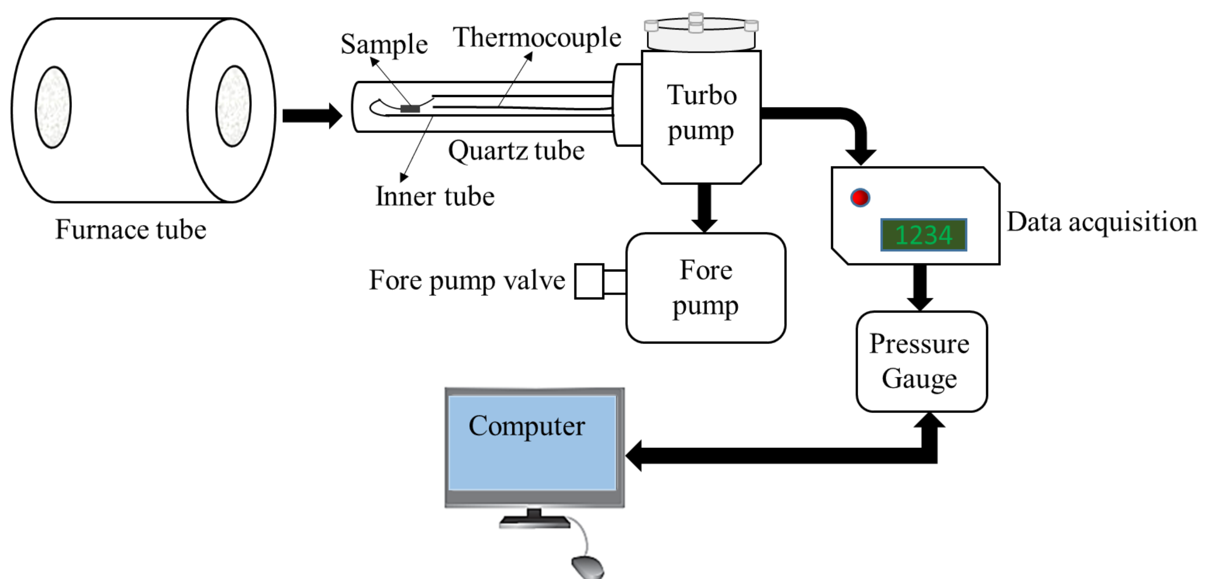

Fig. 6.1: Schematic diagram showing one of the annealing systems used in this research.

Figure 6.2 below is an illustration of a typical heating up and cooling down curves. The nominal temperature accuracy for the Webb oven is given ± 15 °C.
Figure 6.2 also shows a typical heating and cooling curves for the furnace as a function of time. Before each annealing cycle, the oven was evacuated to a pressure in the 10^{-7} mbar range. Degassing was performed at 200 °C for one hour to ensure that the maximum pressure during annealing is kept at or below the 10^{-6} mbar region as well as to reduce the total pumping time. The degassing temperature overshoot from 200 °C to 370 °C. This was due to temperature controlling setting-up by the manufacture, which resulted in the initial large current and fluctuations. During the annealing process the vacuum pressure increases from 10^{-7} to 10^{-5} mbar due to the increased degassing by the high initial current. The heating rate of the oven was programmed at 20 °C/min. After switching on the heating element, it heated up to a selected temperature (i.e. 1500 °C as seen in Figure. 6.2 and then stayed there for the set

annealing time, i.e. 5 hours. A current of about 28 A was measured in the beginning of the heating process, which later dropped to 0 A. After degassing, which was performed at 200 °C, the current increased again up to 18 A to increase the temperature inside the oven to the selected temperature (i.e. 1500 °C). The current was dropped to 8 A during the desired annealing temperature for 5h. At the end of annealing time, the current was turned off and the system cooled down. To remove the samples from the oven, after the oven completely cooled down and reach room temperature, the vacuum was brought down by switching off the turbo pump (i.e. high vacuum pump), still pumping with the fore pump. Argon gas was leaked into the chamber to break the vacuum and bring the pressure to atmospheric pressure.

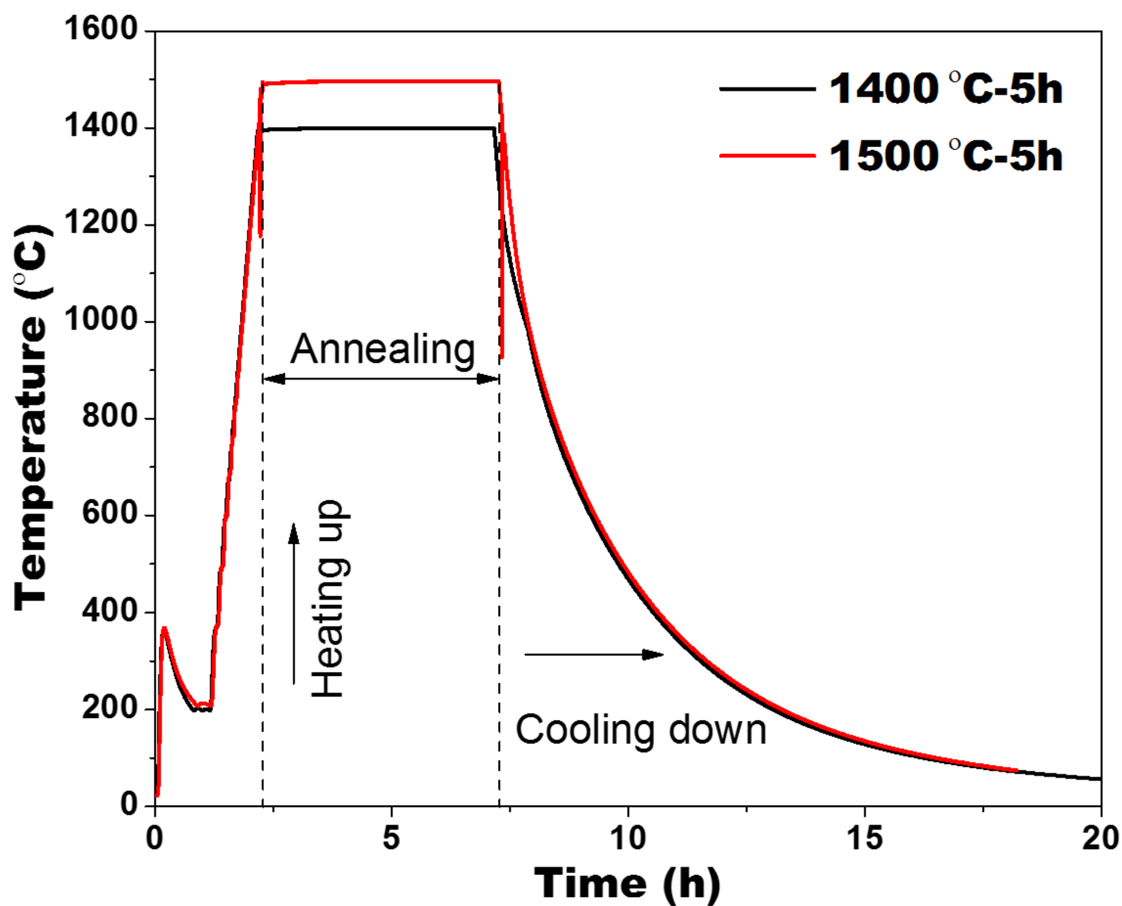

Fig. 6.2: Graph showing the annealing process at different temperatures.

6.4 The measurement conditions

6.4.1 The RBS measurement

The implanted glassy carbon samples were analysed using Rutherford backscattering spectrometry before and after each annealing. The samples were irradiated with 1.6 MeV helium particles in the Van de Graaff accelerator at the University of Pretoria. A total charge of 8 μC, in order to reduce noise, the measurement was repeated three times for each sample. The sample tilt angle was kept at 10° while the surface barrier detector with a solid angle of 3.41 msr was positioned at a scattering angle of 165°. For uniformity, the maximum beam current was kept at 15 nA throughout the study.

6.4.2 Raman measurement

The structural changes as a result of ion implantation and annealing were monitored using Raman spectroscopy. The resulting Raman spectra before and after ion bombardment and heat treatment were obtained at an excitation wavelength of 514.5 nm. The 514.5 nm wavelength was excited using a Jobin Yvon, Horiba© TX64000 triple grating. The excitation laser used in this study was an Ar/Kr mixed gas laser with a maximum power of 0.17 mW during the measurement. The 50× objective was used to acquire the Raman spectra.

6.4.3 The SEM measurement

Surface changes of the glassy carbon samples due to ion implantation and heat treatment were investigated using the Zeiss Ultra Plus SEM located at the University of Pretoria. An analysing voltage of 2 kV was used throughout this work. In-lens SEM images of the sample were taken before, after implantation and after every heat treatment. The working distance was kept at 2.8 mm and magnifications of 1μm, 100 nm and 200 nm respectively were used.

References

[Web06] R.D. Webb Company, operating manual Webb® 77, 2006.

[Kuh15] R. J. Kuhudzai, Diffusion and surface effects for SiC implanted with fission product elements, PhD Thesis, Department of Physics, University of Pretoria, South Africa, 2015.

CHAPTER 7

RESULTS AND DUSCUSSION

In this chapter, the effect of xenon ion bombardment and heat treatment on glassy carbon is presented and discussed. The migration behaviour of the implanted xenon in glassy carbon due to heat treatment at different temperatures and after SHI irradiation was investigated using RBS. The structural changes of the implanted samples were investigated using Raman spectroscopy and TEM, while the surface morphology of the sample was investigated using SEM and AFM.

7.1 Implantation of glassy carbon with xenon

Figure 7.1 shows the RBS depth profile of 200 keV Xe implanted in glassy carbon to a fluence of 1×10^{16} cm^{-2} at room temperature. The RBS profile was compared with the theoretical spectra obtained from the TRIM ion distribution simulation software. Also shown in Figure. 7.1 is the profile showing the damage introduced in glassy carbon simulated using the TRIM program. The TRIM simulations were carried out by taking the density of glassy carbon as 1.42 g/cm^3. This value is the density of the virgin Sigradur® G glassy carbon samples used in this study. The experimental projected range, R_p, was estimated by fitting the Xe depth profile with a Gaussian equation. The value obtained of 119.3 nm is comparable to the 119.7 nm obtained from TRIM. The two values differ by about 0.3 % and is within the accuracy of TRIM. The experimental straggling, ΔR_p value obtained was about 34.2 nm which is about 36.8 % higher than the 21.6 nm obtained from TRIM. The higher ΔR_p obtained from the as-implanted Xe profile suggests a broader ion distribution to that suggested by TRIM. This discrepancy in the ΔR_P might implies that re-distribution of Xe is already taking place during the implantation process.

The maximum damage level of 29 dpa was obtained and significantly higher than the reported critical displacement per atom (dpa) value of 0.2 dpa for amorphisation of glassy carbon [McC94]. McCulloch *et al*. [McC94] studied the structural changes in glassy carbon due to xenon ion irradiation. In their study, glassy carbon samples were implanted with 320 keV Xe ions at fluence ranging from 5×10^{12} to 6×10^{16} at room temperature. Our value of 29 dpa is

comparable to the maximum damage level of 25 dpa obtained at a fluence of 1×10^{16} ions/cm^2 (see-Fig 7.2) by McCulloch et al. One of the key findings in that study is that at a Xe implantation fluence of 2×10^{14} ions/cm^2 (0.2 dpa), the glassy carbon structure starts to change from a micro poly-crystalline graphite to amorphous carbon (a-C). At a damage level of 4 dpa, the glassy carbon structure was completely amorphised. The maximum damage level of 29 dpa predicted by TRIM in this study indicates that the glassy carbon structure will be amorphized after the high dose implantation of Xe. The effect of the amophisation of the glassy carbon on the diffusion of Xe is be reported in the latter part of this chapter.

The damage profile has a maximum at 90 nm and is closer to the surface compared to the implanted Xe distribution and simulated profiles. This value shows that a large number of atoms were displaced near the surface of the glassy carbon. The concentration of the damage towards the surface of the glassy carbon suggests that the diffusion of Xe is expected to be towards the surface of the GC substrate. The results obtained at low temperature annealing do not agree with this speculation.

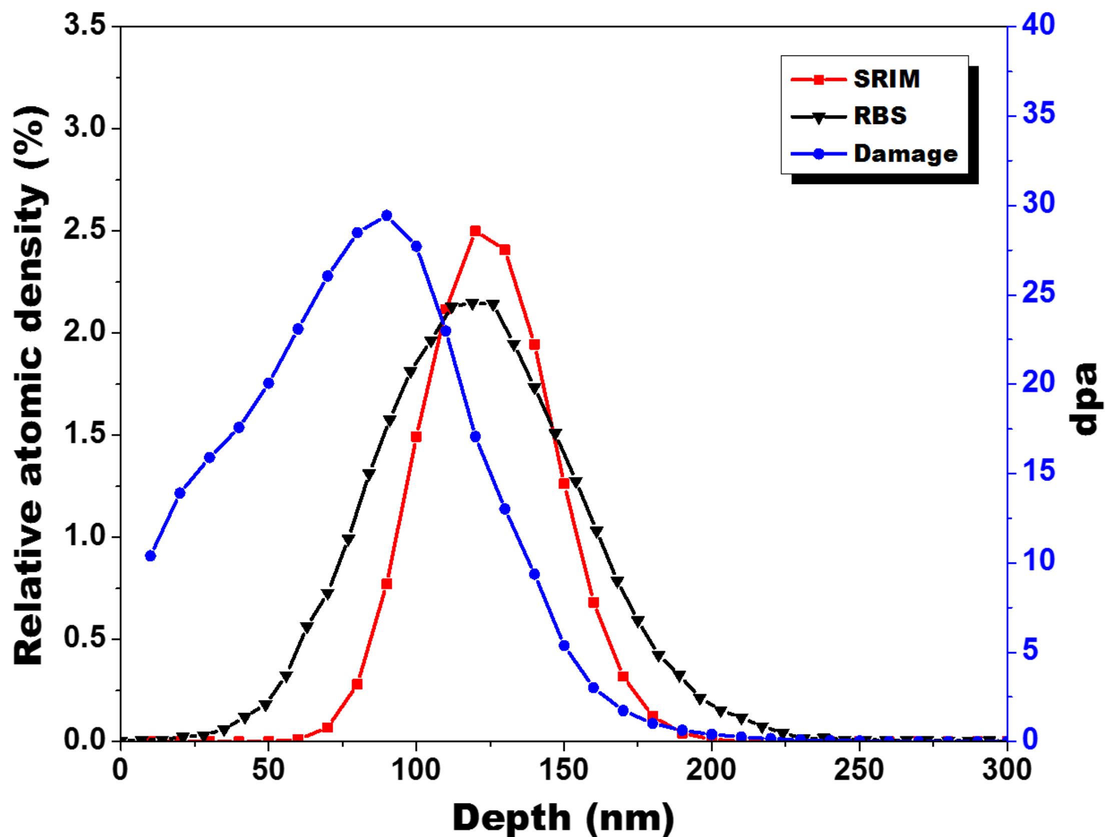

Fig. 7.1: Depth profile of 200 keV Xe^+ ions implanted in glassy carbon at room temperature compared with SRIM simulation profile. The damage in dpa is also shown using the fluence of 1×10^{16}.

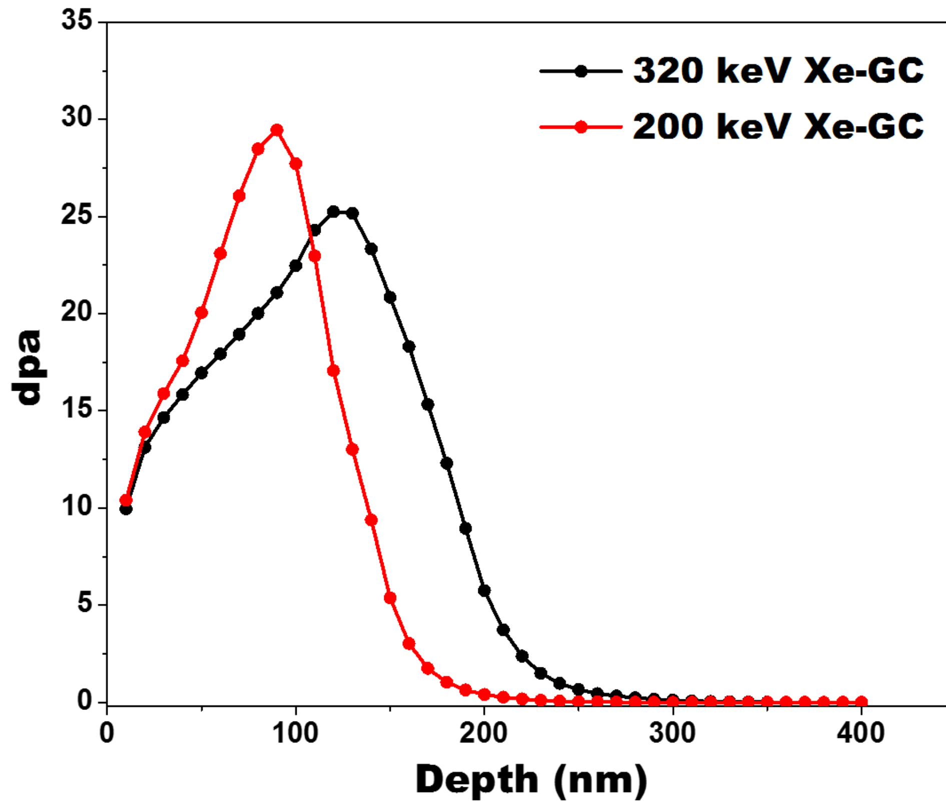

Fig. 7.2: The surface and maximum damage (dpa) of 200 keV and 320 keV Xe^+ ions implanted in glassy carbon at room temperature to a fluence of 1×10^{16} ions/cm^2.

The dpa mostly depends on the ion fluence besides the bombardment parameters such as energy of the ion bombardment. The vacancy distribution, surface and maximum damage (dpa) values are extracted depending on the fluence. At 6×10^{16} ions/cm^2 maximum damage level was 151 dpa.

7.2 Effects of thermal annealing on migration and structure of Xe implanted glassy carbon

7.2.1 RBS Results

The Xe implanted samples were sequentially annealed in a vacuum at a temperature range of 300 ^{o}C - 1400 ^{o}C in steps of 100 ^{o}C for 5 hours. The room temperature, 200 keV implanted Xe depth profiles after annealing are shown in Fig. 7.3 and 7.4. Two distinct diffusion regimes of implanted Xe were observed and the first regime was between 300 ^{o}C and 800 ^{o}C. The RBS profiles obtained after annealing the samples at these temperatures showed no noticeable diffusion or change in the peak of the implanted Xe. The xenon depth profile remained nearly the same compared to the as-implanted profile. This indicates that the lower temperature range was insufficient to cause any significant change in the implanted xenon distribution, i.e. to cause any diffusion of Xe. However, annealing at 800 ^{o}C, a slight shift in the Xe profile tail-end towards the bulk can be observed.

The RBS depth profiles obtained at these temperatures (300 ^{o}C – 800 ^{o}C) were fitted with an in-house program to obtain the projected range, R_p and the range straggling, ΔR_p [Mal17]. These values are presented in table 7.1. Together with the amount of the retained Xe ions after annealing. According to the R_p and ΔR_p values, it can be observed from the table that there was no noticeable diffusion of Xe after annealing at these temperatures. The non-diffusion of Xe at these low temperatures could be as a result of the amorphisation of the glassy carbon. The amorphisation of the glassy carbon introduced several defects and voids in the implanted region. These defects may be able to trap the implanted xenon within the implanted region.

Table 7. 1: A comparison of the range parameters obtained after fitting the RBS depth profiles at different temperatures with a Gaussian function.

Temp (° C)	R_P (nm)	ΔR_P (nm)	Retained Ions (%)
23	120.06	34.16	1.0
300	117.24	33.60	0.91
400	118.04	32.57	0.90
500	120.02	33.62	0.96
600	117.89	34.20	0.96
700	120.02	33.62	0.93
800	120.67	34.54	0.92

From Table 7.1, the average values and statistical error for the parameters: R_p, ΔR_p, and retained ion were calculated. The average values calculated and found to be 119.13 nm (R_p), 33.75 nm (ΔR_p) and 0.94 (retained ion ratio). Statistical errors, i.e. standard deviations, were calculated to be 1.36 nm for the R_p, 0.63 nm for the ΔR_p and 0.035 for the retained ion ratio. The small standard deviation of 1.36 nm in R_p that there no peak shift after annealing at this temperature range. The standard deviation of 0.0.35 nm in ΔR_p confirmed that no broadening in the implanted profile consequently no diffusion occurred up to 800 ^{o}C. No significantly changes were observed after annealing at temperature range 300 ^{o}C – 800 ^{o}C except random errors. Thus, R_p and ΔRp are independent of temperature (300 ^{o}C – 800 ^{o}C). However, the 800 ^{o}C profile showed a slight indication of Xe ions starting to migrate towards the bulk.

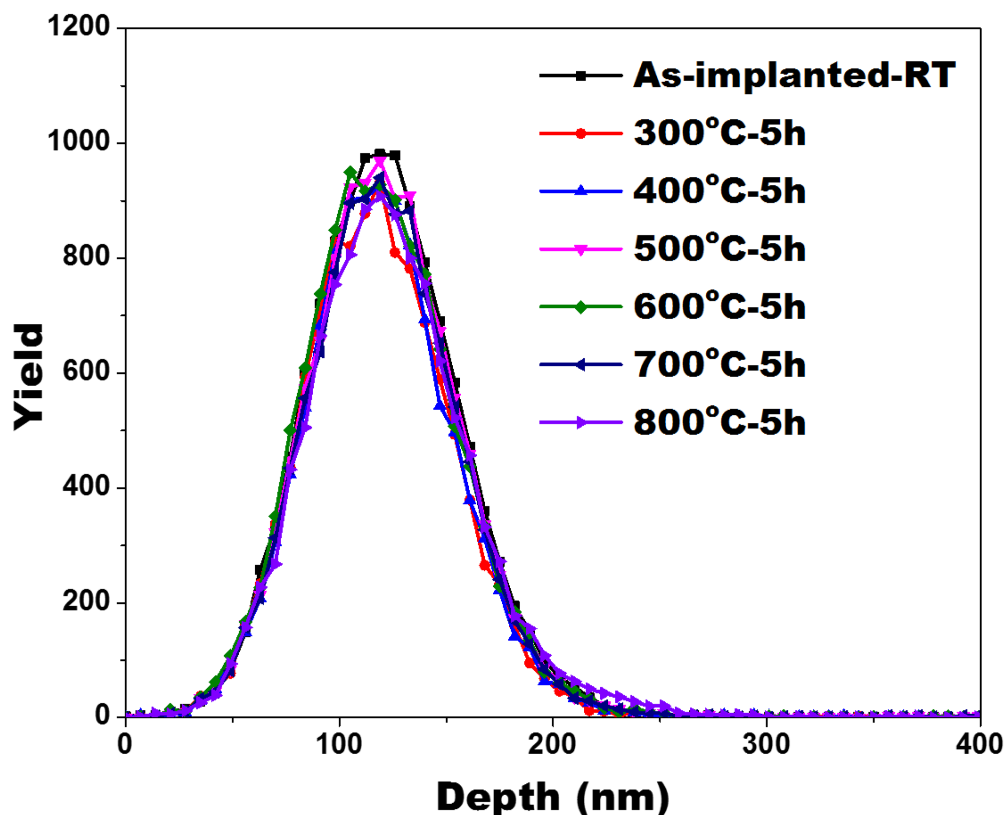

Fig. 7.3: Xe depth profiles showing the effect of sequential at low temperature (300 – 800 ^{o}C) annealing on the migration behaviour.

The second diffusion regime occurs between 900 ^{o}C – 1400 ^{o}C. After annealing at 900 ^{o}C, there was a slight shift of the Xe profile towards surface and also towards the bulk. This shift was

accompanied by broadening of the Xe profile indicating diffusion. The movement of Xe deeper into the bulk of the glassy carbon can be explained as follows; the damage/defects introduced in the glassy carbon is very minimal at the maximum implantation depth ($R_p + 3\Delta R_p$) compared to the near-surface region. During the annealing process at 900 ^{o}C, some of the defects introduced by Xe implantation are annealed out. One would expect that more recovery/recrystallization will take place at the end of range region where there is significantly less damage. This recovery may facilitate a movement of the implanted Xe into the bulk of the glassy carbon.

To test the above explanation, the Xe implanted glassy carbon samples were sequentially annealed at higher temperatures from 1000 ^{o}C – 1400 ^{o}C. Annealing at 1000 ^{o}C resulted in the Xe ions diffusing into the bulk of the glassy carbon with the formation of a bimodal distribution. This movement of Xe ions into the bulk of GC continued after further annealing at higher temperatures. One key feature observed in the depth profiles obtained at higher temperatures (shown in Figure. 7.3 (b)) is that the implanted Xe ions moved deeper into the un-implanted region of the glassy carbon. The maximum RBS-detectable depth of the implanted Xe ions after annealing at 1400 ^{o}C is about 800 nm (see-Fig. 7.3). This is significantly higher than the initial implantation thickness of 220 nm (see-Fig. 7.1). Glassy carbon is known to have a very low density (1.42 g/cm^3). The low density of glassy carbon indicates that it must contain several pores. It has been suggested that glassy carbon contains several small pores with sizes estimated to be in the order of 0.3 nm [Pie93]. The pores size mostly depends on the temperature of preparation, e.g. GC (Sigradur G) prepared at temperature of 2800 ^{o}C [Kip64]. It is possible that the implanted Xe ions may become trapped in the pores present in the GC bulk.

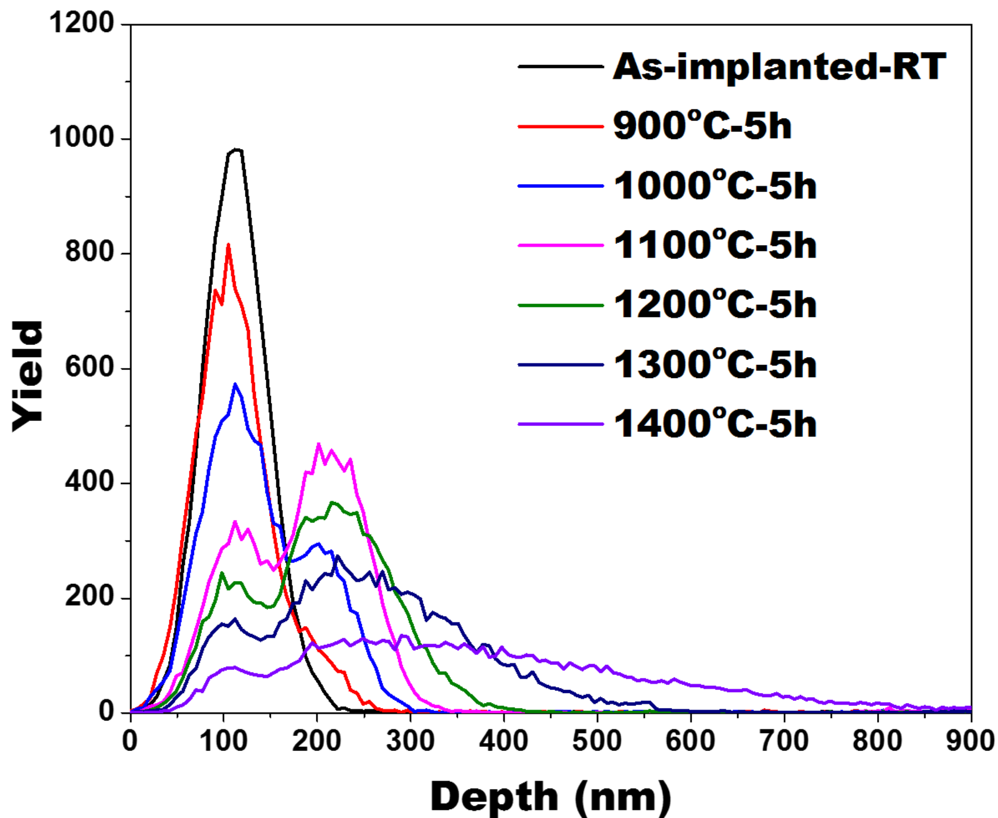

Fig. 7. 4: Xe depth profiles showing the effect of sequential at high temperature (900 – 1400 °C) annealing on the migration behaviour.

Figure. 7.5 shows the retained ratios of Xe after further annealing (900 – 1400 °C) were calculated as the ratio of the area of Xe counts after annealing to that of the as-implanted at RT. The retained Xe in a region with high radiation damage decreases gradually with increasing the temperature, then increases in a low damage region. Annealing at 1400 °C showed that only 24 % of a Xe retained within the damaged region of the GC (trapped). These results and the results in Figure. 7.4 show the migration of Xe ions towards the bulk of the GC (where the less\un-damaged region). This type of diffusion in the less damaged region might be also explained in terms of trapping and de-trapping of implanted Xe in the damaged region. The migration of Xe deeper into the bulk of glassy carbon at higher temperature annealing occurs due to less damage region which is not enough to trap the implants on the implanted and un-implanted interface.

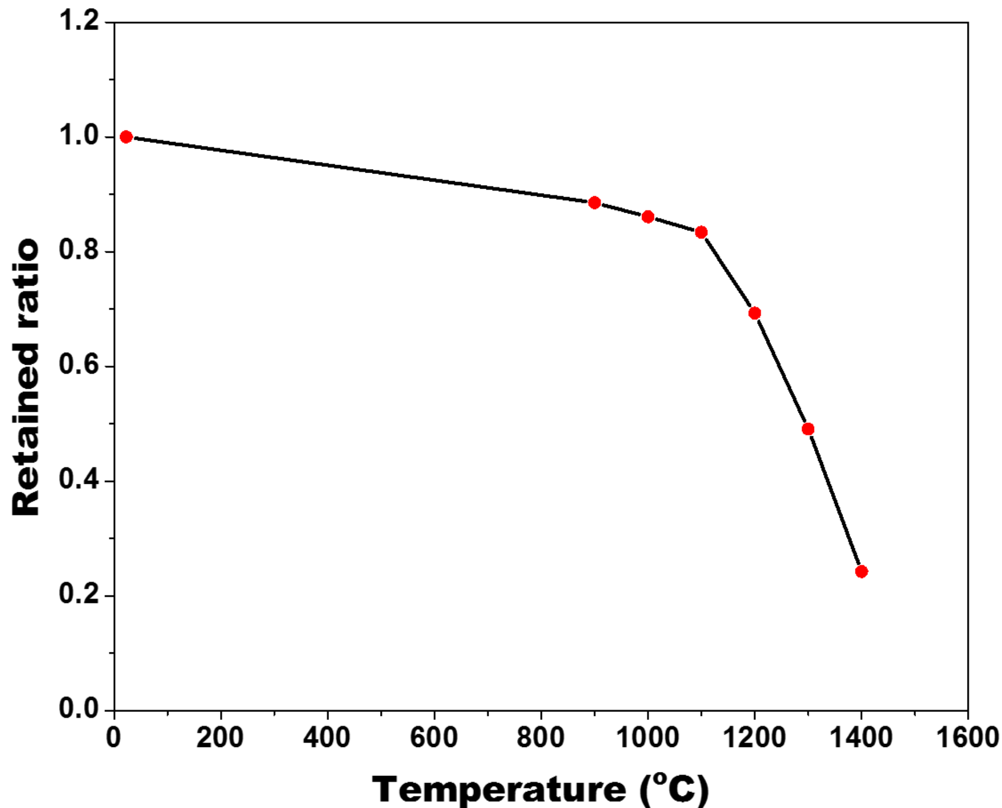

Fig. 7. 5: The amount of Xe retained within the damaged region annealed at temperature (900 - 1400 °C).

7.2.2 Raman results

Raman spectroscopy was used to investigate the structural changes and surface modification in glassy carbon as a result of implanting with Xe ions and subsequent swift heavy ion (SHI) irradiation. The Raman spectrum of virgin glassy carbon which was obtained at an excitation laser wavelength of 514.5 nm (see Figure 7.6) indicates the D and G peaks positions at about 1350 cm^{-1} and 1588 cm^{-1}, respectively. The 1588 cm^{-1} peak corresponds to the intrinsic peak of the graphite single crystal and the 1350 cm^{-1} peak is attributed to the disordered graphite structure. The spectrum also shows a hump at 1619 cm^{-1} (D′ peak), indicated by an arrow in Figure 7.6. This peak usually exists in GC with very small sized sp^2 domains. This results in a Raman doublet of the G + D′ bands which are the 1588 and 1619 cm^{-1} peaks. Additionally, there is also a small peak observed at 1093 cm^{-1}, indicated by an arrow in Figure 7.6. This peak has been attributed to the effect of the intersection of acoustic and optic modes in the density of states of graphitic carbon materials [Lav08] [Nem79].

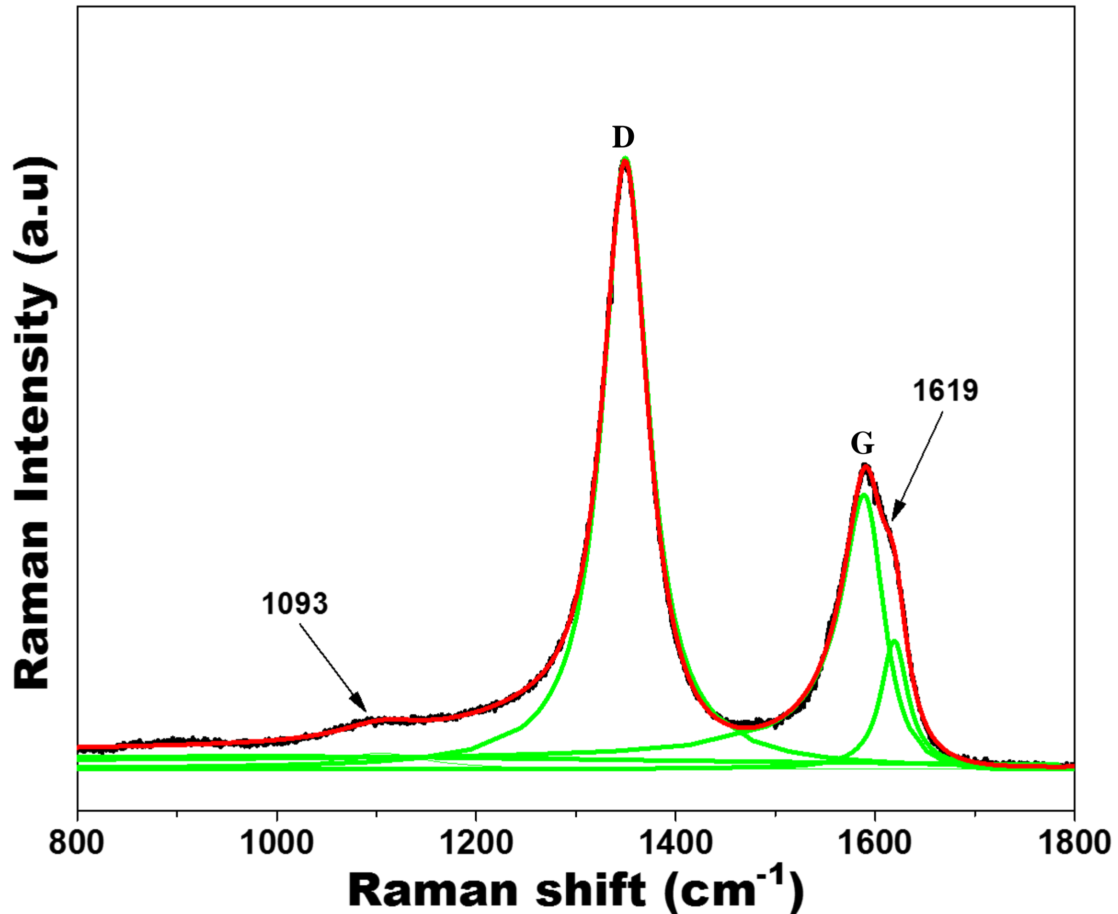

Fig. 7. 6: Raman spectrum of (virgin) glassy carbon obtained with a 514.5 nm excitation laser wavelength. The red line is the cumulative fit peak while the green lines represent the individual peak fits. The peaks indicated by arrows are discussed in the text above.

Figure 7.7 shows the effect of 200 keV Xe implantation on the structure of the glassy carbon. The Raman spectrum obtained after Xe implantation showed that the D and G peak merged into a single broad band. The spectrum is very similar to that of several amorphous forms of carbon [Sil03] [Fer00] [Yos88]. Hence, the merging of the D and G peaks indicates that room temperature implantation of Xe resulted in the amorphisation of the implanted glassy carbon area. At low annealing temperatures (500 ^{o}C – 900 ^{o}C), there was a slight re-appearance of the D and G peaks. The observed intensity of the re-grown G peak is slightly higher than that of the D peak up to 800 ^{o}C while at 900 ^{o}C are close to each other. Another important feature present in Figure 7.7 is that the G peak broadened with different treatment. After Xe implantation, the G peak position is at about 1530 cm^{-1}. This peak shifted to 1569 cm^{-1} after annealing at 500 ^{o}C and reaching a maximum of 1586 cm^{-1} at 900 ^{o}C. The broadening of the G

peak can be attributed to the different structural changes such as some of the sp^2 bonds converted to sp^3 that occur within the implanted region due to implantation and subsequent annealing. The G peak position is said to be particularly sensitive to the structure of the carbon material being investigated. This can be explained using the amorphisation trajectory [Fer01].

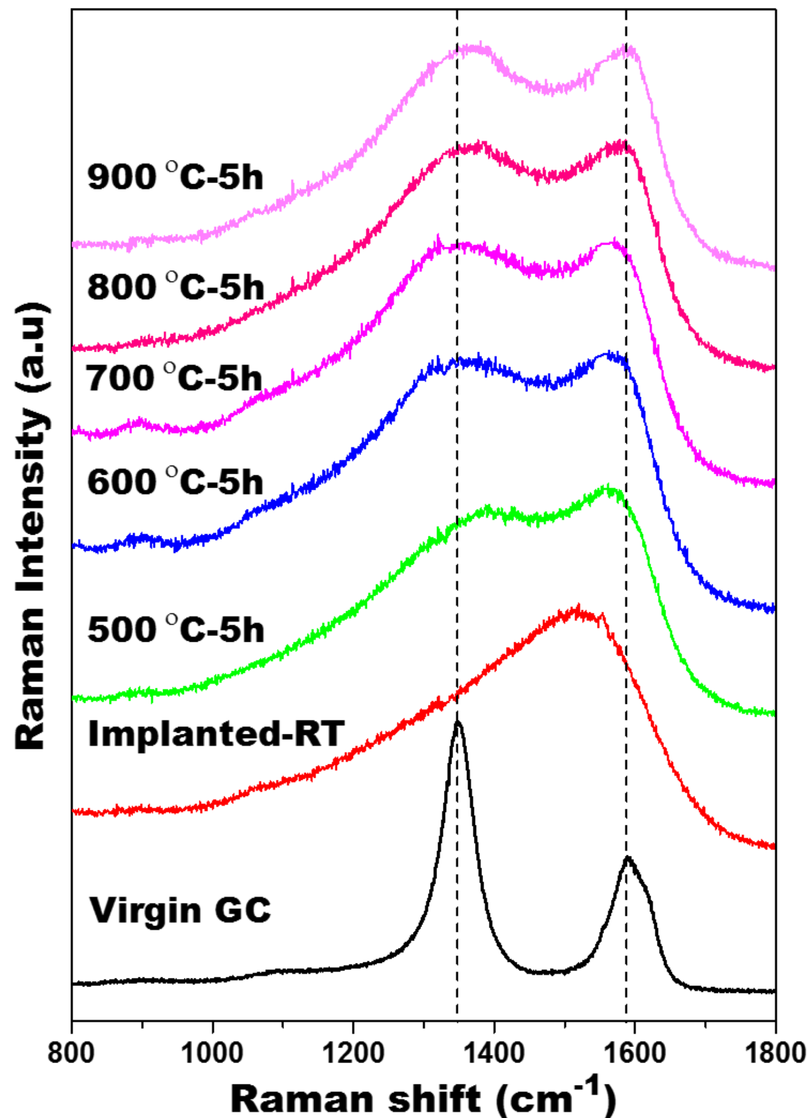

Fig. 7.7: Raman spectra of 200 keV Xe implanted GC at room temperature and the effect of sequential annealing from 500 °C to 900 °C in steps of 100 °C for 5 h, on the structure of GC. The Figure also contains the Raman spectrum for virgin GC for comparison.

The re-growth of the Raman D and G peaks was further observed after high temperature sequential annealing of the implanted glassy carbon from 1000 °C to 1500 °C as depicted in Figure 7.8. From 1000 °C to 1300 °C, the D and G peaks become even more prominent with

the intensity of the G peak increasing at a slightly higher rate than the D peak. However, at 1400 °C and 1500 °C, the intensity of the D and G peak appear to be the same. These results agree with a study carried out by Malherbe *et al*. [Mal18] when they studied the microstructure of pristine and ion bombarded glassy carbon. In their study, glassy carbon was implanted with 200 keV Sr^+ ions to a fluence of 2×10^{16} ions/cm^2 at room temperature. The implanted sample was annealed at 2000 °C for 5h in vacuum. Raman spectrum obtained after annealing showed that intensity of the G peak was significantly higher than the D peak. This is in contrast with the Raman spectrum obtained for glassy carbon – see Figure 7.6. They concluded that while there was re-crystallization of the implanted layer after the 2000 °C annealing, the resulting structure was a graphitising kind of carbon instead of the initial glassy carbon structure. This is in contrast to the pristine glassy carbon Raman spectrum which shows a more distinct D peak. A typical Raman spectrum of polycrystalline graphite shows the above-mentioned D and G peaks with the intensity of the G peak often higher than that of the D peak [Fer00]. Hence, the higher intensity of the G peak after annealing suggests that the implanted layer is being recrystallized to a graphitising type of carbon.

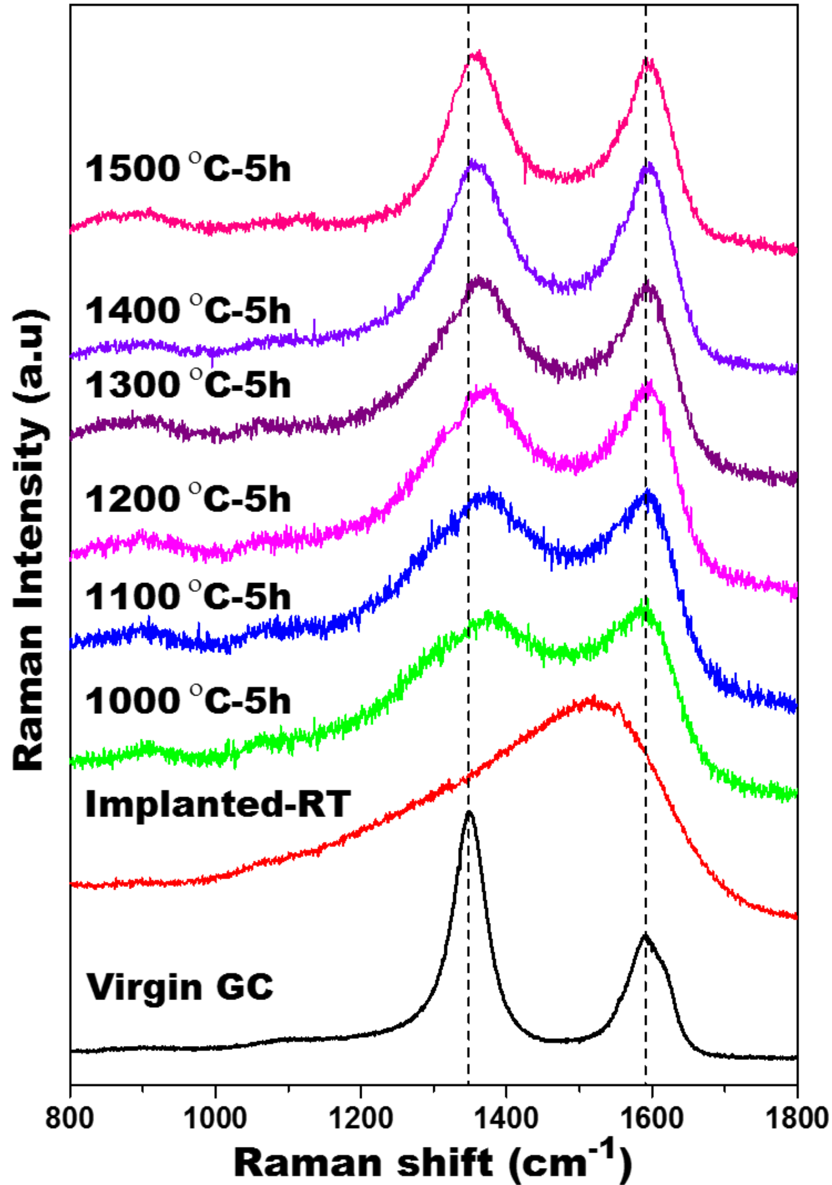

Fig. 7.8: Raman spectra of 200 keV Xe implanted GC at room temperature and the effect of sequential annealing from 1000 °C to 1500 °C in steps of 100 °C for 5 h, on the structure of GC. The Figure also contains the Raman spectrum for virgin GC for comparison.

In order to analyse the Raman spectra obtained, the baseline of the spectra lines was corrected using a linear background correction. The corrected spectra were then fitted using a Lorentzian fit for the D peak and a Breit-Wigner-Fano (BWF) fit for the G peak. The Lorentzian-BWF combination was used to fit the virgin GC spectrum, and the spectra of samples annealed at a temperature range of 500 to 1500 °C. The BWF fit was used for both the D and G peaks of the as-implanted spectrum since the Lorentzian-BWF combination could not be employed. This

was because the D and G peaks had merged into a single broad band and could no longer be distinguished from each other as seen in Figure 7.9.

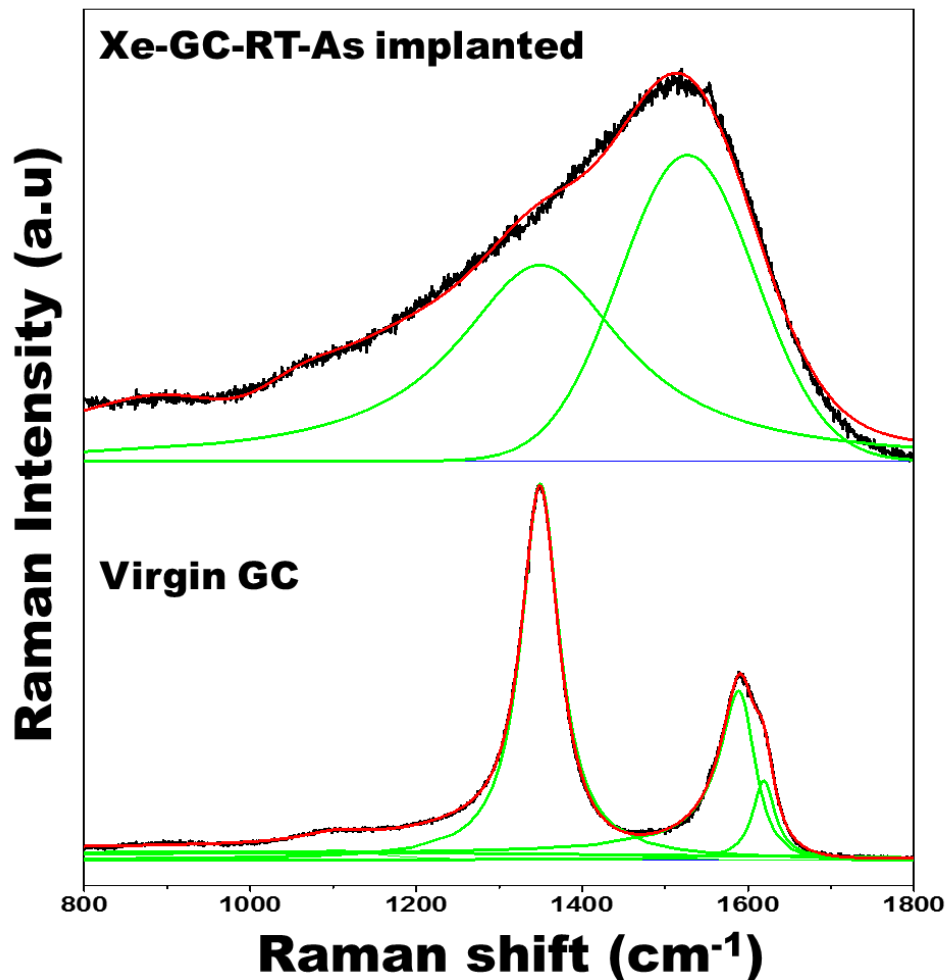

Fig. 7.9: Raman spectrum of 200 keV Xe implanted GC at room temperature. The red lines are the cumulative fit peak while the green lines represent the individual peak fit. The Figure also contains the virgin GC Raman spectrum for comparison.

The parameters such as I_D/I_G ratio (which was calculated from the D and G peak intensities), the G peak position, the G peak FWHM, and the average crystallite size (La) are tabulated in Table 7.2. The I_D/I_G ratio of the virgin glassy carbon was found to be 1.52 which is a typical value for nanocrystalline disordered sp^2 carbon materials [Pra90]. The crystallite size (La) of the virgin glassy carbon was calculated to be 2.91 nm by using Tuinstra-Koenig relation [Tui70] which holds for the sp^2 bonded carbon materials with crystallite size in the range 2.5 nm < La < 300 nm. Tuinstra-Koenig relation used to estimate the crystallite size of the virgin glassy carbon is given as:

$$\frac{I_D}{I_G} = \frac{C'_\lambda}{L_a} \qquad (7.1)$$

where C'_λ is a laser wavelength dependent constant taken as 44 Å for 514.5 nm excitation laser. Due to the fact that the bonding is still mainly sp^2, the weaker bonds soften the vibrational modes, consequently, the G peak decreases where the TK relation is no longer valid. Therefore, for small crystallite size, can be obtained using the equation [Fre00]:

$$\frac{I_D}{I_G} = C_\lambda L_a^2 \qquad (7.2)$$

where C_λ is constant which is equal to 0.0055 Å^{-2}. The I_D/I_G ratio after RT implantation was found to have reduced as expected from the pristine value to 0.35. This confirms that Xe ions implantation leads to more damage and a highly disordered region which has a reduced crystallite size. After ion implantation, the D peak position shifted from 1350 cm^{-1} to 1364 cm^{-1} while the G peak reduced to a lower wavenumber from 1588 cm-1 to 1530 cm^{-1}. The reduction of the intensity ratio and the downshift of the G peak after implantation are as a result of an increase in the amount of disorder and an increase in the sp^3 content and/or bond-angle distortion [Sai02].

Table 7.2: The Raman spectroscopy results of the 200 keV Xe implanted GC at room temperature and annealed up to 1500 °C compared to the virgin glassy carbon. The quantitative values were acquired by fitting using a Lorentzian fit for the D peak and a Breit-Wigner-Fano (BWF) fit for the G peak.

Temp (°C)	**I_D/I_G**	**G peak position (cm^{-1})**	**G peak FWHM**	**L_a (nm)**
Virgin GC	1.52	1588	25.9	2.91
RT	0.35	1530	105	0.76
500	0.40	1569	80.0	0.84
600	0.49	1569	76.8	0.92
700	0.66	1573	73.3	1.10
800	0.69	1580	69.7	1.11
900	0.75	1586	64. 8	1.16
1000	0.76	1590	60.2	1.17
1100	0.87	1593	55.7	1.25

1200	0.94	1594	51.8	1.30
1300	0.96	1595	49.4	1.32
1400	0.97	1596	43.5	1.33
1500	1.02	1596	43.4	1.36

Equation (7.2) was also used to estimate the crystallite size, L_a after annealing at high temperatures. From table 7.2, the crystallite size of the glassy carbon after ion implantation is dependent on the annealing temperature and was observed to increase with increase in annealing temperature. At the highest annealing temperature, (1500 °C), the L_a of the implanted glassy carbon increased from 0.76 to 1.36. While this value is smaller than that of the pristine glassy carbon, it still indicates that annealing resulted in the re-crystallization of the implanted region. Based on crystal growth theory [Che83], it is expected that the L_a value will increase considerably at very high annealing temperatures.

The structural changes in glassy carbon due to Xe implantation was investigated by McCulloch et al. In their study, 320 keV Xe ions were implanted in glassy carbon to fluences between 5×10^{12} to 6×10^{16} ions/cm^2 at room temperature. One of their key findings is that at fluence of 2×10^{14} Xe/cm^2 ($\approx$ 0.2 dpa), there was a significant structural change to the glassy carbon. At this point, the graphitic ribbon bonds in glassy carbon begin to break up resulting in an amorphous structure within the implanted layer. At the highest implantation fluence, 6×10^{16} ions/cm^2 which corresponds to 4 dpa, a downshift of the G peak position and a higher FWHM value was obtained. This indicates that the glassy carbon was completely amorphised by the high fluence implantation of Xe. Using electron energy-loss spectroscopy (EELS), they estimated that about 15% of the sp^2 bonds present was converted to sp^3 [Ber98].

The plot of the G peak position as a function of annealing temperature is shown in Figure 7.10. The G peak position shifted to lower wavenumber after xenon ion bombardment. Annealing from 1000 °C to 1500 °C resulted in a slight increase in the G peak position as seen in Figure 7.10. After annealing at 1500 °C, is can be observed that the G peak shifted by 8 cm^{-1} higher than that one of the virgin sample as can be seen table 7.2. The shift to higher wavenumber indicates the presence of the compressive stress in bonds between atoms as a result of a change in atomic distances [Wen12]. Although, the recovery of the G peak position after heat treatment at high temperature is observed, it differs from that of the pristine glassy carbon. This difference

indicates that some of the damage introduced by ion bombardment was retained even after heat treatment at high temperature.

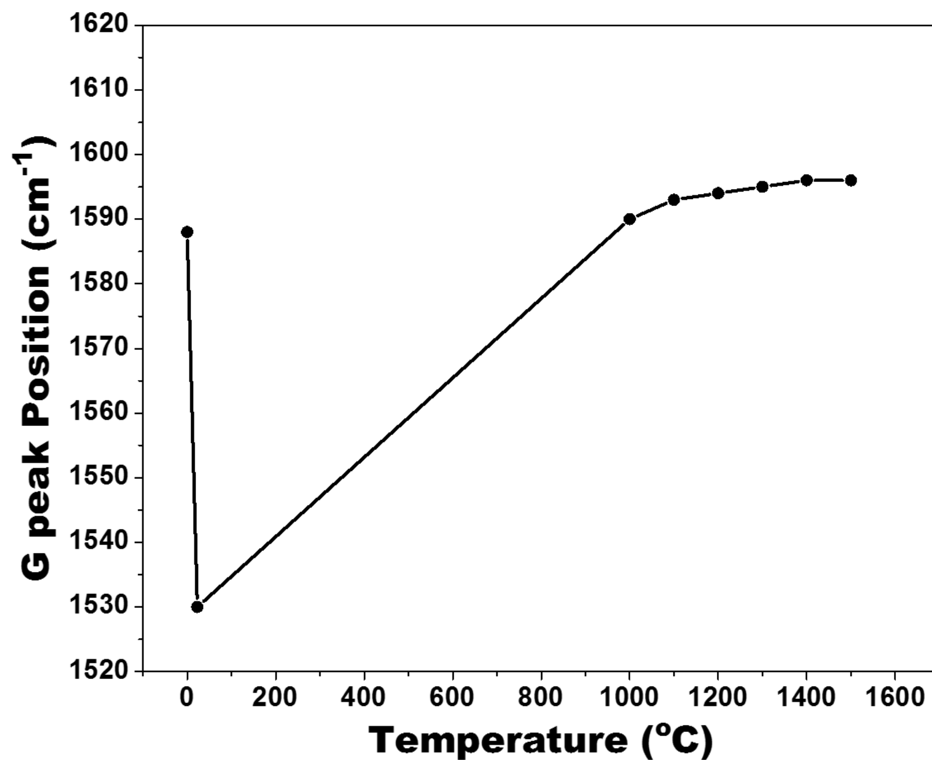

Fig. 7.10: The G peak position of the acquired spectra before and after Xe ions bombardment and heat treatment. The position of virgin GC is shown at 0 °C while the big drop at 23 °C represents the G peak position after xenon bombardment in the GC substrate.

The variation in the FWHM of the G peak after annealing at different temperatures is shown in Figure 7.11. The FWHM value increased after the RT xenon ion bombardment. The G peak broadened from about 25.9 cm $^{-1}$ for the virgin GC to 105 cm^{-1} after the Xe implantation to fluence of 1×10^{16} ions/cm^2. This broadening is due to the introduction of disorder (point defects such as C interstitials and vacancies) within the graphite-like planes of the GC structure.

Annealing at temperatures ranging from 1000 °C to 1500 °C showed a decrease in the FWHM values. The FWHM value obtained at the highest annealing temperature (1500 °C) is 43.4 cm^{-1} which still higher than that of the virgin GC (25.9 cm^{-1}). This is further proof that annealing did not completely remove all the damage introduced by the xenon ion bombardment [Mal18]. The FWHM values obtained in the present study can be compared to the results obtained by

Odutemowo *et al.* [Odu18], who studied the structural and surface changes in glassy carbon due to strontium implantation and heat treatment. They used multi-wavelength Raman spectroscopy, which included visible light laser excitation (514.5 nm (green) wavelength). They concluded that the FWHM values increased after strontium ion bombardment which led to higher level of disorder in the graphite lattice. Also, annealing of the sample at 300 °C, 600 °C and 900 °C resulted in narrower Raman spectra, hence, a decrease in the FWHM values. However, the FWHM values obtained after annealing were still higher than that of the pristine glassy carbon even at the highest annealing temperature (1500 °C).

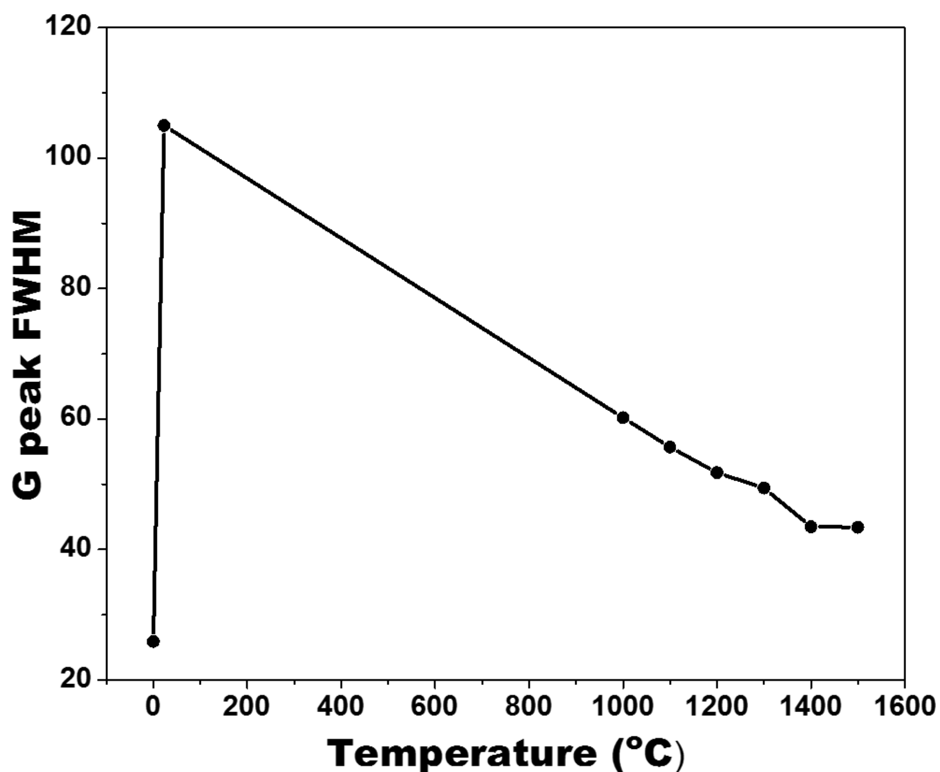

Fig. 7.11: The effect of xenon ion bombardment and heat treatment on the FWHM values of the G peak acquired after fitting the spectra with the BWF function. The increase in the FWHM values compared to the virgin glassy carbon shows the effect of amorphisation of the GC substrate after ion bombardment and heat treatment.

From table 7.2, it can be deduced that there is only slight annealing of radiation damage after heat treatment which is confirmed by the plot of I_D/I_G intensity ratio in Figure 7.12. Annealing at 1500 °C increased the I_D/I_G ratio to 1.02 ± 0.1 which is still lower than that of the virgin GC

value of 1.52 ± 0.1. The increase in the I_D/I_G ratio between 1000 and 1500 °C indicating partial recovery of the GC structure.

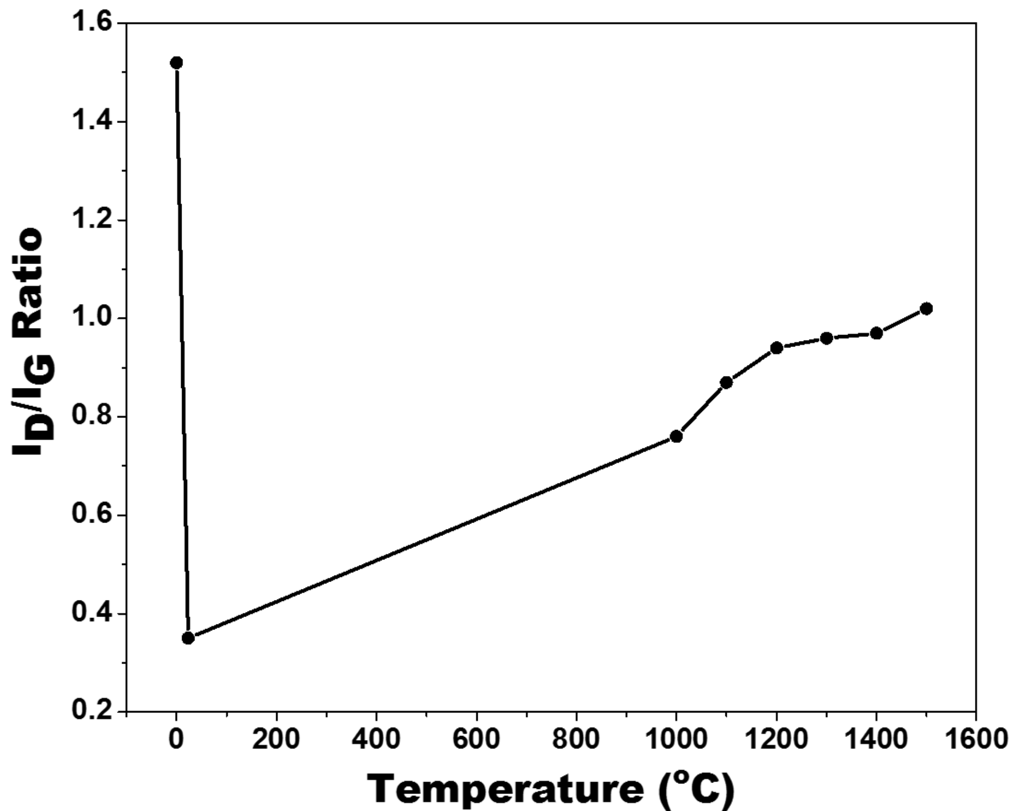

Fig. 7.12: I_D/I_G ratios of virgin glassy carbon, after RT xenon ion bombardment compared with after heat treatment of implanted GC.

To find out whether the virgin glassy carbon beyond the damaged region was also analysed during the experiment, the penetration depth of the green laser (λ = 514.5nm) was calculated using the equation (7.3) [Ni08].

$$\frac{I}{I_o} = e^{-\alpha z} \quad (7.3)$$

where I_o is intensity of incident light, I is intensity of reflected light, I/I_o is correspond the I_D/I_G ratio of the virgin GC spectrum, α is the absorption coefficient which is equal to $4\pi k/\lambda$, k is extinction coefficient of glassy carbon 0.69 for laser wavelength of 514.5 nm [Dul84], and z is the penetration depth.

$$z = \frac{1}{\alpha} = \frac{\lambda}{4\pi k} \tag{7.4}$$

The penetration depth of the 514.5 nm laser in glassy carbon was calculated to be 59.4 nm. The thickness of the implanted layer is about 222 nm ($R_p + 3\Delta R_p$). This implies that the area being probed by the laser during measurement is within the implanted layer and the bulk glassy carbon has no effect on the acquired Raman spectra.

7.2.3 Surface microstructure analysis using AFM and SEM analysis

Changes in surface morphology of a substrate often occur due to sputtering caused by the ion bombardment. The phenomena are of a statistical nature due to sputtering events, described by the sequential layer sputtering (SLS) theory, to be the statistical distribution of areas of different sputtering yields. According to the SLS theory, the surface roughness is proportional to the square root of the mean sputtered depth. This model describes how the root mean square roughness (R_q) increases with the mean sputtered depth [Mar90].

The effect of xenon ions bombardment and heat treatment on the surface topography of the GC was characterized using scanning electron microscopy (SEM) complemented by atomic force microscopy (AFM). AFM was used to evaluate and quantify the effect of Xe ions bombardment and annealing temperature on the surface roughness. The roughness parameters, root mean square (R_q) and the average roughness (R_a) were obtained using the NanoScope Analysis software. R_q is used to calculate the mean surface roughness. R_q is the arithmetic mean of the squares of a set of numbers, which is the root mean square along the sampling length. While R_a is used to calculate the average deviation roughness, which is defined as the average of the absolute value along the sampling length.

Figure 7.13 shows the 2D height, deflection error and 3D AFM images obtained for the virgin GC substrate measured in 1 μm^2. The cantilever bends in response to the force exerted on the tip by the sample features. The deflection of the probe occurs due to repulsive or attractive forces between the tip and sample atoms. The AFM cantilever measures both types of forces by varying the position of the sample. At short distances, the forces are repulsive as opposed to attractive forces that are experienced at larger sample-to-probe distances. These deflections give the topography information on height deviation at the nano-scale as the probe moves over

the surface of a sample in a raster scan pattern. Most AFMs measure sample topography by recording the output of the feedback or the cantilever deflection (also known as deflection error).

The AFM images of virgin glassy carbon showed a homogeneous surface with relatively small granules. The R_q and R_a values obtained are 1.71 nm and 1.36 nm respectively indicating that the GC surface was relatively smooth and flat.

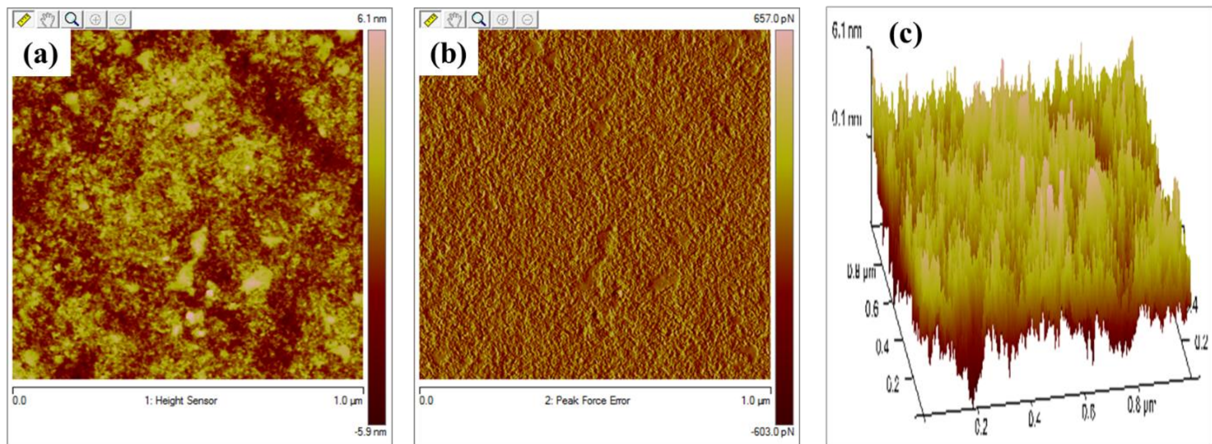

Fig. 7.13: AFM images obtained of the virgin GC substrate (a) Height image (b) deflection error (c) 3D of the height image.

The R_q and R_a surface roughness values increased to 2.54 nm and 1.97 nm respectively after the high dose Xe^+ implantation -see Figure 7.14. This indicates that the surface became rougher and with some protruding features. The increase in surface roughness after Xe ion bombardment can be attributed to the surface roughening effect of ion-induced sputtering.

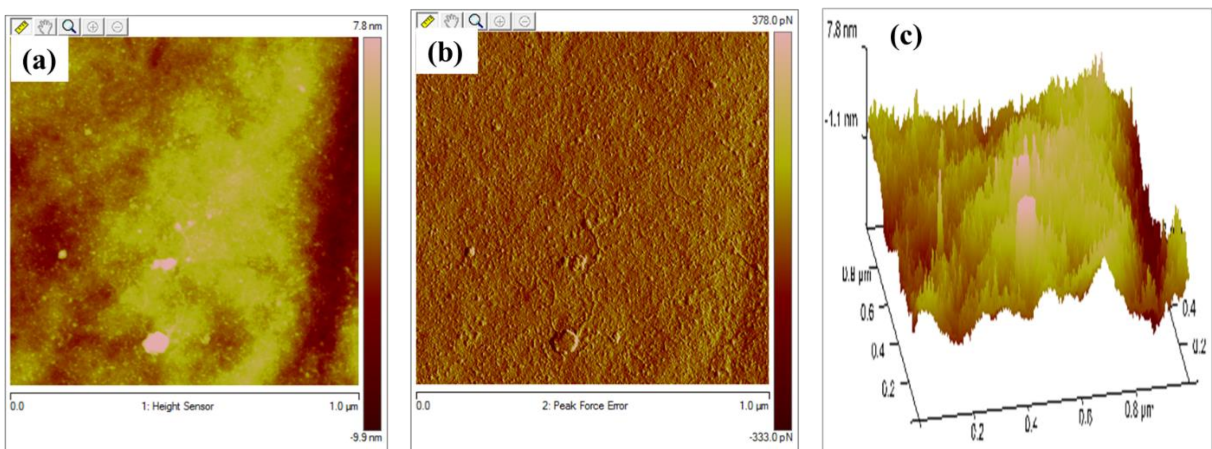

Fig. 7.14: AFM images obtained from the Xe implanted GC substrate (a) Height image (b) deflection error (c) 3D of the height image.

Figure 7.15 (a – d) show the SEM micrographs of the GC surface obtained before and after Xe implantation. The SEM images show that the polishing marks became more prominent after Xe implantation. The prominence of the polishing marks after Xe implantation is the result of the increased sputtering of the carbon atoms in the vicinity of the polishing marks. Due to the strain in the material at these scratched regions, the surface atoms have less binding energies compared to the unscratched surface regions and, consequently sputter more easily, thereby exposing the polishing lines [Ism18][Odu18].

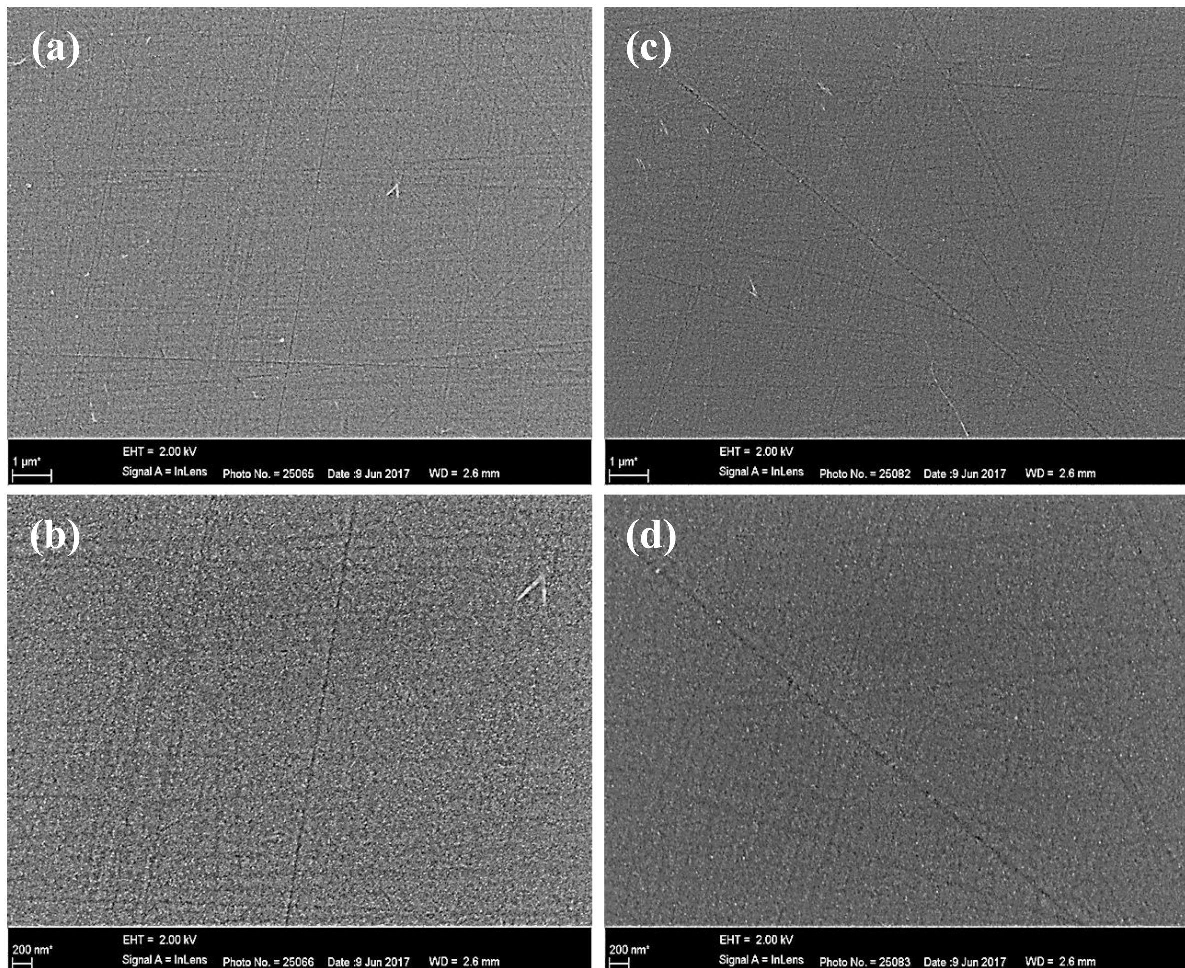

Fig. 7.15: SEM micrographs of (a) virgin GC at low magnification, (b) virgin GC at high magnification, (c) and (d) GC after Xe ion bombardment at low and high magnification respectively.

Figures 7.16 and 7.17 show the AFM and SEM images obtained after annealing the samples at 1000 °C. After annealing at 1000 °C, there was a significant decrease in the surface roughness. The R_q and the R_a values obtained were 1.36 nm and 1.1 nm respectively. The smoothening of the GC surface at this temperature is attributed to surface diffusion of the substrate atoms from the sputter roughened peaks to the valley positions. The surface of GC after annealing at 1000 °C (see- Fig. 7.16) also shows the presence of some spherical protrusions as seen in the AFM image, as well as some irregularly shaped hillocks appearing on the surface compared to the as-implanted sample.

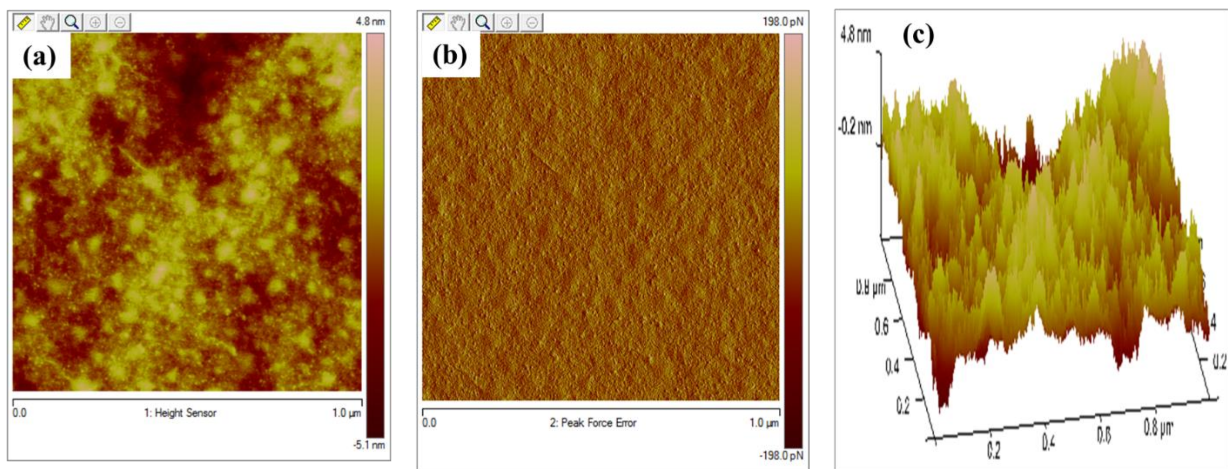

Fig. 7.16: AFM images obtained for Xe implanted GC after annealing at 1000 °C (a) Height image (b) deflection error (c) 3D of height image.

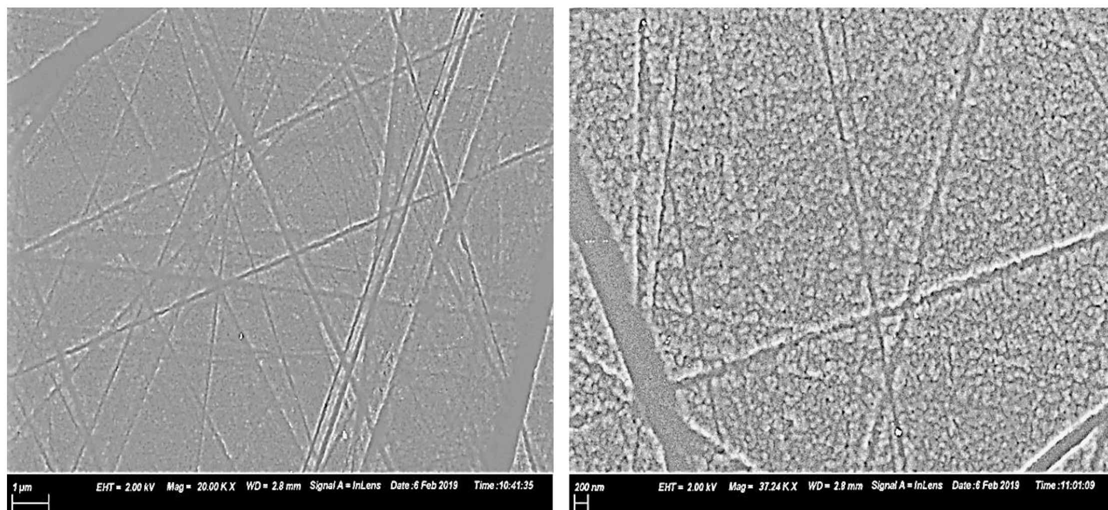

Fig. 7.17: SEM micrographs of Xe implanted GC and annealed at 1000 ^{o}C for 5h. The images were obtained at different magnifications.

After annealing at 1100 ^{o}C the surface features became more prominent, is showing island clusters and valleys as shown in Figure 7.18. It can be seen that the surface morphology after annealing at 1100 ^{o}C was different. At low magnification SEM micrographs obtained after annealing at 1100 ^{o}C in Figure 7.19, it can been seen that the granular surface structure (in regions between the scratch marks) is more prominent after annealing. This observation correlates with the AFM analysis at this temperature where larger grains were observed after annealing at 1100 ^{o}C.

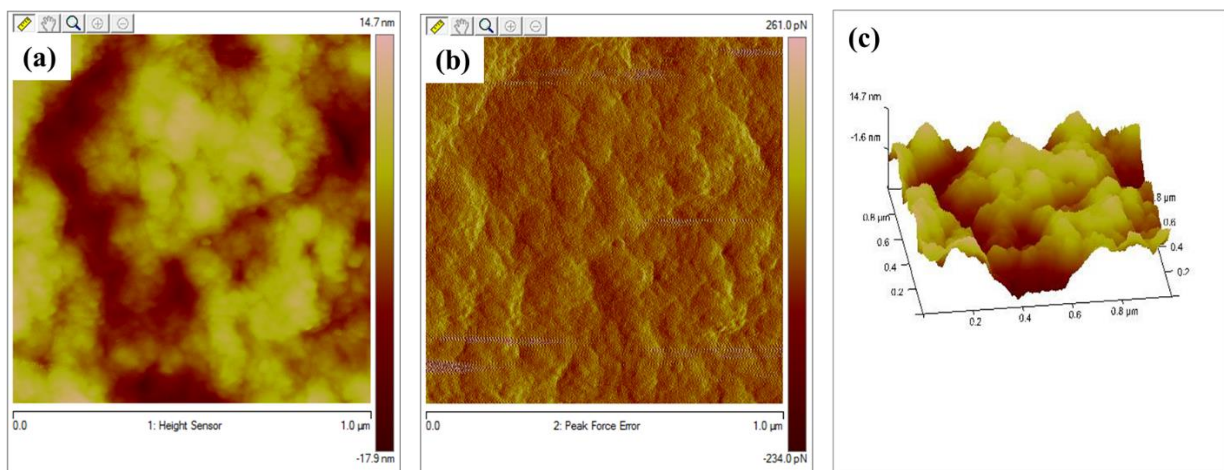

Fig. 7.18: AFM images obtained for Xe implanted GC after annealing at 1100 ^{o}C (a) Height image (b) deflection error (c) 3D of height image.

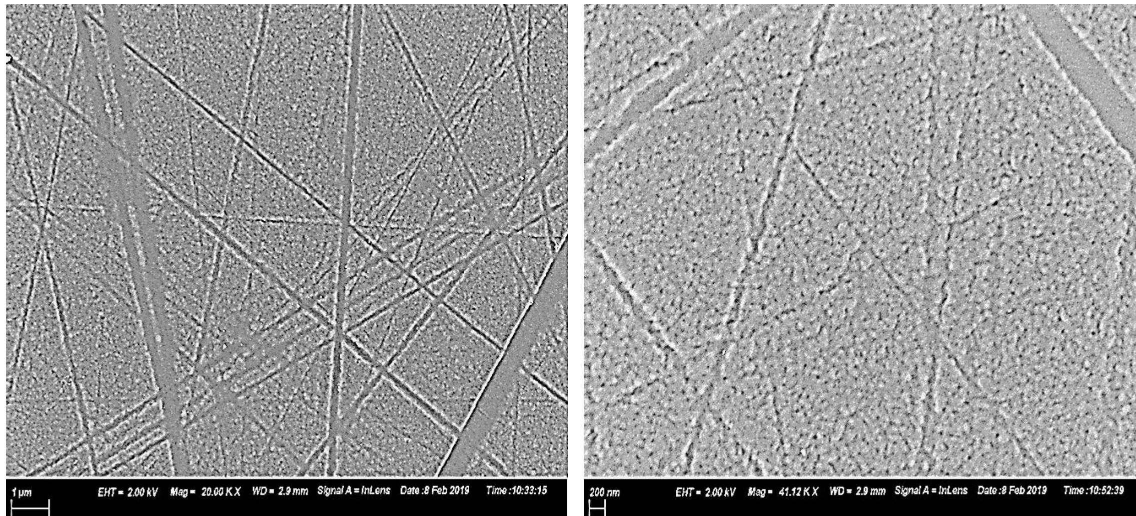

Fig. 7.19: SEM micrographs of Xe implanted GC and annealed at 1100 ^{o}C for 5h. The images were obtained at different magnifications.

However, annealing at 1500 ^{o}C (Fig. 7.20) resulted in an increase in the roughness values, which were found to be 4.12 nm and 3.21 nm respectively. The increase was result in the larger clusters after annealing at a temperature of 1500 ^{o}C. These results were also confirmed by the SEM results obtained after annealing at 1500 ^{o}C (Fig. 7.21) where it was seen that the grains grew larger and the surface became rougher compared to SEM image of 1000 °C. The brighter spots or pixels in the AFM images indicate the top of the hillocks/columns and the dark pixels indicate the valleys [Njo14]. Increase in annealing temperature, the quantity of these clusters was observed to increase. This can be attributed to the coalescing or aggregation of the surface granules into large clusters with increasing annealing temperature. The increasing cluster size was seen to influence the surface morphology, that is, with increasing size and number of clusters, the surface appears rougher. It can be deduced that the physical appearance of the surface topography strongly depends on the heat treatment.

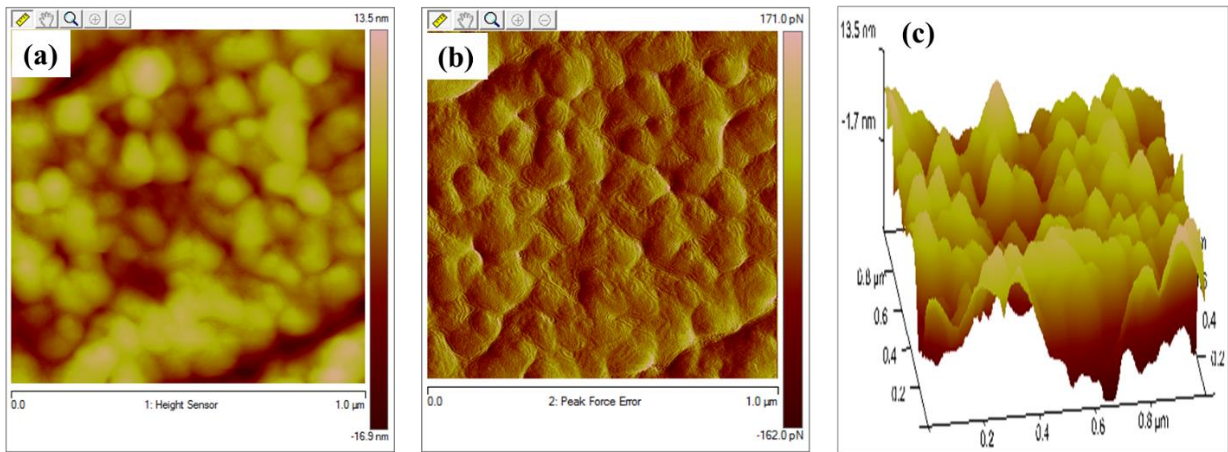

Fig. 7.20: AFM images obtained for Xe implanted GC after annealing at 1500 ^{o}C (a) Height image (b) deflection error (c) 3D of height image.

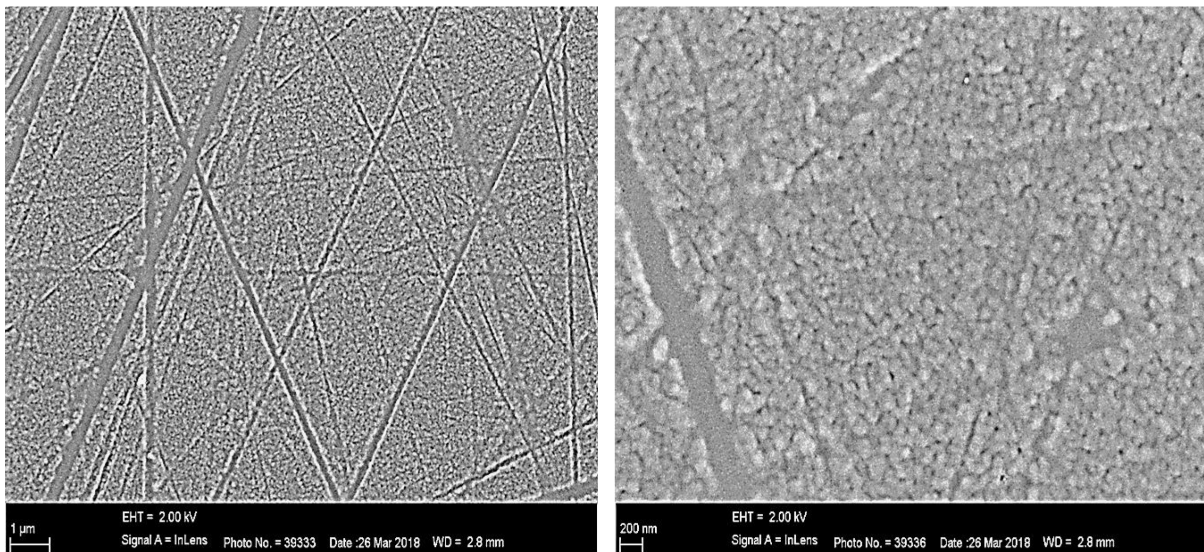

Fig. 7.21: SEM micrographs of Xe implanted GC and annealed at 1500 ^{o}C for 5h. The images were obtained at different magnifications.

7.2.4 Transmission electron microscopy (TEM) Results

The high-resolution transmission electron microscopy (HRTEM) has been extensively and successfully used for analysing crystal structures and lattice imperfections in various kinds of advanced materials at an atomic resolution scale. Recent studies have suggested that glassy carbon has a fullerene-related structure [Jur18] [Har04]. Figure 7.22 shows the HRTEM

micrograph of the pristine Sigradur® G glassy carbon cross-section. Figures 7.22 (a) and (b) show that the Sigradur® G glassy carbon consists of isotropic entanglement of layered graphitic nanostructures. The image shows that glassy carbon is a typical non-graphitizing carbon accompanied by a closed fullerene carbon nanostructure. This can be compared to an imperfect multi-layered fullerene which often surrounds pores. One of the features of glassy carbon that makes it different from other forms of non-graphitising carbon is its low reactivity and being highly impermeable to gases. This has been attributed to its higher number of closely packed microstructures and tightly curled single carbon layers [Har04] which are indicated with circle frames and the arrows in Figure 7.22 (a) and (b). The onion-like, i.e. fullerene, carbon structures were also observed - see Figures 7.22 (b) and (c).

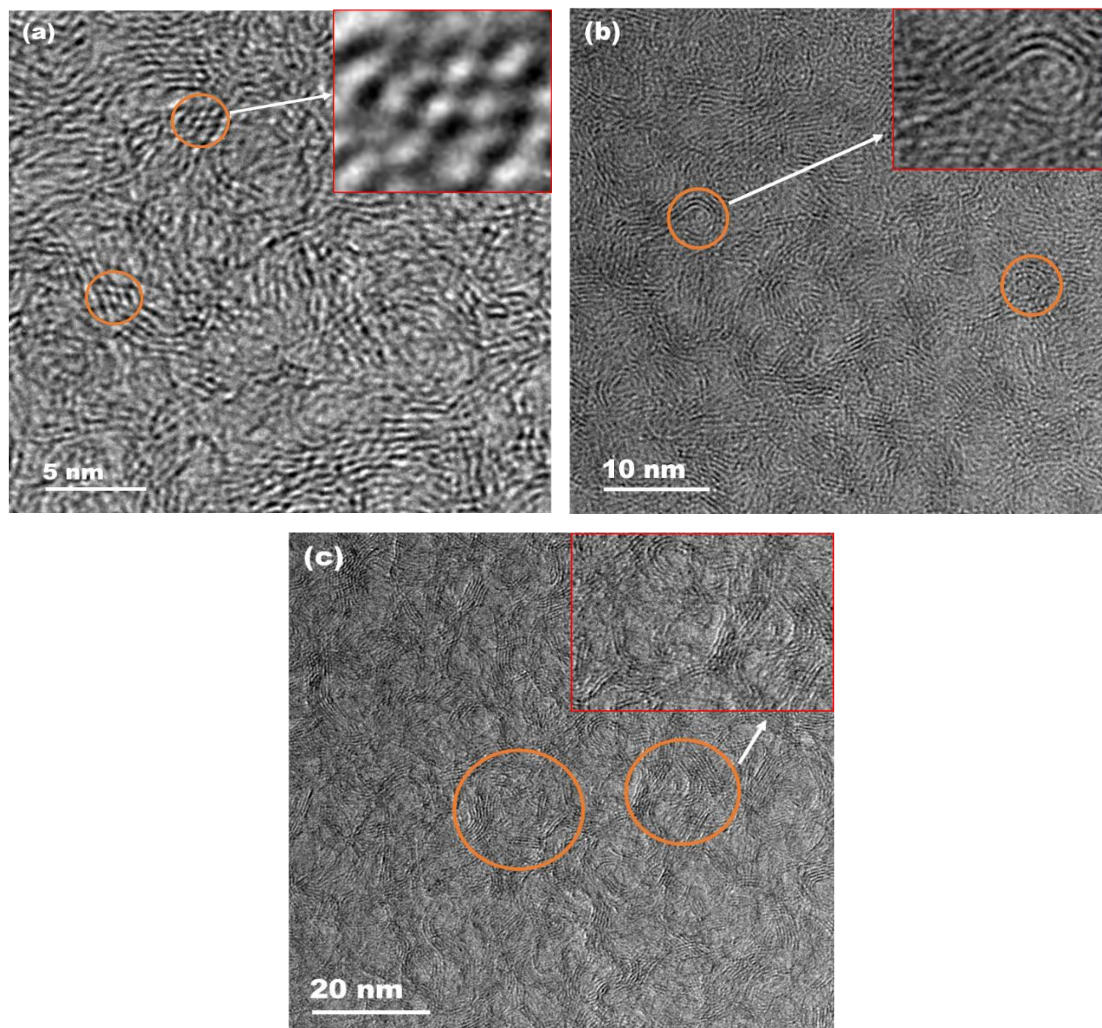

Fig. 7.22: HRTEM micrographs of virgin glassy carbon obtained at different magnifications. The onion-like structure of glassy carbon is highlighted in the brown circles in the Figures.

Figure 7.23 shows the bright field HRTEM images obtained after Xe implantation in glassy carbon. Fig. 7. 23(a) shows three distinct regions. The region; (i) is the platinum protective layer (ii) Xe implanted layer which has a thickness of 220 ± 10 nm and (iii) the bulk glassy carbon. In the bulk region several sharply contrasting areas can be seen. The dark spots indicate regions where the electron beam is diffracted, thereby indicating crystallites. The implanted region also has such dark spots but significantly less than in the bulk. This suggests that the implanted region was not 100 % amorphised but also contained some remaining graphitic crystallites. The implanted region is shown at a different magnification in Figure 7.23(b). Figures 7.23 (c) and (d) are the HRTEM images obtained towards the surface and at the end of the implanted layer respectively. Comparing the bright field HRTEM images of the implanted glassy carbon shown in Figures 7.23 (c) and (d) to that of the pristine glassy carbon (Fig. 7.22), it can be clearly seen that the structure of glassy carbon was damaged after implantation. The initial structure has been replaced by an amorphous structure. The structure of glassy carbon within the implanted layer is very similar to that of diamond like carbon (DLC). However, the amorphous structure consists of several stacks of parallel fringes. Some of these fringes are indicated in Figures 7.23 (c) and (d) with red arrows. These fringes are attributed to graphitic crystallites present within the implanted layer. McCulloch et. al. [McC94] studied the formation of preferred orientation in glassy carbon due to high fluence C^+ implantation. They found out that the implantation of 5×10^{16} C^+/cm^2 resulted in the amorphization of the implanted layer. They also found that several graphitic fringes with spacing of approximately 0.34 nm which corresponds to the (002) lattice spacing in graphite were embedded within the amorphised layer.

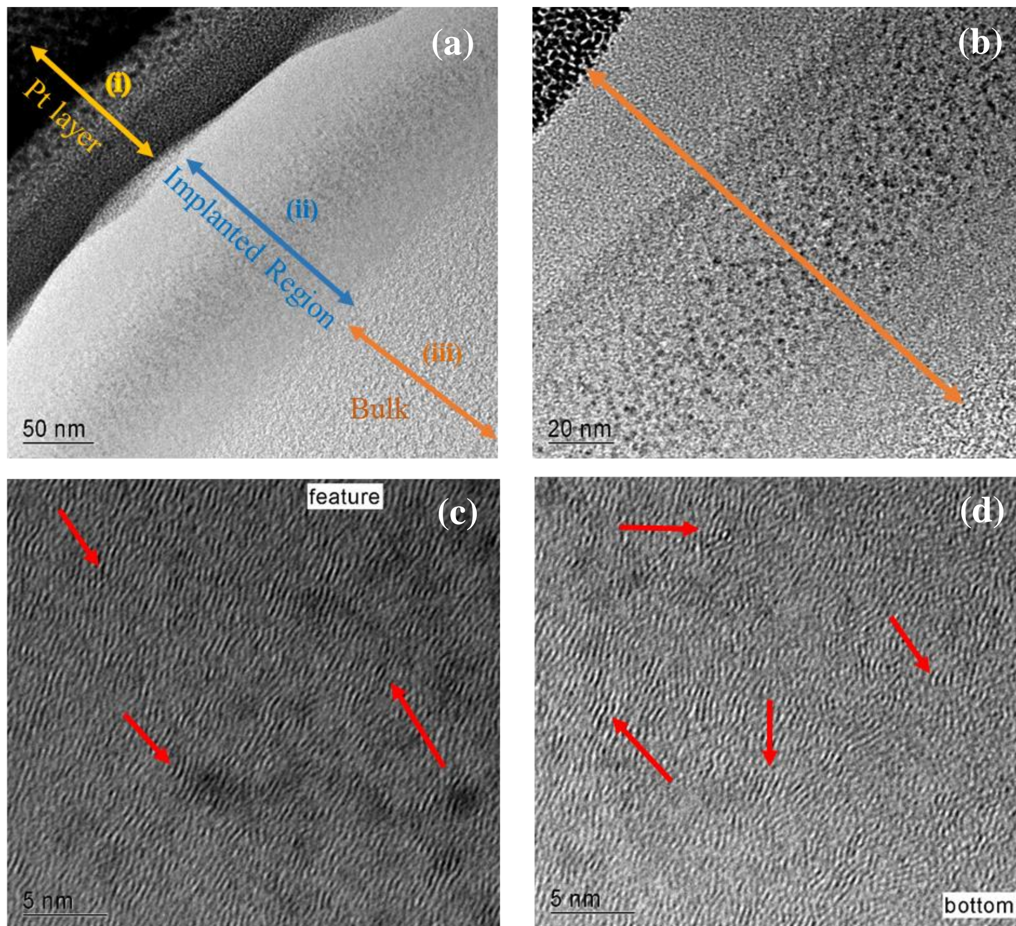

Fig. 7.23: HRTEM micrograph showing the effect of 200 keV Xe bombardment on GC taken at different magnifications. (a) is shows the contrast between the Pt protective layer, the implanted layer and the bulk of the glassy carbon. (b) – (d) are the HRTEM images obtained for the Xe implanted glassy carbon at different magnifications and positions.

The bright field HRTEM images obtained at different magnification after annealing at 600 ^{o}C are shown in Figure 7.24 below. Figure 7.24 (a) also depicts the contrast between the Pt layer, the implanted layer and the bulk of the glassy carbon sample. The implanted layer is shown at a different magnification in Fig. 7.24 (b). HRTEM images obtained near the surface and towards the end of the implanted layer are shown in Figures 7.24 (c) and (d). The graphitic fringes present within the amorphous layer are depicted by brown arrows in (c) and (d). The images shown in (c) and (d) show a very slight re-crystallization of the implanted layer. One key observation from the images is that there are some fullerene-like structures now present within the implanted layer. The Raman spectrum obtained after heat treatment at 600 ^{o}C showed the re-appearance of the Raman D and G peaks. This implies that some of the radiation

damage introduced during the implantation process has been annealed out. However, the initial glassy carbon structure was not recovered after annealing at this temperature.

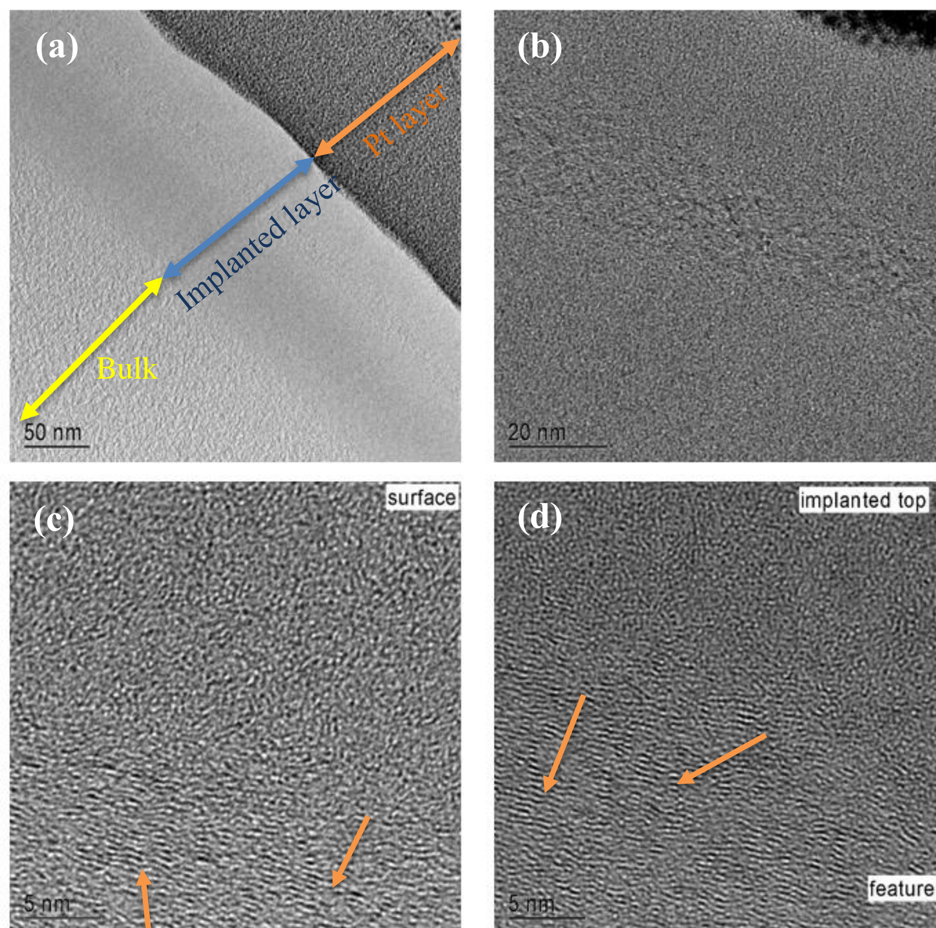

Fig. 7.24: HRTEM micrographs showing the effect of 600 °C heat treatment on the microstructure of Xe implanted glassy carbon. (a) is shows the contrast between the Pt protective layer, the implanted layer and the bulk of the glassy carbon. (b) – (d) are the HRTEM images obtained within the Xe implanted layer at different magnifications and positions after 600 °C annealing.

Figure 7.25 shows the HRTEM micrographs obtained after annealing the implanted sample at 1000 °C. Again Figure 7.25 (a) depicts the contrast between the Pt layer, the implanted layer and the bulk of the glassy carbon. These are also shown at a different magnification in Figure 7.25 (b). From Figures 7.25 (c) and (d), it can be clearly seen that the graphitic fringes embedded in the implanted layer are absent after annealing at 1000 °C. The absence of these fringes could be as a result of the re-crystallization and re-ordering of the glassy carbon

structure. However, it can be clearly seen that the glassy carbon structure was not fully re-crystallized after the high temperature heat treatment.

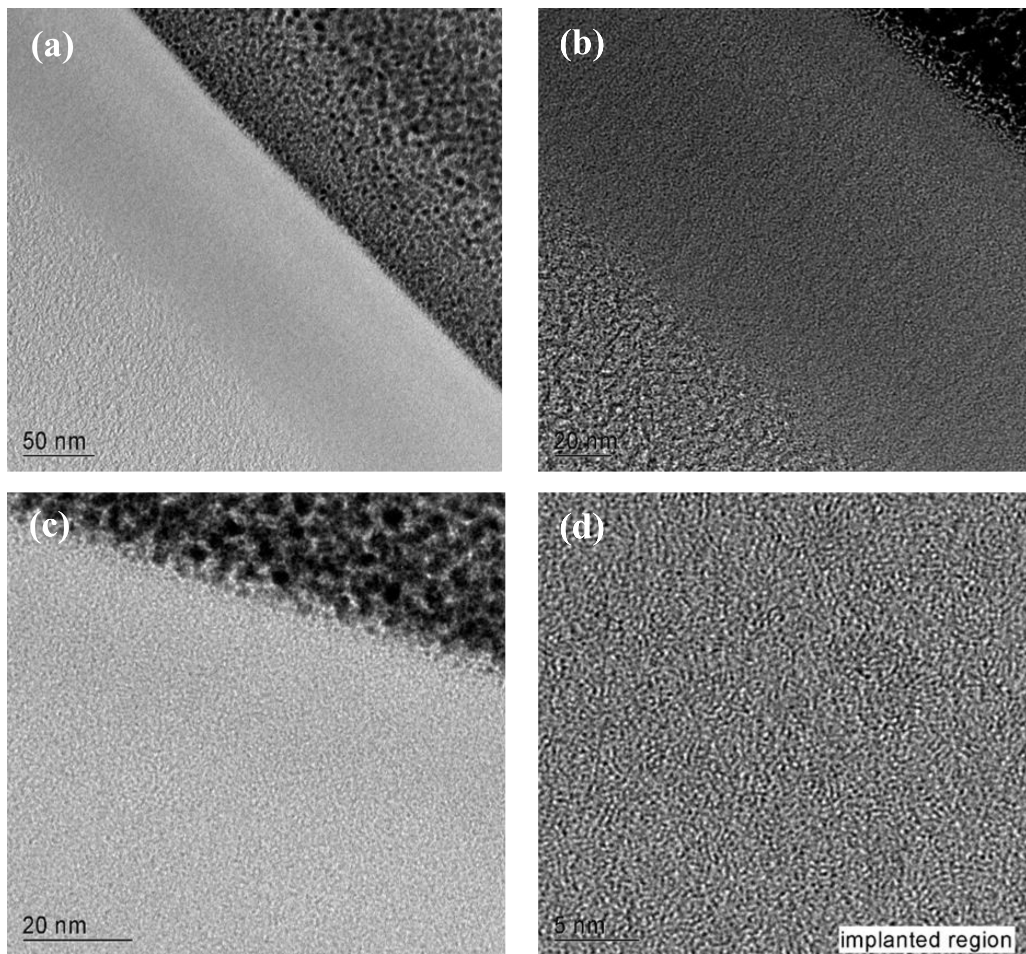

Fig. 7.25: HRTEM micrographs showing the effect of 1000 ^{o}C heat treatment on the microstructure of Xe implanted glassy carbon. (a) is shows the contrast between the Pt protective layer, the implanted layer and the bulk of the glassy carbon. (b) – (d) are the HRTEM images obtained within the Xe implanted layer at different magnifications and positions after 1000 ^{o}C annealing.

7.2.5 Densification of glassy carbon due to Xe ion bombardment

The presence of graphitic fringes in an amorphous matrix within the implanted region of the glassy carbon strongly suggests that Xe bombardment will result in an increase in the density of the GC within the implanted region. To prove this, the step height between implanted and un-implanted regions was measured using AFM – see Figure 7.26. From the step height

measurement, it was found that the implanted region was lower than the un-implanted region. The change in the height is the result of compaction of the near surface region of GC leading to an increase in the density of the implanted GC after ion bombardment. The increase in density was accompanied by change in structure of GC towards an amorphous carbon structure.

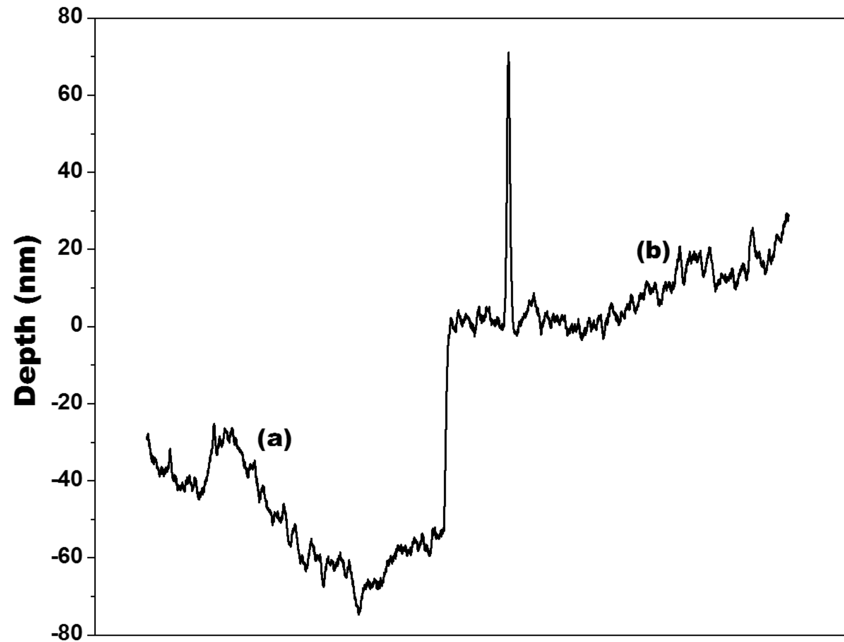

Fig. 7.26: AFM line scan measurement taken from (a) implanted region to (b) un-implanted region of glassy carbon, to obtain the step height value between the two regions.

The density of the implanted layer was calculated using the thickness of the implanted area which is approximately 153.5 nm, the density of the Sigradur® G GC (1.42 g/cm^3) and the step height (55.1 nm). The density was then calculated using the equation below [Odu18]:

$$\rho_f(g/cm^3) = \frac{\rho_{GC} \times (R_P + \Delta R_P)}{(R_P + \Delta R_P) - 55.1} \qquad (7.5)$$

The result from equation above proves that the obtained value (2.215 g/cm^3) is very similar to that of graphite which is 2.26 g/cm^3. The increase in the density of the glassy carbon is due to the amorphisation of the glassy carbon structure after Xe implantation. Several studies have been done on the densification of glassy carbon by ion bombardment [Iwa00] [Toi01]. All concluded that the ion beam bombardment of glassy carbon induces amorphisation of the surface layer which leads to the change in atomic density. The atomic density of glassy

carbon mostly depends on the structure of glassy carbon, is 1.50 g/cm^3 and increases to 2.25 g/cm^3 due to densification after ion bombardment. Therefore, it is considered that the change in structure from GC to amorphous carbon accompanies the change in atomic density. However, the cause of the observed step height could also be due to sputtering of the glassy carbon atoms during ion implantation [Toi01]. From TRIM simulations [Sri12] using a surface binding energy of 7.4 ev/atom, the sputtering yield from the GC surface caused by Xe ions implantation was found to be 1.94 atoms/ion. Then using density of 1.42 g/cm^3, the thickness of the sputtered layer was found to be 2.73 nm. This value is essentially too low to be solely responsible for the height difference between the virgin and implanted glassy carbon.

7.3 Effects of SHI irradiation on migration and structure of Xe implanted glassy carbon

7.3.1 Swift heavy ion (SHI) irradiation

A nuclear waste storage container must be able to contain the fission products which are released with different energies. During the fission process in nuclear reactors, nuclides with a large range of energies from hundreds of MeV to few GeV are released. The energy in the order of 100 MeV, is the energy range of swift heavy ions (SHIs). Since glassy carbon (GC) is used in nuclear reactors and considered as an alternative material for nuclear waste storage of high-level nuclear waste (HLW), hence, GC from such a container will be exposed to radioactive nuclei of different energy range i.e. from few keV to 100 MeV.

When SHI passes through the target material, it produces electronic excitation of the atoms in the material. These processes occur when high energy particles are slowed down in the material due to transfer its energy to the electrons of target materials. The modification of the material can be occurred within a cylindrical zone along the ion trajectory, so-called latent track or ion track (damage zone created along the paths of swift heavy ions) is shown in Figure 7.27.
The SRIM simulation [Sri12] shown in Figure 7.28, confirmed that the energy loss due to 167 MeV Xe ion in GC and xenon was predominantly via electronic excitation from inelastic collisions and not nuclear elastic collisions [Fle75] [Ava11] [Njo17]. The nuclear energy loss (Sn) usually decreases with an increase in ion energy while electronic energy loss (Se) increases. From Figure 7.28 it is clear that Se > Sn near the surface of GC with the Se and Sn values of 10.92 and 0.29 keV/nm, respectively.

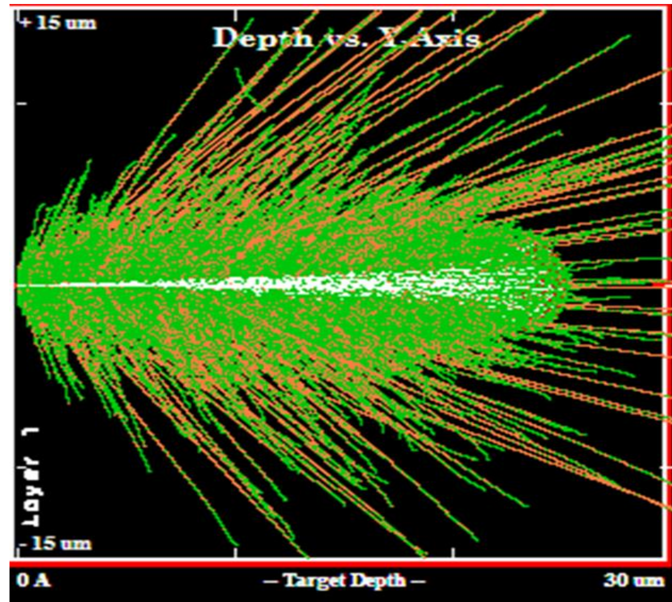

Fig. 7.27: Trajectories produced by 167 MeV Xe ion (white in colour) in GC along with the recoils (represented by green colour) [Sri12].

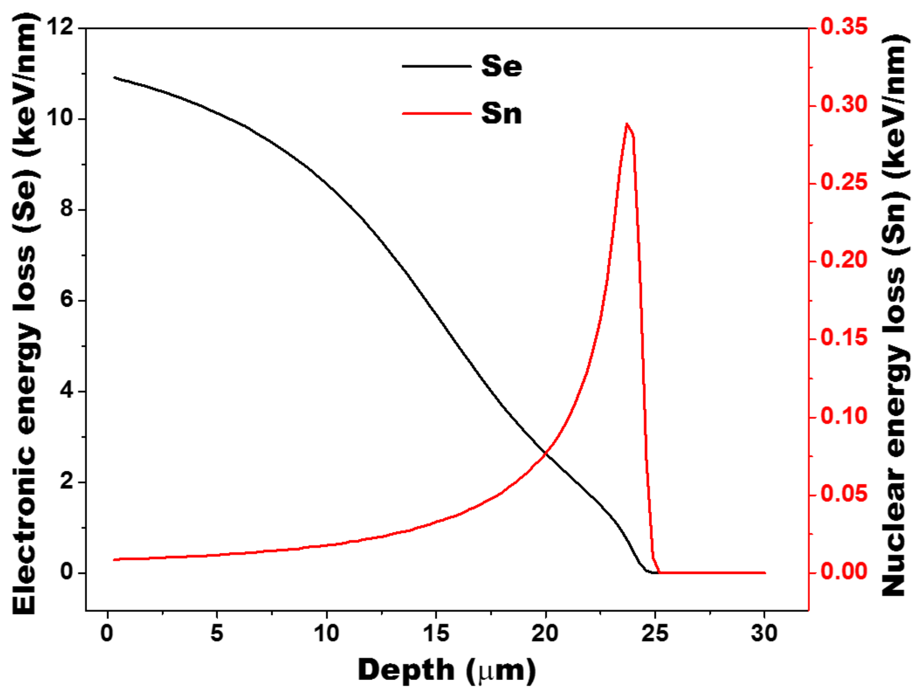

Fig. 7.28: The energy loss of electronic (inelastic) and nuclear (elastic) collisions by Xe ion in GC, at the energy of 167 MeV [Sri12].

7.3.2 RBS results

The RBS spectra of RT implanted GC and the sample irradiated with 167 MeV Xe SHIs to a fluence of 1×10^{14} ions/cm^2 are shown in Figure 7.29. There was a slight shift of Xe ions toward the bulk after SHI irradiation compared to the un-irradiated GC sample. It is well known that transient heating effects (thermal spikes) occur when energetic swift heavy ions (SHIs) deposit their energy to surrounding the ion track via ionization. A penetrating ion induces transient lattice heating, which may exceed the melting point of the target material [Tou92]. This especially occurs during swift heavy ion (SHI) irradiation events, where inelastic interactions with the target atoms can locally produce hot electrons with a very high temperature [Wan94]. This shift may be due to the transient melt along ion trajectory, resulted in a little amount of xenon evaporating. Several studies have concluded that SHI-induced annealing in the material, electronic energy depositions exceeding 10 keV/nm, and some as large as 30 keV/nm [Zha15]. Since $S_e >> S_n$, high electronic energy loss by the SHI beam in a very short time produces significant excitation in the crystal lattice, leading to form a transiently heated region along the track.

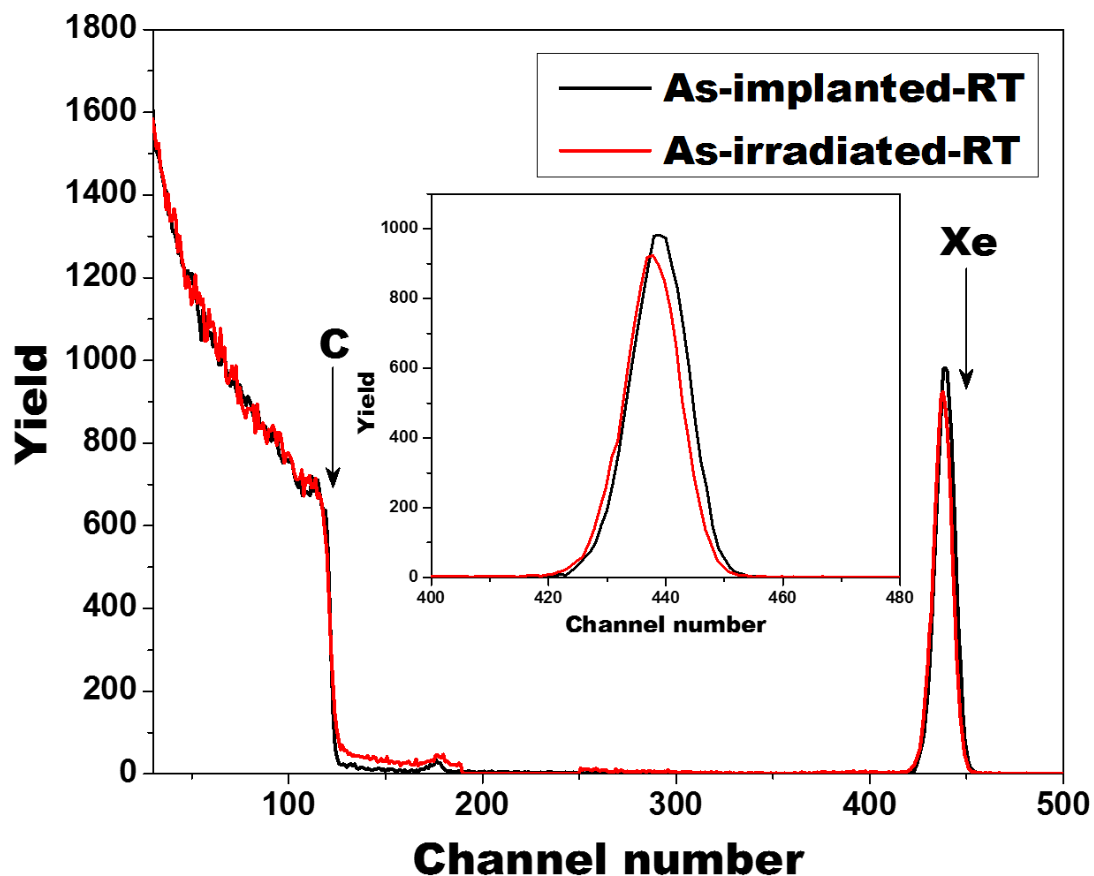

Fig. 7.29: RBS spectra comparison of 200 keV Xe^+ implanted GC, and irradiated with swift heavy ions at (167 MeV Xe^+).

The RBS depth profiles obtained after SHI irradiation and annealing in the temperature range of 1000 °C to 1400 °C in steps of 100 °C for 5 hours are shown in Figure 7.30 (b). The migration of xenon ions is still moving towards the bulk of GC which is the undamaged GC and therefore SHI irradiation does not influence the direction of xenon migration behaviour. The implanted Xe only migrated during annealing into undamaged bulk GC not towards the surface of glassy carbon region.

From Figure 7.30 (a) and (b), a comparison depth profiles between as-implanted at RT and implanted then irradiated with SHI irradiation. After annealing the SHI irradiated samples at 1000 °C, very little diffusion was observed with a single peak while the un-irradiated sample had a bimodal distribution after annealing at this temperature as seen in Figure 7.30 (b). Annealing at the SHI irradiated sample at 1100 °C, the implanted Xe profile has a bimodal distribution. The first peak nearer to the surface has a higher height than the second deeper peak while for the un-irradiated sample first peak has lower height than the second. At the temperatures range of 1200 °C to 1400 °C, the height first peaks for both RT and SHI are lower than the second peaks. The diffusion rates after annealing the un-irradiated and the SHI irradiated samples was different as seen in Figure 7.30. Higher diffusion was observed after annealing the RT from 1000 to 1500 °C. This is due to the different structures retained in the GC after RT Xe implantation (un-irradiated) and after SHI irradiation. The sample irradiated with SHIs was observed to have some slight recovery within the implantation damaged region of the GC.

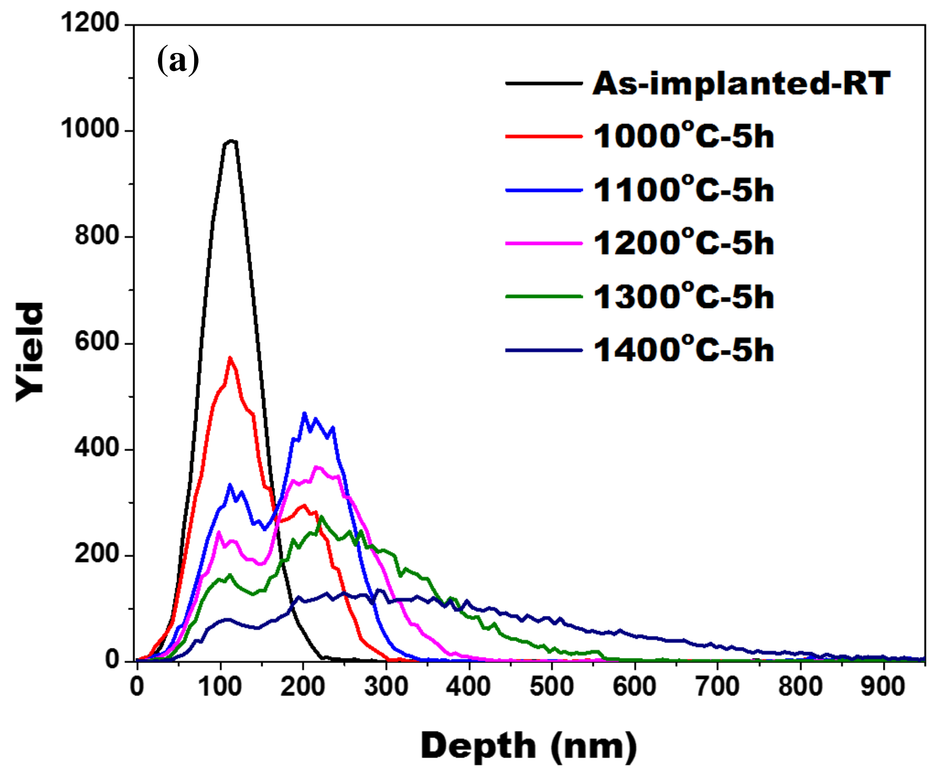

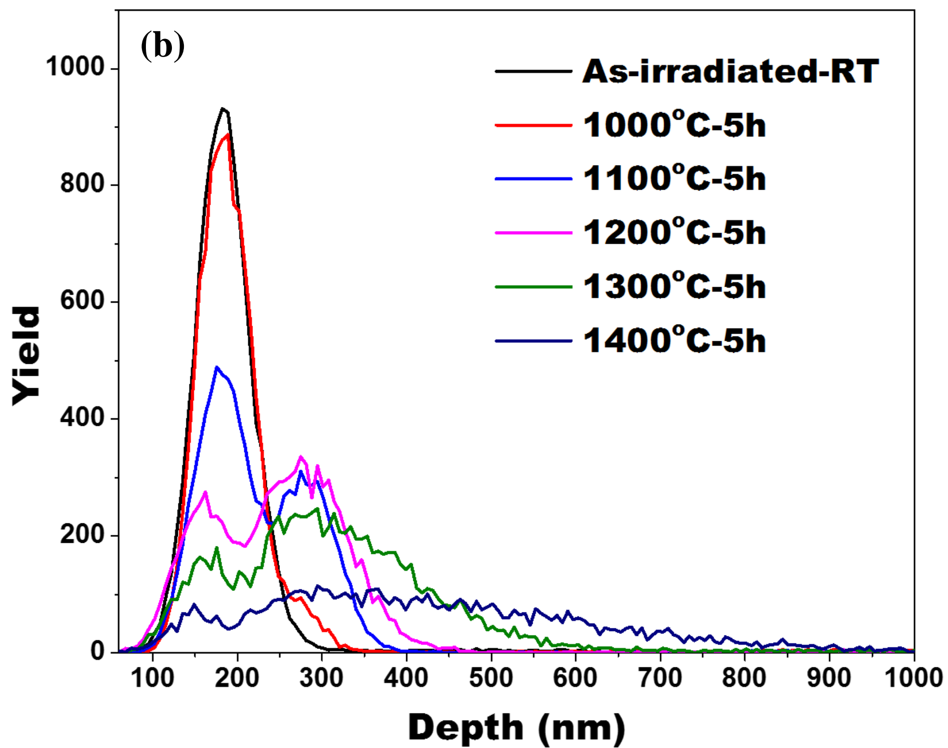

Fig. 7.30: Xe depth profiles showing the effect of high temperature annealing on the migration behaviour (a) as-implanted RT (b) after SHI irradiation.

Figure 31 shows the retained of Xe within the damaged region after SHI irradiation and high temperature annealing (1000 – 1400 °C). Annealing at 1000 °C show that the Xe retained with the damaged region is fairly with the same as the irradiated-RT. This means that the less amount of Xe ions moved toward the un-damage (see-Fig. 7.29 b). These results compared to that obtained from un-irradiated then concluded that the Xe ions before SHI irradiation migrate fast than after SHI irradiation. This may be due to the presence of a high number of pores in the undamaged region and became less or reduced after SHI irradiated.

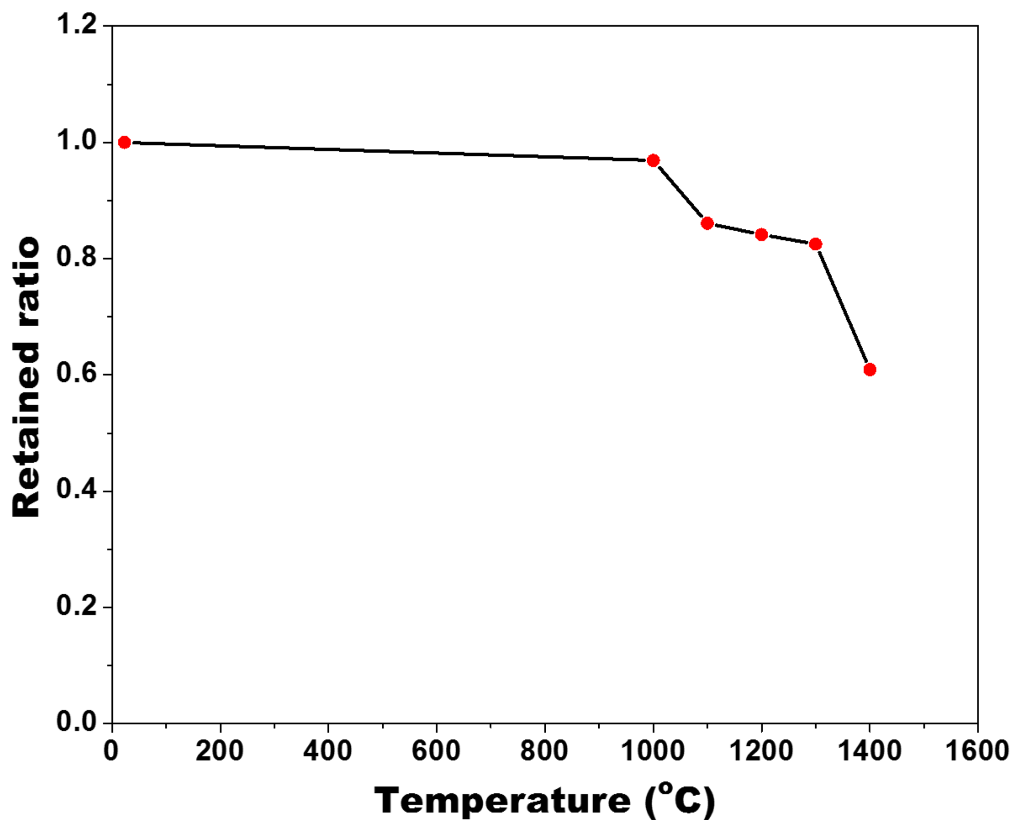

Fig. 7.31: The amount of Xe retained with the damaged region after SHI irradiation and annealed at temperature (1000 - 1400 °C).

7.3.3 Raman results

The Raman spectroscopy analysis of the sample irradiated with SHI to a fluence of 1×10^{14} ions/cm^2 was performed and the results are given in Figure 7.32. These results have been compared with the as-implanted and virgin glassy carbon. The D and G bands of GC reappeared and are pronounced and distinguishable as seen in Figure 7.32. The G peak intensity became

slightly more prominent compared to the D peak. This observation suggests that more crystallites were present in the previously damaged region near the surface of GC after SHI irradiation compared to as-implanted spectrum. This also can explain by the fact that the radiation-induced thermal transient can enhance the recovery along the ion track [Tou92]. These results well agree with the RBS results from SHI irradiation.

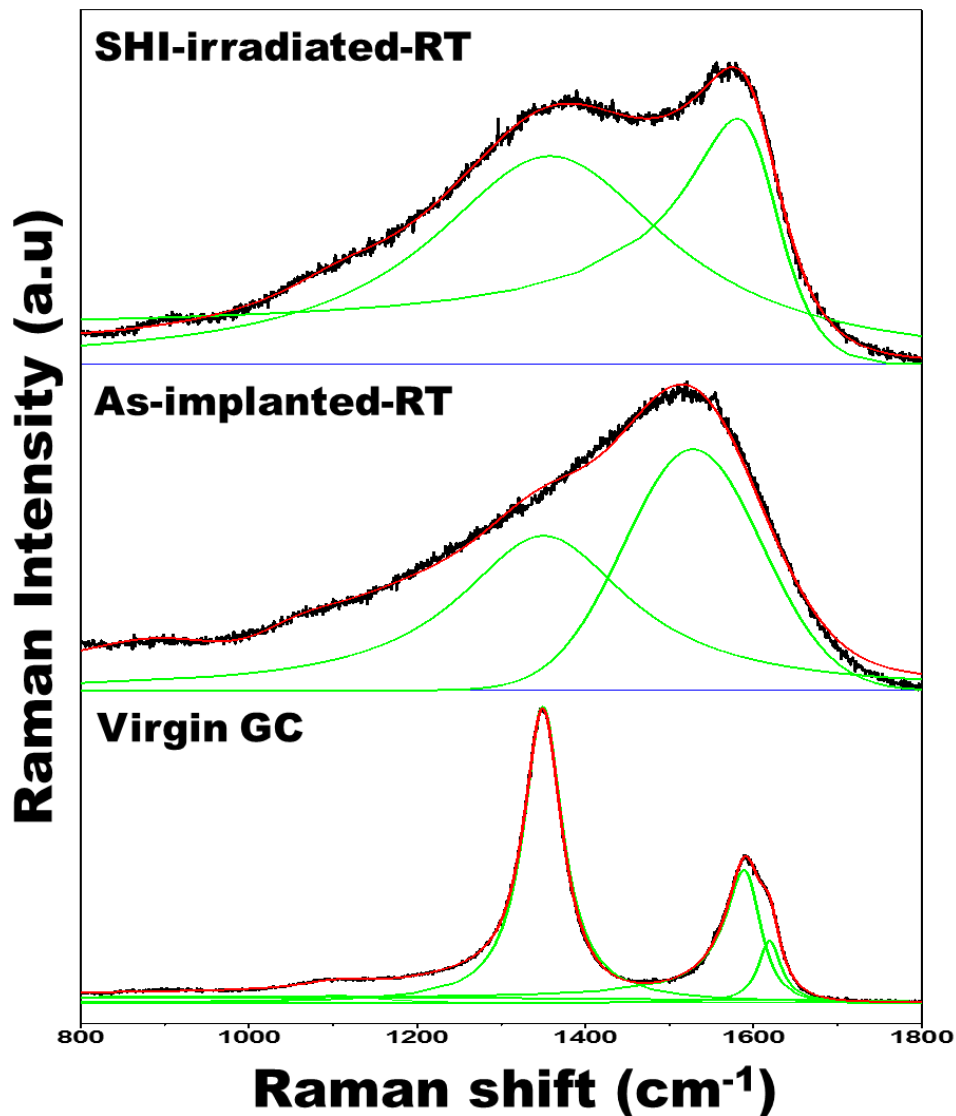

Fig. 7.32: Raman spectrum of Xe implanted in GC at RT and thereafter irradiated by 167 MeV Xe ion at RT to a fluence of 1×10^{14}. The red lines are the cumulative fit peak while the green lines represent the individual peak fit. The virgin GC Raman spectrum included for comparison.

The Raman spectrum of SHI irradiated and annealed were fitted using a Lorentzian fit for the D peak and a Breit-Wigner-Fano (BWF) fit for the G peak and the results are tabulated in table 7.3. The Lorentzian-BWF combination was used to fit as-irradiated spectrum, and the spectra of samples annealed at a temperature range of 1000 to 1500 °C (see-Fig 7.33). The I_D/I_G ratios, the G peak positions, the G peak FWHM, and the average crystallite sizes (La) for the un-irradiated and the implanted then irradiated are found to be as tabulated in table 7.3. The effect of annealing on the structure after SHI irradiation is shown in Figure 7.33. The samples were annealed at temperatures ranging 1000 °C to 1500 °C in steps of 100 °C for 5 hours. The G peak intensity after SHI irradiation was observed to slightly increase with the increase in annealing temperature. However, after annealed the results in table 7.2 (section 7.2.2 above) are very comparable to those obtained from un-irradiated samples (see table 7.3).

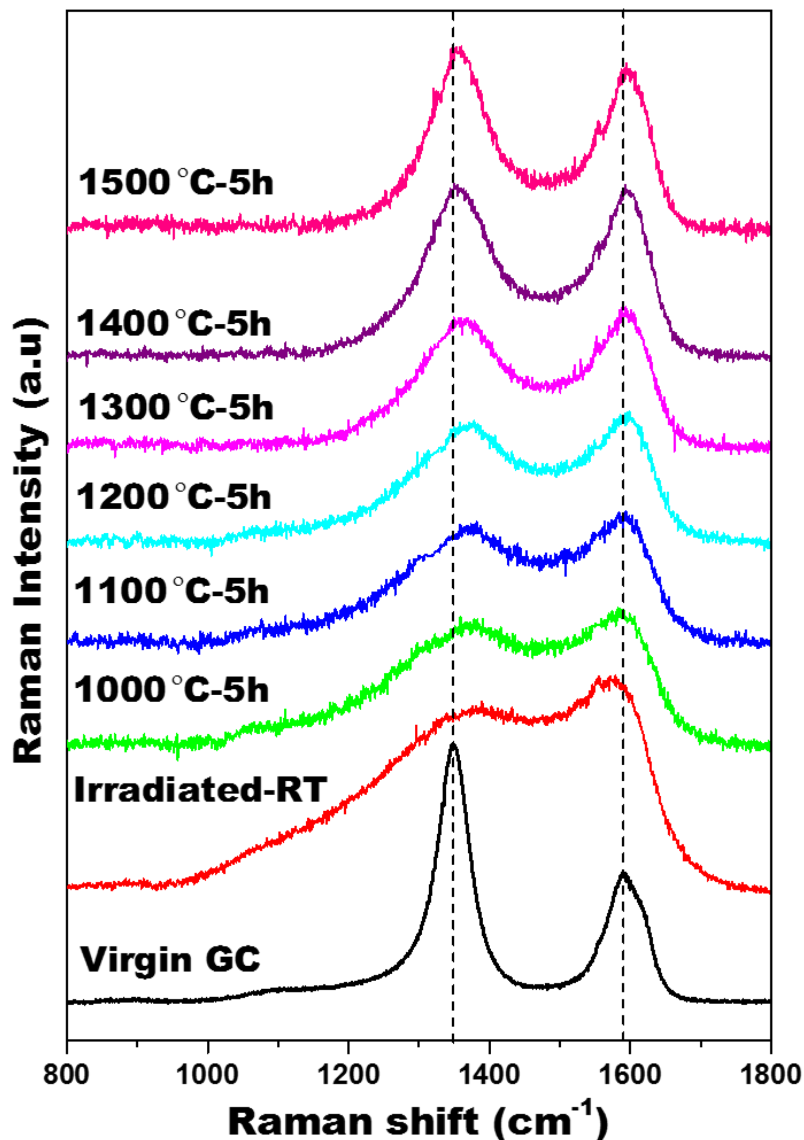

Fig. 7.33: Raman spectrum of xenon implanted GC at room then irradiated with SHI at room temperature and the effect of annealing at temperatures ranging from 1000 °C to 1500 °C in steps of 100 °C for 5 h, on the structure of GC. The Figure also contains the Raman spectrum for virgin GC for comparison.

Table 7. 3: The Raman results of the (200 keV Xe + SHI) irradiated GC at room temperature and annealed up to 1500 °C compared to the virgin glassy carbon at 0 °C. The quantitative acquired by fitting using a Lorentzian fit for the D peak and a Breit-Wigner-Fano (BWF) fit for the G peak.

Temp (°C)	I_D/I_G	G peak position (cm^{-1})	G peak FWHM	L_a (nm)
Pristine	1.52	1588	25.9	2.91
As-imp	0.35	1530	105	0.76
SHI	0.84	1580	66.7	1.23
1000	0.90	1587	61.2	1.27
1100	0.91	1591	55.8	1.28
1200	0.94	1594	51.7	1.31
1300	0.96	1595	47.1	1.32
1400	1.04	1597	42.4	1.37
1500	1.12	1597	42.3	1.43

From table 7.3, the crystallite size of the glassy carbon after SHI irradiation, obviously increased from 0.76 nm to 1.23 nm after SHI. This indicates that SHI irradiation resulted in the re-crystallization of the implanted region. Comparison between un-irradiated and after SHI irradiation results in Table 7.2 and Table 7.3, we can conclude:

i. Higher (La) size was observed in SHI irradiated samples over the whole temperature range of annealing.
ii. There was faster recovery after SHI irradiation.
iii. Due to recovery introduced in glassy carbon after SHI irradiation, the D and G peaks reappeared and are pronounced and distinguishable.

References

[Ava11] D.K. Avasthi, G.K. Mehta, Swift Heavy Ions for Materials Engineering and Nanostructuring, Springer Series in Materials Science 145, Netherlands, 2011.

[Ber98] S. D. Berger, D. R. McKenzie, P. J. Martin, EELS analysis of vacuum arc-deposited diamond-like films, *Philosophical Magazine Letters* **57** (1998) 285 – 290.

[Che83] A. A. Chernov, H. Miiller-Krumbhaar, Modern Theory of Crystal Growth I, Springer-Verlag, New York 1983.

[Dul84] W. W. Duley, Refractive indices for amorphous carbon, *The Astrophysical Journal* **287** (1984) 694 – 696.

[Fle75] R.L. Fleischer, B.P. Price, R.M. Walker, Nuclear Tracks in Solid: Principles and Applications, University of California Press, Berkeley, California, 1975.

[Fer00] A.C. Ferrari, J. Robertson, Interpretation of Raman spectra of disordered and amorphous carbon, *Physical Review B* **61** (2000) 14095 – 14107.

[Fer01] A.C. Ferrari, A model to interpret the Raman spectra of disordered, amorphous and nanostructured carbons, *Materials Research Society* **675** (2001) W11.5.1.

[Fer02] A.C. Ferrari, Determination of bonding in diamond-like carbon by Raman spectroscopy, *Diamond and Related Materials* **11** (2002) 1053 – 1061.

[Har04] P. J. F. Harris, Fullerene-related structure of commercial glassy carbons, *Philosophical Magazine* **84** (2004) 3159 – 3167.

[Har13] P. J. F Harris, Fullerene-like models for microporous carbon, *Journal of Materials Science* **48** (2013) 565 – 577.

[Ism18] M.Y.A. Ismail, J.B. Malherbe, O.S. Odutemowo, E.G. Njoroge, T.T. Hlatshwayo, M. Mlambo, E. Wendler, Investigating the effect of heat treatment on the diffusion behaviour of xenon implanted in glassy carbon, Vacuum, **149** (2018) 74 – 788.

[Iwa00] M. Iwaki and K. I. Terashima, Change in atomic density of glassy carbon by Na ion implantation, *Surface and Coatings Technology* **128-129** (2000) 429 – 433.

[Jur18] K. Jurkiewicz, M. Pawlyta, D. Zygadło, D. Chrobak, S. Duber, R. Wrzalik, A. Ratuszna, and A. Burian, Evolution of glassy carbon under heat treatment: correlation structure-mechanical properties, *Journal of Materials Science* **53** (2018) 3509 – 3523.

[Kip64] J. J. Kipling, J. N. Sherwood, P. V. Shooter, N. R. Thompson, The pore structure and surface area of high-temperature polymer carbons, Carbon **1** (1964) 321-328.

[Koz14] T. Kozu, M. Yamaguchi, M. Kawaguchi, H. Shima, J.W. Kim, M. Matsuoka, K. Nishida, T. Yamamoto, Evaluating of Diamond Like Carbon Using Deep UV Raman Spectroscopy, *Integrated Ferroelectrics* **157** (2014) 147 – 156.

[Lav08] V. Lavrentiev, J. Vacik, H. Naramoto, Structural phenomena in glassy carbon induced by cobalt ion implantation, *Applied Physics A* **92** (2008) 673-680.

[Mar90] D. Marton and J. Fine, Sputtering-induced surface roughness of metallic Thin films, Thin Solid Films, **185** (1990) 79 – 90.

[Mal17] J.B. Malherbe, P.A. Selyshchev, O.S. Odutemowo, C.C. Theron, E.G. Njoroge, D.F. Langa, T.T. Hlatshwayo, Diffusion of a mono-energetic implanted species with a Gaussian profile, *Nuclear Instruments and Methods in Physics Research B* 406 (2017) 708 – 713.

[McC94] D.G. McCulloch, S. Prawer, A. Hoffman, Structural investigation of xenon-ion-beam-irradiated glassy carbon, *Physical Review B* **50** (1994) 5905 – 5917.

[Nem79] R.J. Nemanich, S.A. Solin, First- and second-order Raman scattering from finite-size crystals of graphite, *Physical Review B* **20** (1979) 392 – 401.

[Ni08] Z. Ni, Y. Wang, T. Yu, Z. Shen, Raman spectroscopy and imaging of graphene, Nano Res. **1** (2008) 273-291.

[Njo17] E.G. Njoroge, L.D. Sebitla, C.C. Theron, M. Mlambo, T.T. Hlatshwayo, O.S. Odutemowo, V.A. Skuratov, E. Wendler, J.B. Malherbe, Structural modification of indium implanted glassy carbon by thermal annealing and SHI irradiation, Vacuum, **144** (2017) 63 – 71.

[Njo14] E. G. Njoroge, Solid-state interactions between Zr thin films and SiC, PhD Thesis, University of Pretoria, 2014

[Odu16] O.S. Odutemowo, J.B. Malherbe, L. Prinsloo, D.F. Langa, E. Wendler, High temperature annealing studies of strontium ion implanted glassy carbon, *Nuclear Instruments and Methods in Physics Research B* **371** (2016) 332 – 335.

[Odu18] O.S. Odutemowo, J.B. Malherbe, L.C. Prinsloo, E.G. Njoroge, R. Erasmus, E. Wendler, A. Undisz, M. Rettenmayr, Structural and surface changes in glassy carbon due to strontium implantation and heat treatment, *Journal of Nuclear Materials* **498** (2018) 103 – 116.

[Pra90] S. Prawer, F. Ninio, I. Blanchonette, Raman spectroscopic investigation of

ion-beam-irradiated glassy carbon, *Journal of Applied Physics* **68** (1990) 2361 – 2366.

[Rus87] E. Ruska, The Development of the Electron Microscope and of Electron Microscopy, Bioscience Reports, Vol. 7, No. 8, Germany, 1987.

[Sai02] H. Saitoh, T. Shinada, Y. Ohkawara, T. Shinada, Surface modification of glassy carbon by pulsed laser irradiation with several wavelengths, *Journal of Applied Physics* **41** (2002) 5359 – 5366.

[Sie82] R. W. Siegel, Atomic Defects and Diffusion in Metals, Amsterdam 1982.

[Sil03] S.R.P. Silva, Properties of Amorphous Carbon, INSPEC, London, UK, 2003.

[Sri12] J. Ziegler, SRIM 2012 computer code, (2012). www.srim.org.

[Toi01] Hiroshi Toida, Keiichi Terashima, Tomohiro Kobayashi, Minoru Osada, Kowashi Watanabe, Masaya Iwaki, Densification of glassy carbon by fluorine ion implantation, *Nuclear Instruments and Methods in Physics Research B* **175-177** (2001) 532 – 536.

[Tui70] F. Tuinstra, J.L. Koenig, Raman spectrum of graphite, *Journal of Chemical Physics* **53** (1970) 1126.

[Tou92] M. Toulemonde, C. Dufour, E. Paumier, Transient thermal process after a high energy heavy-ion irradiation of amorphous metals and semiconductors, Phy. Rev. **B 46** (1992) 14 362 – 14369.

[Wan94] Z. G. Wang, Ch Dufour, E. Paumier, M. Toulemoude, The Se sensitivity of metals under swift-heavy-ion irradiation: a transient thermal process, *Journal of Physics: Condensed Matter* **6** (1994) 6733 – 6750.

[Wen12] E. Wendler, Th. Bierschenk, F. Felgenträger, J. Sommerfeld, W. Wesch, D. Alber, G. Bukalis, L.C. Prinsloo, N. van der Berg, E. Friedland, J.B. Malherbe, Damage formation and optical absorption in neutron irradiated SiC, *Nuclear Instruments and Methods in Physics Research B* **286** (2012) 97 – 101.

[Yos88] M. Yoshikawa, G. Katagiri, H. Ishida, A. Ishitani, T. Akamatsu, Raman spectra of diamond-like amorphous carbon films, *Journal of Applied Physics* **64** (1988) 6464 – 6468.

[Zha15] Y. Zhang, R. Sachan, O. H. Pakarinen, M. F. Chisholm, P. Liu, H. Xue, W. J. Weber, Ionization-induced annealing of pre-existing defects in silicon carbide, Nature *Communications* **9049** (2015) 1 – 7

CHAPTER 8

CONCLUSION

This study investigates the migration behaviour of xenon (Xe) ions-implanted into glassy carbon. This was with a view to check whether glassy carbon will be a good diffusion barrier for Xe as a fission product. The experimental techniques used in this study gave quantitative and qualitative information on the migration behaviour; the surface morphology and the structural changes after Xe implanted into glassy carbon; subsequently irradiated with swift heavy ion (SHI). This information obtained is required to understudy the behaviour of glassy carbon if it was going to be used as a storage device to contain Xe fission products. The conclusions and summary from these work are presented in the sections below.

8.1 Xenon implantation in glassy carbon samples

200 keV of Xe ions were implanted in glassy carbon at room temperature (RT) to a fluence of 1×10^{16} ions/cm^2. The samples was then characterized with RBS, Raman, SEM, AFM and HR-TEM techniques.

We have reported the conventional RBS depth profile results after annealing at two different temperature regimes, 300 – 800 ^{o}C and 900 – 1500 ^{o}C, respectively. For the first annealing temperature regime, 300 – 800 ^{o}C, no noticeable diffusion of Xe was observed as the profile remained nearly the same as compared to the as-implanted depth profile. The non-diffusion of Xe at these low temperatures could be as a result amorphisation of the glassy carbon leading to creation of point defects in the implanted region of the glassy carbon substrate. The defects which could be in terms of voids and vacancies are responsible for the trapping of Xe well within the damaged region of the glassy carbon matrix. Annealing was carried out in the 2nd temperature regime, (900 ^{o}C$\leq$ T $\leq$ 1500 ^{o}C). The Xe profile shifted towards the surface of glassy carbon after annealing at 900 ^{o}C. The shift at this temperature towards the surface was accompanied with slight broadening of the Xe profile. This broadening was considered critical because the diffusion of Xe was Fickian (Gaussian) in nature. Annealing from 1000 – 1500 ^{o}C resulted in the movement of Xe profile deeper beyond the damaged bulk deeper into the undamaged bulk of glassy carbon and the formation of a bimodal distribution was also observed. As the Xe atom moved deeper into the undamaged bulk, the migration behaviour

extends up to a depth of 800 nm deeper into the undamaged bulk with increasing bimodal distribution formation after annealing at 1400 °C. The migration of Xe deeper into the undamaged bulk of glassy carbon was not expected because the TRIM simulation shows that the damage introduced in glassy carbon after Xe implantation is concentrated near the surface. The migration behaviour of Xe was different from every other fission products earlier studied in glassy carbon. The model given for this unpredictable migration behaviour of Xe is the presence of large number of pores in glassy carbon. These pores needs to be filled up when Xe atoms become more energized after annealing at higher temperatures.

The effect of xenon ion implantation in glassy carbon has been investigated using Raman spectroscopy. Each time Raman spectroscopy was carried out, the baseline of the spectrum lines were corrected using a linear background correction. The corrected spectrum was then fitted using a Lorentzian fit for the D peak and a Breit-Wigner-Fano (BWF) fit for the G peak. The virgin glassy carbon spectra obtained at 514.5 nm shows that D and G peaks are at 1350 cm^{-1} and 1587 cm^{-1}, respectively. The D peak position representative of a disordered graphite structure and the G peak position is typical of a graphite single crystal. Xenon implantation into glassy carbon resulted in amorphisation as evident by the merging of D and G peaks, decreased I_D/I_G ratio and increased FWHM.

Annealing of the sample in the first temperature regime shows that the damaged layer caused by Xe implantation start to recrystallizes after annealing at 500 °C. This temperature is considered a dynamic annealing temperature for Xe implanted glassy carbon. Some observed changes after annealing at 500 – 900 °C include a decrease and narrowing of the FWHM of the G peak, a decrease in the I_D/I_G ratio and upshift in the G peak positions. However, annealing of the xenon implanted glassy carbon sample up to 900 °C did not revert to its original state before irradiation.
The re-growth of the Raman D and G peaks was further observed after high temperature annealing of the implanted glassy carbon from 1000 °C to 1500 °C. From 1000 – 1300 °C, the D and G peaks shows better recovery with slightly increased G peak than the D peak. However, at 1400 °C and 1500 °C, the intensity of the D and G peak appear to be the same. At the highest annealing temperature, (1500 °C), the crystallite size, La of the implanted glassy carbon have increased from 0.88 to 1.39. This is an indication that the structural recovery of the implanted layer resulted in a structure that is more graphite-like than the glassy carbon. The difference in

the crystallite sizes also means that some of the damage introduced by Xe ion implantation was still retained after heat treatment at highest temperature.

The effect of xenon ions bombardment and heat treatment on the surface topography of the GC was characterized using scanning electron microscopy (SEM) complemented by atomic force microscopy (AFM). AFM was used to evaluate and quantify the effect of Xe ion bombardment and annealing temperature on the surface roughness. The R_q and R_a values obtained are 1.71 nm and 1.36 nm respectively, for virgin glassy carbon. These values increased to 2.54 nm and 1.97 nm respectively after Xe ion bombardment. This indicates that the sample surface became rougher and this is due to the surface roughening effect of ion-induced sputtering. The increase in the surface roughness after Xe bombardment was in agreement with the SEM images. The SEM micrographs obtained the samples showed that the polishing marks became prominent after ion bombardment. The R_q value significantly increased to 4.12 nm after annealing at 1500 ^{o}C. This value of R_q is typical for a much roughened surface. This result was confirmed by SEM for the sample annealed at 1500 ^{o}C. The SEM micrograph shows a uniform distribution of large granules on the surface of the sample.

The HRTEM analyses gave a clearer information on the structure of virgin glassy carbon and after ion bombardment. The TEM images of the virgin glassy carbon indicated a layered fullerene-like nano structure. This structure changed after Xe bombardment indicating the amorphization of glassy carbon with the presence of some nano-crystallites features. The HRTEM image of sample annealed at 600 ^{o}C had showed some graphitic strands which became reduced after annealing at 1500 ^{o}C. The HRTEM result of annealed sample might depicts some form of recrystallization or recovery of the glassy carbon.

Another effect of the implanted Xe in glassy carbon is densification. The densification of glassy carbon due to Xe implantation was investigated by calculating the step heights between the implanted and un-implanted regions using AFM. The height of the implanted region was lower as compared to the un-implanted region. The relative height difference was used to calculate the density as 2.215 gcm^{-3}. This value is much comparable to the density of graphite which is 2.26 gcm^{-3}. This shows that the recovery of the implanted region resulted in a structure that is more graphite-like than glassy carbon.

8.2 Swift heavy ion (SHI) irradiation of Xe ion-implanted glassy carbon

An important parameter considered in this study is the effect of effect of swift heavy ion irradiation on Xe ion-implanted glassy carbon. We have hypothesized that glassy carbon will be exposed to radioactivity release (in orders of 100s MeV to few GeV) resulting from the fission process of nuclear waste with large range of energies. Glassy carbon proposed as a nuclear waste containment material in this study is expected to undergo structural changes after SHI irradiation. The SRIM simulation confirmed that the energy loss due to 167 MeV Xe ion in glassy carbon was found to be via electronic excitation from inelastic collisions and not nuclear elastic collisions.

The RBS result of sample irradiated with 167 MeV Xe SHIs at fluence of 1×10^{14} ions/cm^2 indicates an increased shift of Xe ions towards the undamaged bulk of glassy carbon as compared to the un-irradiated but as-implanted sample. This shift of Xe may be due to the transient melting along the ion trajectory which also resulted in a little amount of xenon that have evaporated.

The Xe SHIs irradiated but implanted sample was annealed in the temperature range of 1000 – 1500 ^{o}C in steps of 100 for 5 hours and characterize with RBS. The RBS depth profile of SHI irradiated but implanted sample indicate the diffusion of Xe after annealing at 1000 ^{o}C. The RBS depth profiles obtained for the sample irradiated with SHIs and subsequently annealed was not expected. The un-irradiated sample had a bimodal distribution after annealing at 1000 ^{o}C. The RBS depth profiles obtained for the sample irradiated with SHIs and subsequently annealed between 1100 and 1500 ^{o}C showed a similar migration behaviour for Xe as compared with the un-irradiated but as-implanted sample. This implies that SHIs irradiation does not influence the migration behaviour of Xe in glassy carbon at annealing temperature $\geq$ 1100 ^{o}C.

The effect of SHIs on the damaged layer of the implanted glassy carbon was investigated by using Raman spectroscopy. Two distinguished peaks reappeared near the D and G bands of the glassy carbon as a result of SHIs irradiation. The G peak intensity became slightly more prominent as compared to the D peak intensity. This observation means that glassy carbon structure is already recrystallizing as a result of SHIs irradiation which was later confirmed by the calculated increased crystallite size. These results agree well with the RBS results for SHI irradiation.

8.3 Future work

Previous studies of ion implanted in glassy carbon was carried out to understudy the diffusion or migration behaviour of fission products in glassy carbon. The results of these studies have shown that diffusion and/or migration of these nuclides are always directed towards the surface. Also, SRIM simulation correctly predicts the migration of the previous studies. This is not the case with our results in this study. Damage created into glassy carbon after Xe ion implantation into glassy carbon was very close to the surface than the bulk. Likewise, the migration of Xe was into the undamaged bulk of the glassy carbon matrix after annealing at high temperature (1000 – 1500 ^{o}C). According to our study, a different model was proposed to explain the migration behaviour of gaseous Xe. This model might also be useful to study other gaseous fission products like Ar and Kr implanted into glassy carbon. The migration behaviour of other heavy gaseous ions is therefore proposed for further studies may be our proposed model might be established for gaseous fission products.

Another suggestive study is to critically examine the structure of glassy carbon with respect to determining how glassy carbon behave to stress and strain after Xe implantation and annealing at higher temperatures. Several models have been developed to describe the structure of glassy carbon, however, these models have been unable to explain some of the properties of glassy carbon. In future, we will attempt to develop a model that explains the structure of glassy carbon. This will be done by using several analytical techniques such as Raman spectroscopy, transmission electron microscopy (TEM) and X-ray diffraction (XRD). And also, further studies should be carried out to characterize the type of diffusion or migration mechanisms peculiar to metallic, non-metallic and gaseous fission products, respectively.

CHAPTER 9

RESEARCH OUTPUT

The work in this thesis has contributed to several publications and conference proceedings. A summary of these research outputs is listed below:

9.1 Publications in peer-reviewed or refereed journals

1. **M.Y.A. Ismail**, J.B. Malherbe, O.S. Odutemowo, E.G. Njoroge, T.T. Hlatshwayo, M. Mlambo, E. Wendler, Investigating the effect of heat treatment on the diffusion behaviour of xenon implanted in glassy carbon, *Vacuum* **149** (2018) 74 –78.

2. O.S. Odutemowo, M.S. Dhlamini, E. Wendler, D.F. Langa, **M.Y.A. Ismail**, J.B. Malherbe, Effect of heat treatment on the migration behaviour of Sr and Ag CO-implanted in glassy carbon *Vacuum* **171** (2020) 109027.

3. M.J. Madito, **M.Y.A. Ismail**, T.T. Hlatshwayob, C.B. Mtshali, The nature of surface defects in Xe ion implanted glassy carbon annealed at high temperatures: Raman spectroscopy analysis, *Applied Surface Science* **506** (2020) 145001.

4. A.J. Innocent, T.T. Hlatshwayo, E.G. Njoroge, T.P. Ntsoane, M. Madhuku, E.O. Ejeh, M. Mlambo, **M.Y.A. Ismail**, C.C. Theron, J.B. Malherbe, Evaluation of diffusion parameters and phase formation between tungsten films and glassy carbon, *Vacuum* **175** (2020) 109245.

5. Z.A.Y. Abdalla, **M.Y.A. Ismail**, E.G. Njoroge, T.T. Hlatshwayo, E. Wendler, J.B. Malherbe, Migration behaviour of selenium implanted into polycrystalline 3C-SiC, *Vacuum* **175** (2020) 109235.

9.2 Conference Presentations

9.2.1 National Conferences

The 6^{2nd} Annual Conference of the South African Institute of Physics (SAIP 2017). Department of Physics, University of Stellenbosch, July 2017, Stellenbosch, South Africa.
(Poster presentation)

9.2.2 International Conferences

I. The 23rd International Conference on Ion-Surface Interaction (ISI-2017), August 2017, Moscow, Russia. (Poster presentation)

II. 2nd International Conference on Material Science and Nanotechnology (IMSNC-2019), July 2019, London, UK. (Poster presentation)

III. 24th International Conference on Ion Beam Analysis (IBA-2019), October 2019, Antibes, France. (Poster presentation)